NGU REPORT
2022.010

Trenching and 14C dating
of the Stuoragurra fault complex
in Finnmark, Northern Norway
– with some accompanying
data included : revised edition

GEOLOGY FOR SOCIETY

SINCE 1858

GEOLOGICAL
SURVEY OF
NORWAY
- NGU -

NGU REPORT
2022.010

Trenching and ^{14}C dating
of the Stuoragurra fault complex
in Finnmark, Northern Norway
– with some accompanying
data included : revised edition

Trenching transverse to the fault scarp at Latnetoaivi, Stuoragurra, Finnmark, Northern Norway. Exposed hanging wall (upper left), and brownish fault breccia overlying bluish-grey deformed till (central part). Vertical section c. 4 m high, fault scarp 7 m high.

Erratum to NGU Report 2022.010

Revision of NGU Report 2022.010 pr. 22.09.2022

Based on new field observations during the autumn this year we find it necessary to adjust parts of the mentioned report, and changes have been done in Figs. 2 and 3 (minor changes), and 9, including figure caption to Fig. 9. Also changes in the figure caption to Fig. 26 have been done .

At page 48 the following changes have been done:

Upper part –
Old version: … However, the age is not quite recent because the rock fall material seems to have had enough time to transform to a rock-glacier type of formation, at least in the lower parts….
New version: … Curvilinear structures in the lower parts may indicate that this portion of the rock fall material may have had enough time to transform to a rock-glacier type of formation. However, field observations this year indicate that the curvilinear structures may alternatively be a result of sliding of the avalanche on thick sandy glaciogenic deposits in the steep valley side….

Lower part –
Old version: … If the unstable area also reaches, e.g., 100 m into the bedrock, then it will include an unstable bedrock volume of c. 20 mill. m3. The reservoir immediately below the unstable rock slope has a length of c. 700 m, a depth of c. 45 m and a width of c. 110 m. In total, this volume represents c. 1.75 million m3 of water that most likely will be displaced if up to 20 million m3 of rock falls into the reservoir…
New version: … If the unstable area also reaches, e.g., 100 m into the bedrock, then it will include an unstable bedrock volume of c. 3 mill. m3. The reservoir immediately below the unstable rock slope has a length of c. 700 m, a depth of c. 45 m and a width of c. 110 m. In total, this volume represents c. 1.75 million m3 of water that most likely will be displaced if up to 3 million m3 of rock falls into the reservoir…

The revised NGU Report 2022.010 of 22.09.2022 replace the previous report from 15.05.2022.

23.09.22

Lars Olsen   Odleiv Olesen

NORGES GEOLOGISKE UNDERSØKELSE
- NGU -

REPORT

Geological Survey of Norway
P.O.Box 6315 Torgarden
NO-7491 TRONDHEIM
Tel.: 47 73 90 40 00

Report no.: 2022.010	ISSN: 0800-3416 (print) ISSN: 2387-3515 (online)	Grading: Open

Title:
Trenching and 14C dating of the Stuoragurra Fault Complex in Finnmark, Northern Norway – with some accompanying data included : revised edition

Authors: Olsen, L., Olesen, O., Høgaas, F., Poliakova, A., Rueslåtten, H., Schönenberger, J., van der Lelij, R., Tassis, G. and Bjørlykke, A.	**Client:** NGU; projects 378100 and 362200.
County: Finnmark (Troms & Finnmark)	**Commune:**
Map-sheet name (M=1:250.000)	**Map-sheet no. and -name (M=1:50.000)**
Deposit name and grid-reference:	**Number of pages:** 71 **Price (NOK):** 210

Fieldwork carried out: 2018-2022	**Date of report:** **Revised report 22.09.2022**	**Project no.:** 362200	**Person responsible:** Marco Brönner

Summary:

The Stuoragurra Fault Complex (SFC) constitutes the Norwegian part of the larger Lapland province of postglacial faults in northern Fennoscandia. The 90 km long SFC consists of three separate fault systems; the Fitnajohka Fault System in the southwest, the Máze Fault System in the central area and the Iešjávri Fault System to the northeast. The distance between the fault systems is 7–12 km. The faults dip at an angle of 30–75° to the SE and can be traced on reflection seismic data to a depth of c. 500 m. Here we present data from trenching of different sections of the fault complex. The trenching reveals deformed overburden in all 8 sites, and inclusions of peat and organic bearing soil in the deformed and partly overrun loose deposits on the footwall in all but one site.

Radiocarbon dating of organic matter located in buried and severely deformed sediment horizons indicates late Holocene ages for the (final) formation of the different fault segments, more specifically that the Máze, Fitnajohka and Iešjávri (Guovziljohka) Faults formed during earthquakes younger than 600 years, younger than 1,300 years and younger than 4,000 years BP, respectively. The youngest age is at the Masi (Mazé) site, where plant macrofossil data from the buried sediments suggest an early to late Holocene vegetation cover. The reverse displacement of c. 9 m and fault system lengths of 14 and 21 km of the two southernmost fault systems indicate a moment magnitude of c. 7 on Richter's scale if just one rupture event is associated with each of these systems. The fault rupture with length and height of fault scarps, and injections and throw-out of angular boulders and wedges of fault breccia reaching up to 15–20 m away from the fault scarp give the most distinct expressions of the associated earthquake magnitude with the SFC. A total of c. 60 landslides, some of these possibly earthquake-induced, has been recorded along the SF. Initial breakage or fracturing of bedrock with a potential to lead to larger rock avalanches are also recorded at a few places in or close to the fault zone.

Keywords: Postglacial fault	Reverse fault	Neotectonics
14C and K-Ar dating	Sediment deformation	Macro plant remains
Georadar data	Landslide	Rock avalanche

Content

29 figures

7 tables

Corresponding authors: Lars Olsen (Lars.Olsen@ngu.no) vs. trenching and ^{14}C dating; Odleiv Olesen (Odleiv.Olesen@ngu.no) vs. geophysics and general issues

Introduction

Two postglacial faults have previously been reported from Norway: The Nordmannvikdalen Fault in northern Troms (Bakken, 1983; Tolgensbakk & Sollid, 1988; Dehls et al., 2000; Olsen et al., 2018) and the Stuoragurra Fault Complex (SFC) in western Finnmark (Olesen, 1988; Olesen et al., 1992a, b, 2004, 2013, 2022; Bungum & Lindholm, 1997; Roberts et al., 1997; Dehls et al., 2000). The faults have been assumed to be of Younger Dryas and postglacial age, respectively, and constitute the northern part of the Lapland postglacial fault province in northern Fennoscandia (Lagerbäck & Sundh, 2008; Olesen et al., 2013; Smith et al., 2014; Sutinen et al., 2014; Mikko et al., 2015; Palmu et al., 2015). The postglacial faults are assumed to have formed because of released excess horizontal stresses generated during glaciation and activated by deglaciation and glacial isostatic rebound (Wu et al., 1999; Lund et al., 2009; Steffen et al., 2014a, b). Lagerbäck & Sundh (2008) argue further that the outburst of lateglacial faulting in northern Sweden was restricted to the last deglaciation. They argued that the modest glacial erosion in this part of Sweden would allow older fault scarps of similar magnitude to be preserved. The postglacial faults in northern Fennoscandia (Fig. 1) have been considered to represent single rupture events at the end of, or after, the last Weichselian glaciation. Lagerbäck & Sundh (2008), Smith et al. (2018) and Mattila et al. (2019) have, however, provided field evidence for multiple slip events, some of these probably older than postglacial time, and some represent postglacial faulting.

A review of the present-day knowledge of the structure and deformation along the postglacial SFC was given by Olesen et al. (2022), and their main conclusions are included as background information in the next section: Geological and geophysical setting.

Olesen et al. (2022) adapted the term 'complex' for the Stuoragurra Fault since it consists of three or more fault systems which again consists of at least 29 segments (Fig. 2). We now think that the fault systems formed at different times (Olsen et al., 2020; Olsen et al., 2021). The terms 'fault complex' and 'fault system' have been introduced for other postglacial faults in northern Fennoscandia (e.g., by Ojala et al., 2017) and Olesen et al. (2022) have accordingly grouped the SFC segments into the Fitnajohka, Máze and Iešjávri Fault Systems.

Lithified fault breccia has been recorded in bedrock in the fault zone at Fitnajohka (Olesen et al., 1992a, Roberts et al., 1997), and in all trenches reaching bedrock. This indicates old fault activity with formation of fault breccia, followed by a period with diagenesis. The original fault activity

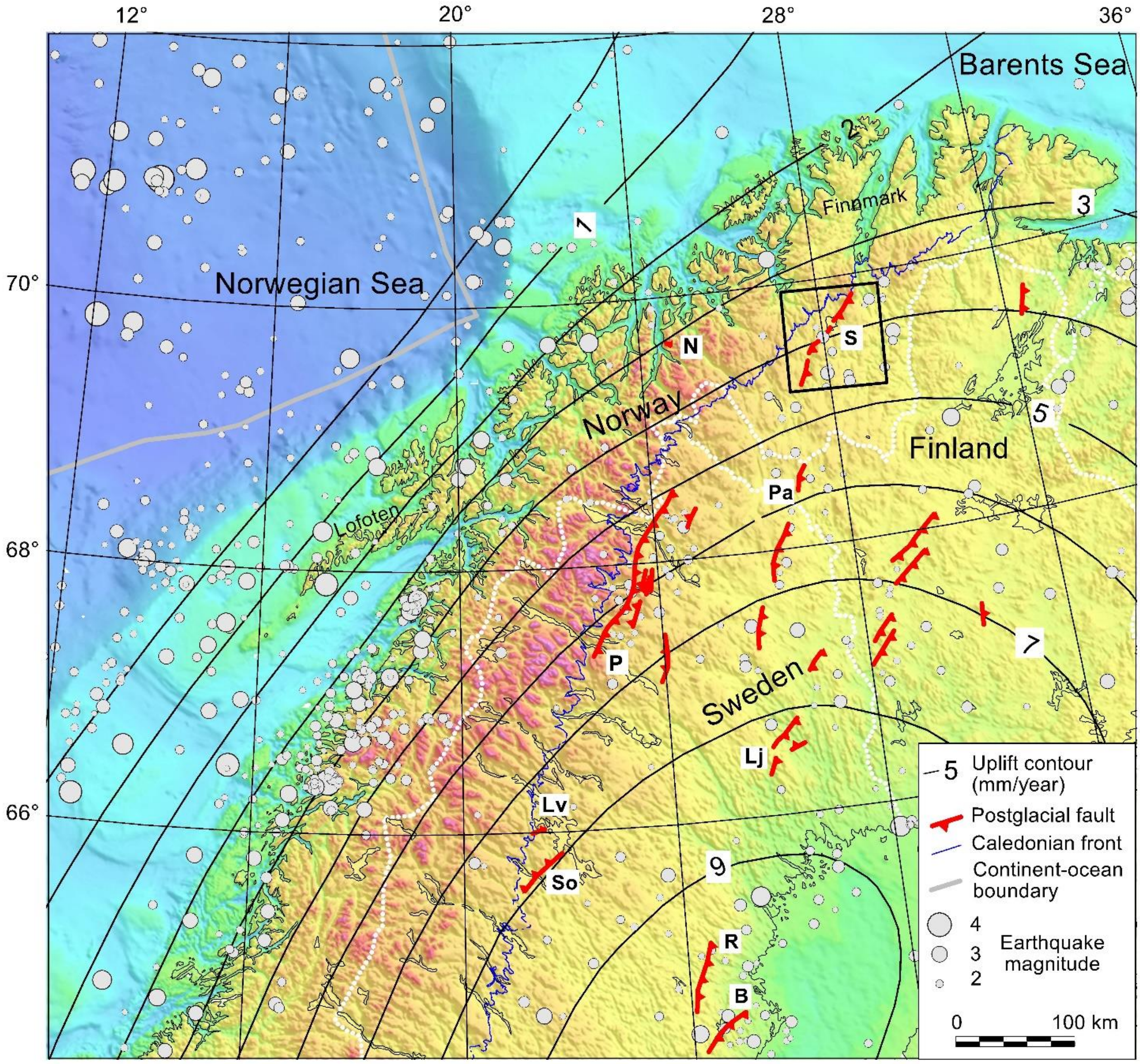

Figure 1. Postglacial faults, topography, bathymetry, earthquakes during the period 1750–2011 and present-day uplift (mm/year) in northern and central Fennoscandia (modified from Olesen et al., 2022). The Norwegian National Seismological Network at the University of Bergen is the source of the earthquake data in Norway, Svalbard and NE Atlantic. Data on the other earthquakes in Finland and Sweden are downloaded, from the web pages of the Institute of Seismology at the University of Helsinki; http://www.seismo.helsinki.fi/english/bulletins/index.html. The topography and bathymetry are compiled from various sources by Olesen et al. (2010). Most of the faults within the Lapland province of postglacial faults cuts the present-day uplift contours at an angle of 30-70°. The postglacial faults occur in areas with increased seismicity indicating that they are active at depth. The Stuoragurra, Pärvie, Laisvall and Sorsele Faults are located immediately to the east of the Caledonian front. The black frame shows the location of Figs. 2 and 3 and the Stuoragurra Fault Complex. N- Nordmannvikdalen Fault; S-Stuoragurra Fault Complex; B-Burträsk Fault; Lv-Laisvall Fault; Lj-Lansjärv Fault; P-Pärvie; Pa-Palojärvi; Fault; R-Röjnoret Fault; So-Sorsele Fault.

in this zone may therefore be of Cambrian to Ordovician age, or probably much older based on structural studies (Roberts et al., 1997; Henderson et al., 2015).In addition, weathering of fault gouge at Fitnajohka, with production of, e.g., kaolinite and vermiculite (Åm, 1994) a long time before the youngest fault activity in the SFC zone, indicates together with the lithified breccia that the SFC is merely a postglacial reactivation of an old fault zone.

The historical record of seismicity in northern Norway is short since the first report in the Scandinavian Earthquake Archive within the area is describing an earthquake in Karasjok and adjacent areas in Finland on the 31st of December 1758. The recurrence interval of large earthquakes in intraplate regions like northern Norway can be several hundred years or even longer. It is therefore necessary to undertake palaeoseismological studies to fill in some of the missing time before 1758. Rock avalanches and landslides, potentially triggered by earthquakes, can generate tsunamis in fjords and lakes and constitute the greatest seismic hazard to society in Norway (Bungum & Olesen, 2005). Such information is therefore of high societal importance for the hazard assessments and mitigating the effects of future large earthquakes on petroleum installations, carbon capture storage (CCS) and hydropower dams in a formerly glaciated region such as Fennoscandia.

The present report presents a compilation of the results from analyses of aerial photographs, LIDAR data, and trenching across the Stuoragurra Fault scarps at locations along all three fault systems, including radiocarbon dating and macrofossil content of buried organic material, geophysical profiling, and K-Ar dating and XRD and XRF analysis of a sample of fault gouge from Ellajávri, south-southwest of Masi. The ^{14}C dating results indicate possibly different ages of the fault events in the three separate faults systems.

The work has been carried out within the frame of the two NGU projects ‘378100 Bokutgivelse - Glacially Triggered Faulting - Cambridge University Press’ and ‘362200 - Crustal onshore-offshore project - Phase 3 (Coop3)’.

Geological and geophysical setting

The 90-km-long SFC dips at an angle of 30–75° to the SE and can be traced on reflection seismic data to a depth of c. 500 m (Olesen et al., 2022), and may well extend downward. The fault segments of the SFC can be grouped into three major systems separated by c. 6–7 to 12 km long gaps without any apparent faulting (Fig. 2). Therefore, the fault segments were most likely formed during three or more separate earthquakes. Because of the large rupture lengths (≥14 km), the fault systems extend most likely to a depth of several kilometres (Olesen et al., 2022). The SFC (Fig. 2) is located within the regional c. 4–5 km wide Mierojávri-Sværholt Shear Zone (MSSZ) in the Precambrian of Finnmark, northern Norway (Olesen et al., 1992a; Olesen & Sandstad, 1993;

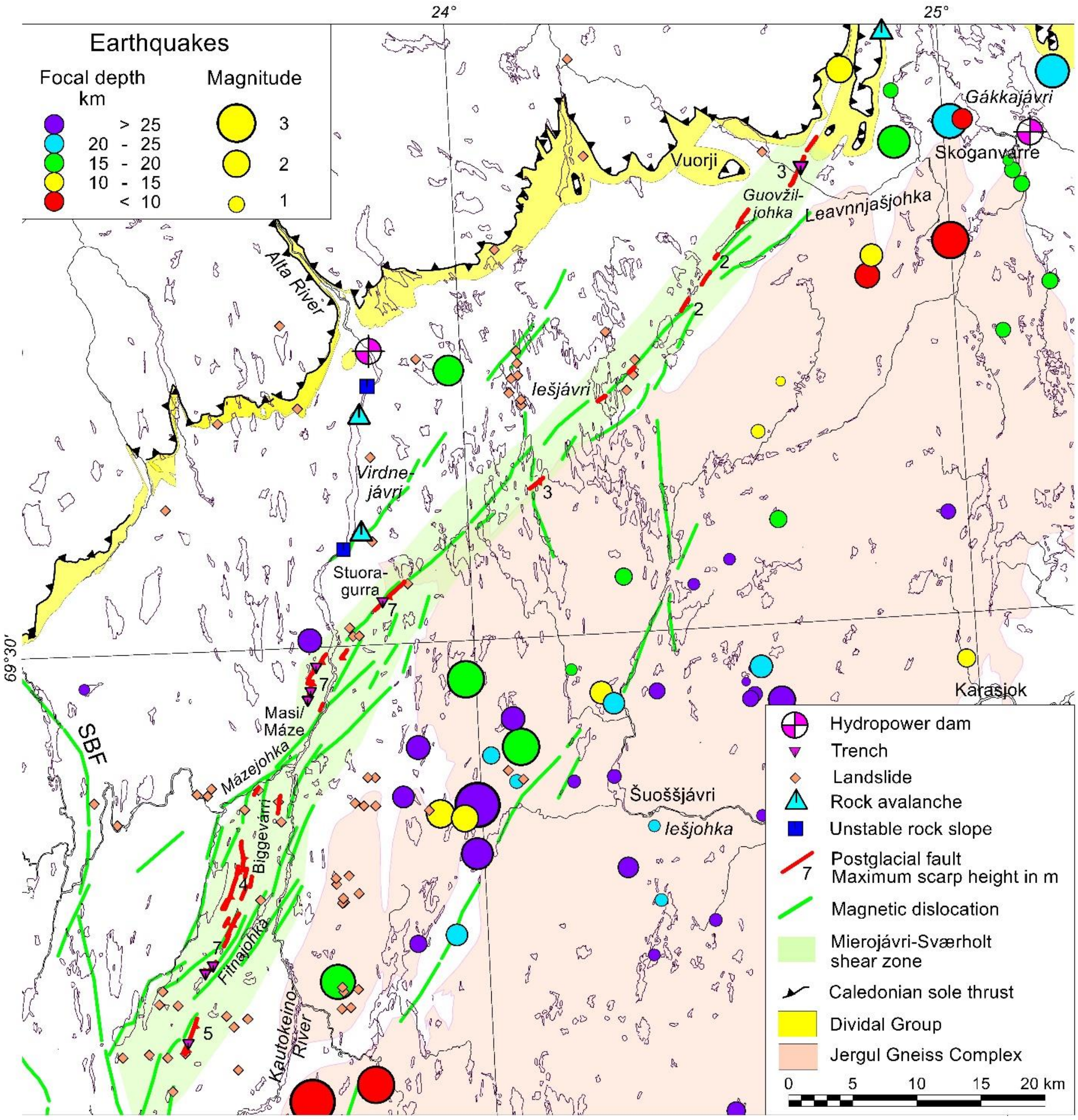

Figure 2. Simplified geological map of Finnmarksvidda (modified from Olesen et al. (2022) The 90 km long Stuoragurra Fault Complex (SFC) consists of three separate fault systems; the Fitnajohka Fault System in the southwest, the Máze Fault System in the central area and the Iešjávri Fault System to the northeast. The SFC occurs within the 4–5 km wide Mierojávri-Sværholt Shear Zone (MSSZ) that is located along the northwestern boundary of the Jergul Gneiss Complex (Olesen et al., 1992a). The MSSZ is also characterized by magnetic anomalies produced by the highly magnetic mafic intrusions (diabase, albite diabase and gabbro). An albite diabase south of Masi has been dated by Bingen et al. (2015) to 2220 ± 7 Ma. SBF – Soagŋojávri-Bajášjávri Fault (Olesen & Sandstad, 1993). Evidence of a total of 60 landslides is found within 20 km from the fault scarp. The earthquake epicentres are based on recordings at the ARCES seismic array immediately to the north of Karasjok in addition to seismic stations in northern Norway, and northern Finland.

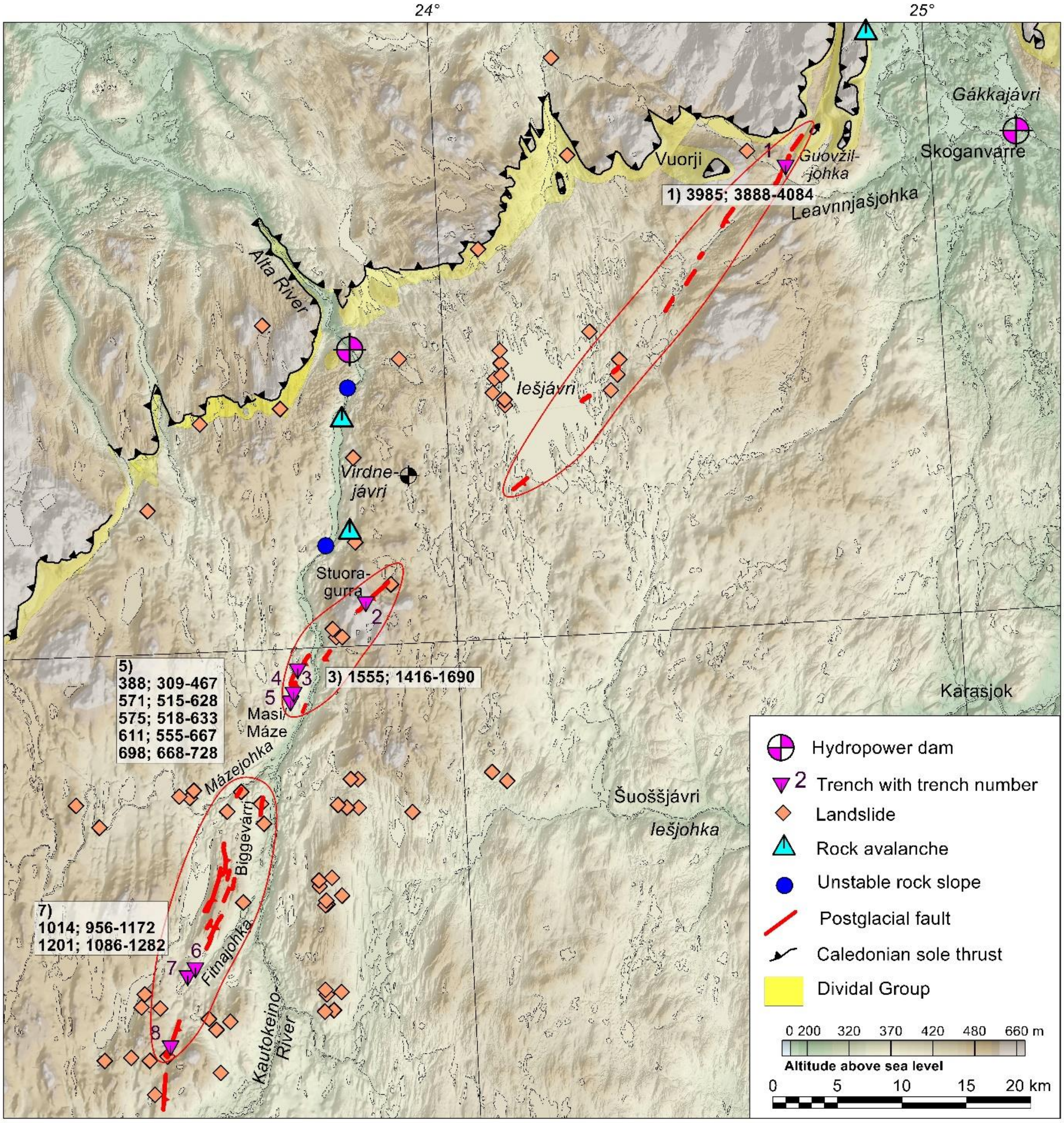

Figure 3. Location of trenching sites along the Stuoragurra Fault Complex, 1- Guovziljohka 2019 in the Iešjávri Fault System, and 2- Latnetoaivi 2020, 3- Masi 2021, 4- Masi 2020 and 5- Masi 2018-2019 in the Máze (Masi) Fault System, and finally, 6- Fitnajohka 1998, 7- Fitnajohka 2019, and 8- Ellajávri 2020 in the Fitnahohka Fault System. Figure map area is framed in Fig. 1 and includes most of the northern part of Finnmarksvidda, i.e., the relatively flat area 300–500 m a.s.l. close to the national border in the northernmost part of Norway. Radiocarbon dates relevant for age estimation of the youngest fault activity at four sites (1, 3, 5 and 7) are indicated with results in calendar years BP and shown for each dating with mean age and 2 sigma uncertainty age range. The ages indicated are maximum ages (1 and 5) and inferred maximum ages (3 and 7) for the associated faulting, respectively.

Siedlecka & Roberts, 1996; Bingen et al., 2015; Henderson et al., 2015). The seismic profiling (Olesen et al., 2022) shows that the regional MSSZ dips at an angle of c. 43° to the southeast and can be traced down to a depth of c. 3 km on the reflection seismic profile (Olesen et al., 2022).

The dip of the reverse postglacial faults as observed in trenches is 50–55° implying a maximum reverse displacement of approximately 9 m, which together with the 14–21 km length of the fault systems indicates associated earthquakes with a moment magnitude of 6.4–8.0 (Olesen et al., 2022), if single rupture events are considered.

The central part of the SFC in the Masi area occurs at the north-western boundary of the MSSZ while the southern and northern parts are in the middle of the fault zone. MSSZ (Fig. 2) constitutes the north-western margin of the Jergul Gneiss Complex (Siedlecka & Roberts, 1996).

The SFC is sub-parallel to the Caledonian front located 25 km farther to the northwest (Figs. 1 & 2) and similar sub-parallel setting is also observed for the postglacial Pärvie Fault (Lundqvist & Lagerbäck, 1976) located in northern Sweden (Fig. 1). The SFC seems to die out along the Guovžiljohka valley in the northeast. It is, however, possible that the fault complex extends farther to the northeast but is concealed underneath large boulder fields. The regional MSSZ continues, however, farther to the northeast and the Late Ediacaran to Cambrian Dividal Group is downfaulted by 100 m to the southeast along the MSSZ (Townsend et al., 1989; Siedlecka et al., 2011). The above-lying Caledonian nappes that were thrusted during the Silurian are, however, not offset. The MSSZ must consequently represent a long-lived fault-zone (Olesen et al., 1992a, 2022). Precambrian shear zones were reactivated in the Čáskejas area during the Timanian orogeny in the latest Ediacaran to early Cambrian (Andresen et al., 2014; Bjørlykke et al., in prep.).

The last regional glacial movements across Finnmarksvidda (for location, see framed area in Fig. 1, which cover a central part of Finnmarksvidda) during the last glaciation were mainly from S to N, with some small deviations locally, as indicated by e.g., the direction of drumlins and other streamlined glacial landforms, like flutes (Olsen et al., 1996). This is similar or close to the direction of some of the fault segments and may thus occasionally cause problems to separate glacial lineaments from fault lines in some areas.

The SFC and the Pärvie, Laisvall and Sorsele Faults in Sweden coincide with a physiographic border (Fig. 1). The mountainous area to the west of the Caledonian front has a higher elevation than the area to the east-southeast. The continental ice sheet was consequently thicker in the eastern area. This would involve more depression during the glacial period and consequently a greater contribution to the subsequent postglacial stress regime. The differential loading of ice across a pre-stressed fault line might consequently be sufficient to cause a reactivation of the faults and weakness zones (Olesen, 1988; Muir Wood, 1989; Olesen et al., 2022). This process cannot, however, explain the formation of the other postglacial faults in northern Fennoscandia.

The SFC crosscuts tills and glaciofluvial deposits (including an esker) on Finnmarksvidda (Olesen, 1988; Olesen et al., 1992b). A total of 60 landslide scarps (Fig. 2) are documented within 20 km from the fault scarp (Sletten et al., 2000; the majority reported by Olesen et al, 2022). Most of these landslides occur south of Masi.

The Stuoragurra faulting has produced distinct deformation and fracturing of the host rock. Percussion and core drilling in the Fitnajohka area revealed a dip of c. 40° to the SE at a shallow depth of c. 100 m (Olesen et al., 1992a, b, 2013; Roberts et al., 1997). The postglacial fault consists of few cm thick zones of clay minerals (fault gouge), within a 1.5 m thick interval of fractured quartzite. The clay zones contain kaolinite, vermiculite and smectite (Åm, 1994) and most likely represent a weathered fault gouge. Several 2–3 m thick zones of lithified breccia occur within a 25 m wide interval and reveal that the postglacial faults were formed within an old zone of weakness partly coinciding with the margins of deformed Paleoproterozoic albite diabases.

These c. 2,220 ± 7 Ma old dykes and sills (Bingen et al., 2015) are deformed due to later movements along the fault zone (Solli, 1988; Olesen et al., 1992a). The deformation is mostly related to the Svecofennian orogeny (c. 1,700–1,900 Ma). Magnetic modelling of the albite diabase in the vicinity of the drill holes shows a dip of c. 40° to the SE (Olesen et al., 1992a), consistent with the results from the drilling. Seismic refraction surveys and resistivity profiling (Olesen et al., 1992a) show both low seismic P-Wave velocity (c. 3800 m/s) and resistivity (c. 900 Ωm) and indicate a high degree of fracturing.

Trenching across the Fitnajohka Fault System was first performed in 1998, in a location that did not reveal buried organic materials suitable for radiocarbon dating (Dehls et al., 2000). The till above the SFC was folded forming a blind thrust (Dehls et al., 2000). Drilling and geophysical data revealed that the fault has a high groundwater yield (Olesen et al., 1992a, 2004) and Dehls et al. (2000) showed that high-pressure groundwater was injected more than 15 m into the till during the main rupture event at Fitnajohka.

Bungum & Lindholm (1997) recorded many earthquakes along the SFC. Focal mechanism solutions for five earthquakes recorded along or close to the SFC indicated that the maximum principal compressive stress, S_{Hmax}, is oriented on average NW–SE, i.e., approximately perpendicular to the strike of the SFC. The individual focal mechanisms were located at shallow depths southeast of the SFC surface expression. The reverse/oblique nodal planes were oriented so that one plane could be associated with the fault strike for all events; however, σ_H varied from N–S to E–W (averaging to NW–SE).

Olesen et al. (2022) estimated the earthquake moment magnitudes of the Fitnajohka, Máze and Iešjávri Fault Systems within the SFC from fault offset and length utilising formulas by Wells and Coppersmith (1994) and Moss & Ross (2011), provided that just one major rupture event was associated with each fault system. The moment magnitudes varied considerably, from 6.4 to 8.0 on Richter's scale. The estimates using the Moss & Ross (2011) equation for reverse faults give the highest magnitudes. Olesen et al. (2022) concluded that the three earthquakes associated with the formation of the three fault systems along the SFC were in the order of 6.4 to 8.0.

A total of c. 80 earthquakes were registered along the postglacial faults between 1991 and 2019 (Olesen et al., 2022, Fig. 2). The maximum moment magnitude is 4.0 and, due to the proximity of sensitive seismic stations, the catalogue is likely complete down to around magnitude 1.5. The focal depths vary between 5 and 32 km. Most events are located with a lateral and vertical uncertainty of 4 km or less. On the assumption of a c. 43° dip of the SFC and the Mierojávri-Særholt Shear Zone most of the earthquakes occur at a distance less than 10 km from these structures (Olesen et al., 2022).

Methods

Trenching and radiocarbon dating

New trenching and accompanying data collection were performed at Masi in 2018–2020, north of Masi in 2021, at Guovziljohka (Iešjávri Fault System) in 2019, and at Fitnajohka in 2019–2020. We have used trenching through the sediment overburden transverse to the Stuoragurra Fault scarps as our main method to reveal sediment structures affected by the fault event(s) (e.g., Dehls et al., 2000). Various sized trenches were excavated using 8–12-ton machine excavators. Sampling of sediments and buried organics has been performed with the intention of revealing the vegetation history based on the content of pollen (*study delayed due to lack of funding*) and macro plant remains, in addition to identifying terrestrial plant macrofossils suitable for radiocarbon dating. The sediment samples were wet sieved, before single plant fragments were hand-picked and attempted identified down to species level. The suitable samples were subsequently dried at 60°C overnight, weighed and sent for radiocarbon dating at the Poznan radiocarbon laboratory, Poland and Beta Analytic, USA. The reported ages were calibrated into calendar years with the OXCAL v.4.4 software (Bronk Ramsey, 2009) using the IntCal20 dataset (Reimer et al., 2020).

Georadar profiling

The Ground Penetrating Radar (GPR) technique is a fast, economic and non-destructive geophysical method with the potential to provide detailed and continuous images of the subsurface. Mapping of underground layers and/or linear features is based on the propagation and reflection of high frequency electromagnetic (EM) waves and later processing and interpretation of the resulting radargrams (Jol, 2009). Georadar profiling in the Fitnajohka and Masi areas have been used mainly to describe and evaluate the general appearance of the bedrock surface covered by Quaternary sediments along transects crossing the fault scarps. Data were acquired using the Malå RTA system (Snake), since it was easier for transport to the survey area and is more suitable for high inclination terrain. The Snake system utilizes an in-line antenna setting enclosed in a flexible cord that allows it to be maneuvered easily and efficiently through dense vegetation and uneven terrain without affecting ground contact. In this sense, several profiles were collected using the 100 MHz antenna, but only the one adjacent to the Masi trenching no. 4 (Fig. 3) is presented and used in this report. All profiles, included the one used here, intersected the superficial manifestation of the fault perpendicularly and data were collected starting uphill, on top of the fault escarpment, and walking down towards the base of the slope. Due to the inability to perform a Common Midpoint (CMP) measurement with the Snake system, no accurate velocity of reflected EM waves was possible to extract. However, the raw data do not present hyperbolic reflections that require collapsing, therefore all GPR results are presented unmigrated to avoid artefacts due to inaccurate velocity usage. Depth conversion was achieved with the use of default velocity 0.1 m/ns to give a general outlook of the dimensions of the targets. Data were converted to the desired format using ReflexW v.9.0.5 (Sandmeier Geophysical Research, 2019) and subsequently processed, modelled, and interpreted using EKKO_Project v.5 (Sensors & Software, 2018). Processing included namely bandpass and horizontal filtering, first break adjusting, de-wowing, background subtraction and SEC2 gaining. Positioning was extracted from handheld GPS tracks and topography was then sampled from detailed LiDAR data (www.hoydedata.no).

Plant macrofossil content

Samples from the trenching at Masi were analysed for their macro plant remains content, with the aim of increasing our knowledge about the Holocene history of the subarctic vegetation in Finnmark, particularly in the area close to Masi. Plant macrofossil analyses together with palynological studies provide an opportunity to infer and date palaeo-environmental and hydrological changes in the area. Detailed palaeoecological data, age-depth models, and a detailed reconstruction of the environmental conditions around the SFC will be further studied later and presented elsewhere. In the present report we describe only the results from the plant macrofossil analysis, which is relevant as general information of availability of ^{14}C-dating materials at Masi.

Study site / Research area

The location of the trenching site at Masi where the sediment samples were taken is indicated in Fig. 3 (Trench 5). Most of Finnmarksvidda is covered by mountain birch (*Betula pubescens* ssp.

czerepanovii) forest or tundra vegetation (e.g., *Betula nana* and *Empetrum nigrum* ssp. *hermaphroditum*) (Virtanen et al., 2016). The forest limit ranges between 400 and 500 m a.s.l. (Meier et al., 2005), and general climate data for the Masi area is indicated in Fig. 4. (www.senorge.no, 2016).

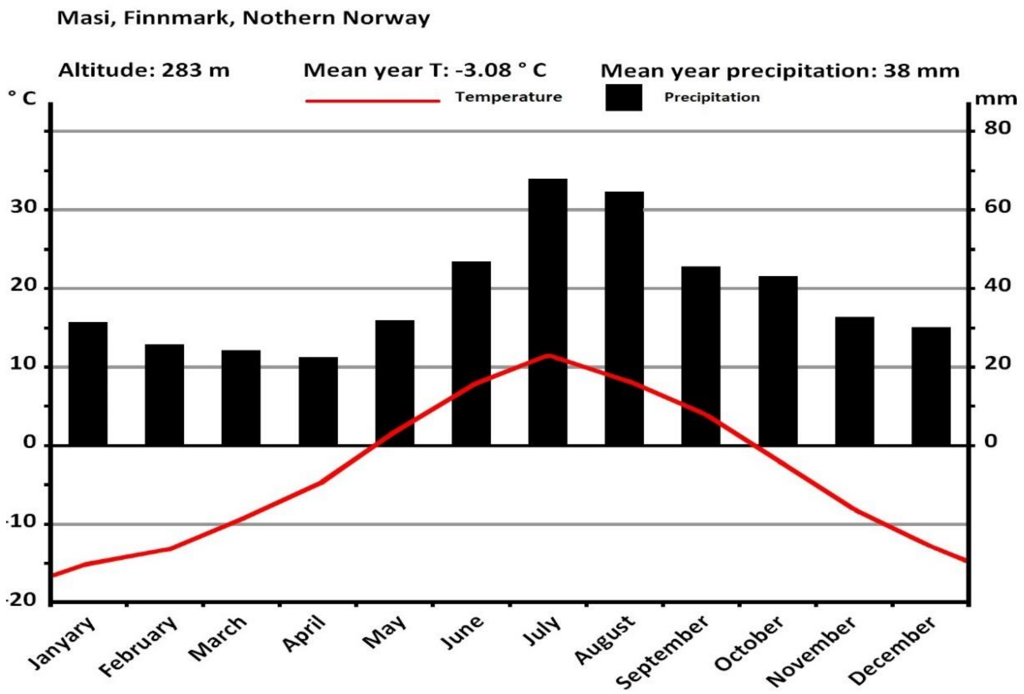

Figure 4: Climate diagram for the Masi area, Northern Norway. From seNorge.no, 2016.

Material and methods

The analyzed 18 samples listed in Table 1 were collected from the Stuoragurra Fault during a field campaign in August 2018. Obtained material was kept cold at c. 2–3°C and afterwards processed for plant macrofossil analysis.

Plant macrofossil analysis was performed following methods of Mauquoy et al. (2010) on the sub-samples of the known volume of sediments (20–25 cm^3) measured by water displacement. Samples were disaggregated with sodium pyrophosphate ($Na_4P_2O_7$*$10H_2O$) and each sample was washed through two sieves (125 and 250 μm) with a gentle spray of water. Then, the residue was suspended in water in a Petri dish and was examined under a stereomicroscope at about x10 – x20 magnification. The identification of fossil remains was performed using photographic references held by the DPCD UniGOE herbarium of the University of Tromsø and personal reference collection of plant macro remains.

Depth m	Age, cal yr BP, range 2σ	Sample number	Type of sediment - structure and colour
0.3	668-728	1-19	Modern peat, partly disturbed in lower part, dark grey to black
0.5	315-490	2-19	Deformed laminated lacustrine silt-sand with thin organic horizon, light grey to yellowish brown.
0.7	456-631	3-19	Deformed laminated lacustrine silt-sand with thin organic horizon, light grey to yellowish brown.
0.8	550-658	4-19	Deformed laminated lacustrine silt-sand with thin organic horizon, light grey to yellowish brown.
0.98	751-925	5-19	Deformed laminated lacustrine silt-sand with thin organic horizon, light grey to yellowish brown.
1.0	2350-2695	6-19	Deformed laminated lacustrine silt-sand with thin organic horizon, light grey to yellowish brown.
1.07	6275-6394	7-19	Buried peat with small pebbles and boulders, between peat and sand.
1.3	6314-6505	4B-18	Buried peat, partly disturbed, greyish brown to black.
1.5	8429-8753	3-18	Deformed till with lenses of sand with organic bearing material, peat remains, grey to bluish grey

Table 1. Sample depths, ages and descriptions of sediments revealed during trenching in 2018-2019 across the Stuoragurra Fault Complex at Masi, Finnmark, Northern Norway (See location in Fig. 3, Trench 5).

XRD and XRF analyses of fault gouge

XRD – X-ray diffraction

The mineralogical composition of all grain size fractions was studied with X-ray diffraction (XRD). Random-oriented samples were prepared by side-loading and analyzed with a Bruker D8 Advance X-ray diffractometer operating with a Cu X-ray tube (40 kV/40 mA) and Lynxeye XE detector. The XRD scan was performed from 3 to 75° 2θ with a step size of 0.02° 2θ, a measurement time of 1 s per step, and rotation speed of 30 per minute. Fixed divergence had an opening of 0.6 mm and primary and secondary soller slits were 2.5°. A knife edge was used to reduce scatter radiation. Mineral identification was carried out with the automatic and/or manual peak search-match function of Bruker's Diffrac.EVA V5.2 software using both Crystallographic Open Database (COD) as well as the PDF 4 Minerals database from the International Centre for Diffraction Data (ICDD). For further clay minerals study, oriented mounts of some fractions were prepared by letting 1 ml of sample suspension dry out on a glass slide. These slides were measured from 2 to 40° 2θ at room temperature, after treatment with ethylene glycol for 24 h, and after heating at 550°C for 1 h.

Mineral quantification was performed on randomly prepared specimens using Rietveld modelling with TOPAS 5 software. Refined parameters included crystallite size, unit cell dimensions, sample displacement, preferred orientation as well as background coefficients. The lower detection limits are mineral-dependent and estimated to be 1-2 wt% with an approximate uncertainty for the Rietveld modelling (i.e., quantification) of at least 2-3 wt%.

A sample of fault gouge from Ellajávri, south-southwest of Masi (sample 2020-#198469) was analyzed with XRD for its mineral composition. The results [wt%] are given in Table 5 (See the next section: Results and interpretation).

XRF – X-ray fluorescence

A representative amount of crushed, homogenized and pulverized sample material was used for geochemical analysis. Loss on ignition was determined by heating 2-3 g of the pulverized sample in a porcelain crucible to 1000 °C for at least one hour. The chemical composition was determined by X-ray fluorescence (XRF). Glass beads were prepared by fusing 0.6 g of sample material with 4.2 g of lithiumtetraborate ($Li_2B_4O_7$). XRF measurements were performed on a sequential wavelength-dispersive PANalytical Axios equipped with a 4 kW Rh-tube. Detection limits range between 0.01 to 0.5 wt% for major elements with varying uncertainties depending on element and concentration range.

K-Ar dating

The potassium–argon (K-Ar) dating is a well-established method for determining ages of potassium bearing rocks and minerals. It is based upon the radioactive isotope of potassium (^{40}K), which naturally decays into a stable daughter isotope of argon (^{40}Ar) (Mitchell, 1972; Weaver, 1980). This means that the method can only be used when potassium-bearing minerals are found in the sample. In the present case (Table 5), there is mainly smectite that contains potassium.

All sample preparation was performed at the NGU laboratory. The finer than sand fractions of the samples were transferred to graduated cylinders using more Type II pure water, and the <2 µm and 2-6 µm fractions were successively isolated using Stokes' law. Two successive separations were performed to increase the yield of the <2 µm fraction. The <2µm fractions were centrifuged with a Beckman-Coulter Avanti J-26S XP centrifuge fitted with a JCF-Z continuous flow rotor for generating 0.6–2 µm and <0.6 µm fractions. All fractions were dried in freeze drier and homogenized.

All K-Ar analyses were performed at the NGU laboratory. Air-dry clay materials and standards were wrapped in molybdenum envelopes, and the net mass of the aliquots was determined using a Mettler Toledo XPE26DR microbalance fitted with an antistatic ionizer. Molybdenum envelopes were subsequently loaded into an ultra-high vacuum extraction line and baked at a maximum temperature of 120°C to eliminate excess water following the recommendations of Clauer & Chaudhuri (1995).

Argon was extracted from the aliquots in a Pond Engineering double vacuum resistance furnace at 1400°C for 20 minutes. During heating, bulk sample gas was expanded directly into a stainless-steel vessel housing a freshly activated Titanium Sublimation Pump, to strip the sample gas from most reactive gases including H_2O, N, O, CO and CO_2 (O'Hanlon, 2005). A known molar amount of pure ^{38}Ar spike (Schumacher, 1975) was prepared using a 0.2 cc gas pipette attached to a 4-litre reservoir and was mixed with the purified sample gas. The gas mixture was subsequently isolated in a second clean-up stage and exposed for 10 minutes to two SAES GP50 getter cartridges with ST101 Zr-Al alloy, one of which was kept at 350°C and one at room temperature, to remove residual reactive gases including H_2 and CH_4.

Argon isotope ratios were determined on an IsotopX NGX multi-collector noble gas mass spectrometer using faraday cups fitted with 10^{12} Ω amplifiers, except for 40Ar which was measured using a faraday cup fitted with a 10^{11} Ω amplifier. Time-zero beam intensities were measured for 30 cycles of 20 1-second integrations, and time-zero intensities were calculated using exponential regressions back to gas inlet time. Furnace blanks were run regularly between samples, and generally had Ar compositions close to atmospheric argon. Instrument mass discrimination was determined using aliquots of argon purified from air and compared with the reference value of 298.56±0.31 (Lee et al., 2006). The ^{38}Ar spike pipette was calibrated using GA-1550 biotite with $^{40}Ar^*$=1.342±0.007 x 10-9 mol/g (McDougall and Wellman, 2011) and HD-B1 biotite (Fuhrmann et al., 1987) with a $^{40}Ar^*$=3.351±0.01 x 10-10 mol/g (Charbit et al., 1998). The overall standard deviation of the pooled spike calibrations by combined GA1550 and HD-B1 is <0.3 %. The accuracy of the $^{40}Ar^*$ determinations was monitored within batch by HD-B1 biotite.

Potassium concentration was determined by weighing sample aliquots of 50 mg the same day in the same humidity conditions as the sample for Ar analysis. Aliquots were digested in $Li_2B_4O_7$ flux at a temperature of 1,000±50 °C in palladium crucibles. The resulting glass was subsequently dissolved in HNO_3 and analysed on an Agilent 5110 VDV ICP-OES. 1σ uncertainties are estimated from the reproducibility of a range of standards with K concentrations between 0.12%K and 8.3%K and considered the signal strength of K during analysis. Mean standard deviations of all measured standards overlap with published reference values and their published standard deviations.

K-Ar ages were calculated using the ^{40}K decay constants, abundance, and branching ratio of Steiger & Jaeger (1977). Atmospheric argon corrections were performed using the relative abundances of ^{40}Ar, ^{38}Ar and ^{36}Ar of Lee et al. (2006; $^{40}Ar/^{36}Ar = 298.56 \pm 0.31$). Uncertainties were estimated using the error equation for multi-collector isotope dilution measurements from Halas & Wojtowicz (2014) modified to consider the uncertainty on mass discrimination.

Results and interpretation

Trenching and radiocarbon dating

The aim of trenching was to locate buried peat and gyttja that existed prior to the faulting event, perform radiocarbon dating of samples from the buried organic material, and thus would provide a maximum age estimate for the event. The trenching at Masi revealed deformed sediments, gyttja and peat layers (Figs. 5 & 6A, B), which we believe were buried and deformed during the main fault event. Radiocarbon dates of macro plant remains from the buried organics and from the base of the topmost 20–30 cm of the modern surficial peat, which is deformed at least in its lower part, indicate that the main young faulting event seem to have occurred after c. 569 cal. years BP (N=5)(Table 2), which is a mean of five dates, all from c. 20–30 cm depth in the surficial modern peat directly over deformed sand lenses, sample positions 1, 2 and 3 in Fig. 7A and age ranges based on 2σ standard deviation precision given in Table 2 and Fig. 3. This is based on the observation that sand wedges and lenses from the deformed sediments are injected into the existing surficial peat during the main fault event (Figs. 6, 7 & 8).

An attempt to illustrate how we think the overall stratigraphy could have been in the loose material overburden on the footwall side before the faulting event (or events) occurred, is presented in a simplified stratigraphic log (Fig. 7B).

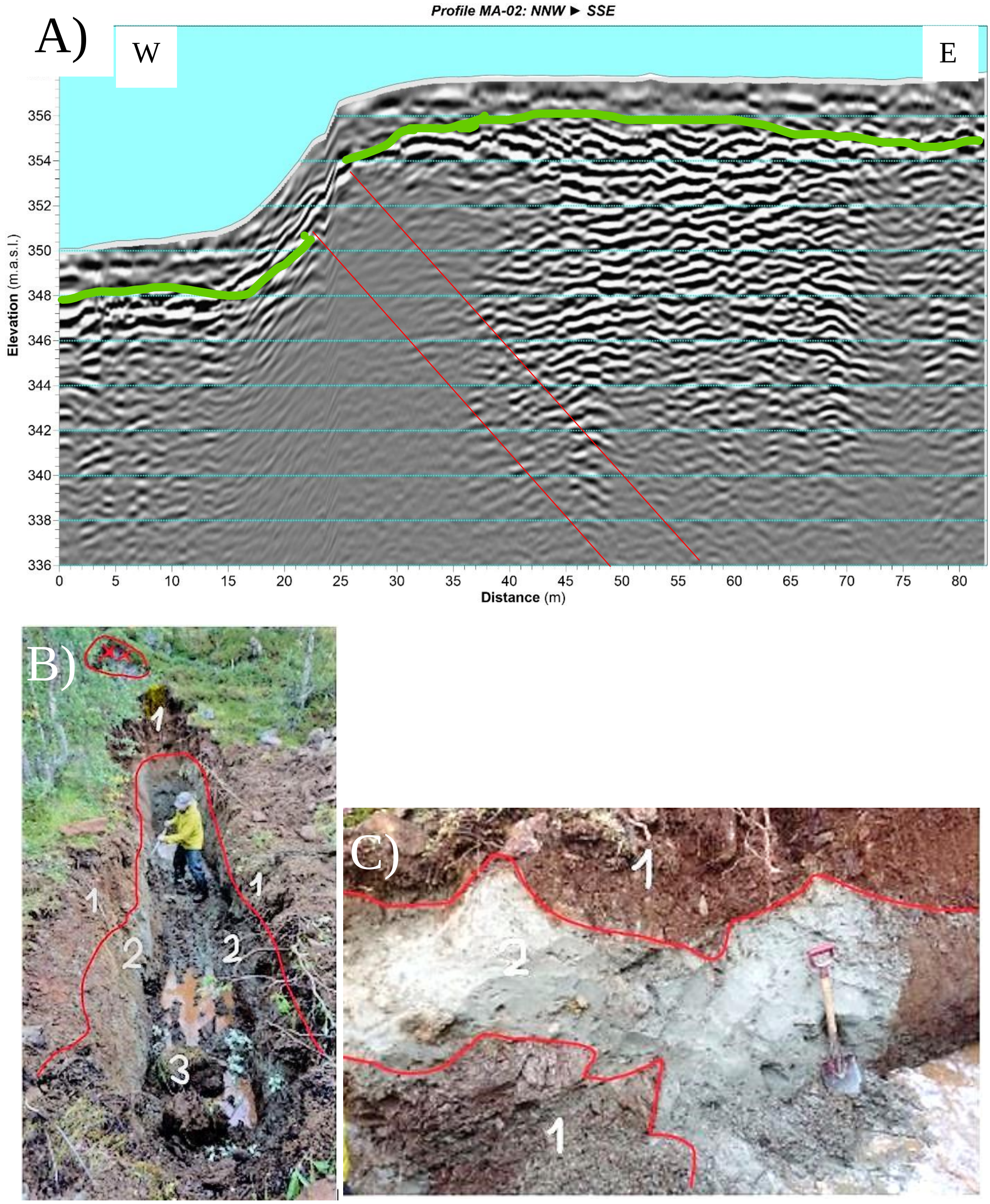

Figure 5. A) Georadar profile transverse to the Stuoragurra Fault scarp at Masi, along Trench 4, from AD 2020. Approximate boundary between overburden and bedrock indicated by green line, and fault planes (not visible in the profile) indicated with red lines. For location, see Figs. 3, 9 and 10 (Trench 4). B) Trenching transverse to the fault scarp, with brownish fault breccia (1) adjacent to the hang wall just above the head of the person, deformed greyish overburden (2) in the trench walls, and buried peat (3) at the base. Exposed hanging wall nose indicated by red x-es (encircled). C) Close-up of deformed sediments (2) with lenses and overlying wedge of reddish-brown fault breccia (1) in the side wall of the trench transverse to the fault scarp.

No.	Pos.; Fig. 7A	Field ref.	Lab. ref.	14C-yrs BP ± 1σ	Cal. yrs BP, mean	Cal. yrs BP, 2σ ranges	Comments
	Recent peat, slightly deformed, c. 20-30 cm depth just above deformed lavcustrine sediments and buried peat						
1	2	MASI, STUOR 1-2	Poz-114130	325 ± 30	c. 388	95:4%: 309-467	Macro-plant remains, unspecified
2	1	MASI3-240820-1	Poz-128923	545 ± 30	c. 571	95:4%: 515-628	Leaves and stick, unspecified
3	1	MASI3-240820-2	Poz-129481	555 ± 30	c. 575	95.4%: 518-633	Sticks, unspecified
4	3	MASI1-240820-2	Poz-129478	645 ± 30	c. 611	95.4%: 555-667	Bark, unspecified
5	3' (2)	MASI, Stuor 1-1	Poz-114129	765 ± 30	c. 698	95.4%: 668-728	Sticks and bark, unspecified
	Mean age of 5 samples from c. 20-30 cm depth:			567 ± 30	**c. 569**	513 (min); 625 (max)	Fault deformation younger than this age
	Upper part of deformed lacustrine sediments						
6	between 2 & 4	MASI2-030919	Beta-543856	190 ± 30	c. 220	78%: 137-302	Macro-plant remains, unspecified
7	between 2 & 4	MASI6A-300818	Poz-110597	200 ± 30	c. 222	83%: 139-306	0.35 mgC; macro-plant remains
8	between 2 & 4	MASI2B-300818	Poz-110598	200 ± 30	c. 222	83%: 139-306	0.6 mgC; macro-plant remains
9	between 2 & 4	MASI3-030919	Beta-543857	270 ± 30	c. 358	89.1%: 281-435	Macro-plant remains, unspecified
10	between 2 & 4	MASI2C-300818	Poz-114132	350 ± 30	c. 402	95.4%: 315-490	0.6 mgC; macro-plant remains
11	between 2 & 4	MASI 2-19, 3-19	Poz-129480	490 ± 50	c. 543	95.4%: 456-631	0.09 mgC; Salix bark and Equisetum fragm.
12	4	MASI4-030919	Beta-543858	620 ± 30	c. 604	95.4%: 550-658	Macro-plant remains, unspecified
13	5	MASI2-290818	Poz-110596	945 ± 35	c. 838	95.4%: 751-925	0.11 mgC; stick of birch
	Mean age of 8 samples from deformed sed.:			408 ± 35	**c. 427**	346 (min); 507 (max)	Contamination from roots is possible here
	Lower part of deformed lacustrine sediments and buried peat						
14	3	MASI1-240820-1	Poz-128921	2415 ± 30	c. 2522	94.5%: 2350-2695	Bark, unspecified
15	6	MASI2-240820-1	Poz-128922	2800 ± 30	c. 2877	95.4%: 2789-2966	Stick and bark, unspecified
16	6	MASI2-240820-2	Poz-129479	2825 ± 30	c. 2927	95.4%: 2850-3004	Bark, unspecified
17	7	Masi6B-300818-1	Poz-137244	4810 ± 50	c. 5531	95.4%: 5459-5604	Spheroidal Carbonaceous Particles (SCPs)
18	7	MASI6B-300818	Poz-106547	5510 ± 35	c. 6334	95.4%: 6275-6394	0.3 mgC; macro-plant remains
19	8	MASI4A-300818	Poz-110561	5660 ± 40	c. 6409	95.4%: 6314-6505	Wood of birch
20	9	MASI4B-300818	Poz-110560	6030 ± 40	c. 6866	95.4%: 6749-6983	Twig, unspecified
21	10	MASI2A-300818	Poz-106545	6150 ± 40	c. 7036	95.4%: 6909-7163	Macro-plant remains, unspecified
22	11	MASI3-290818	Poz-110595	7810 ± 50	c. 8591	95.4%: 8429-8753	Twig of birch
23	12	MASI1A-300818	Poz-110563	8150 ± 50	c. 9135	95.4%: 8997-9273	Twig of birch

Table 2. 23 radiocarbon dates from the Masi trenching site (Fig. 3, Trench 5). Most dating samples are unspecified macro plant remains. Potential roots from modern plants, if observed, have been removed prior to selection of material for dating. However, samples between positions 2 and 4 in Fig. 7A are considered to possibly be affected by modern roots, though not observed in the dating samples. Dating no. 5, with field ref. MASI, Stuor 1-1 is from a position slightly under position 2 in Fig. 7A and is correlated to position 3. Dating no. 11 (MASI 2-19, 3-19) is from fragments of identified plants (Salix bark and Equisetum), and it shows similar age as the accompanying dates (c. 400-600 cal. years BP) from bulk macro unspecified plant remains from close lying samples. Dating no. 14 (MASI 1-240820-1), is from the deformed lower part of the recent peat and is inferred to represent reworked older material injected into the recent peat during the fault event. Its age deviates significantly from the 13 other dates from the basal part of the recent peat and underlying deformed sediments, and it is therefore put below these in the table. Mean ages are calculated as weighted means between maximum and minimum ages in the 2σ uncertainty age range intervals and are in most cases very close to the associated mean ages in the calibration table presented by Reimer et al., 2020.

Deposition of the laminated lacustrine sediment overlying the buried peat at Masi (E and F in Fig. 7A; and originally partly overlying and partly adjacent to peat in Fig. 7B) requires a damming by a few dm and up to c. 2 m, i.e. (Fig. 9A, B), before the major fault event occurred. The damming event may have resulted from landslide and blocking of the outlet, induced by earthquake, with or without an accompanying reverse fault. The bedrock is not exposed in the damming area, so there is no direct visible indicator of an earlier fault event represented there.

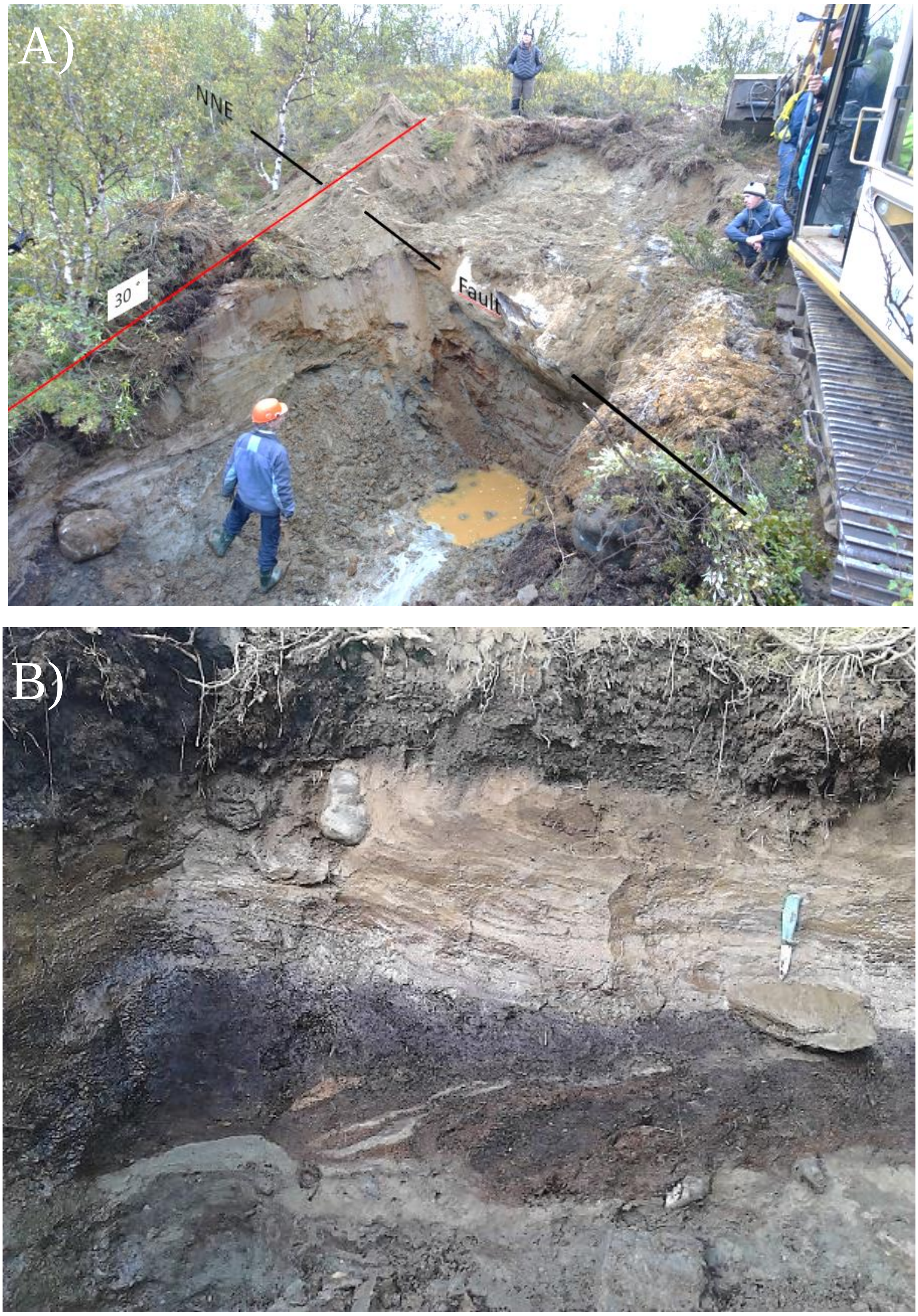

Figure 6. A) Trenching transverse to fault scarp associated with the Masi Fault System in the Stuoragurra Fault Complex, just north of Masi (5 in Fig. 3). Up-thrown part of bedrock from the reverse fault is exposed in the central part of the photograph. The hanging wall or fault plane is dipping c. 50˚ to the right (ESE). Fault breccia, visible in the central part of the photograph, is in contact with the bedrock hanging wall. The fault breccia is produced, pushed, and injected during the fault event into the sediment overburden, with deformation and burial of sediments and organics as a result. B) Partly deformed surficial peat overlying deformed layered lacustrine sand, buried peat and till and glaciofluvial sediments in the 2018-trenching at Masi (5 in Fig.3).

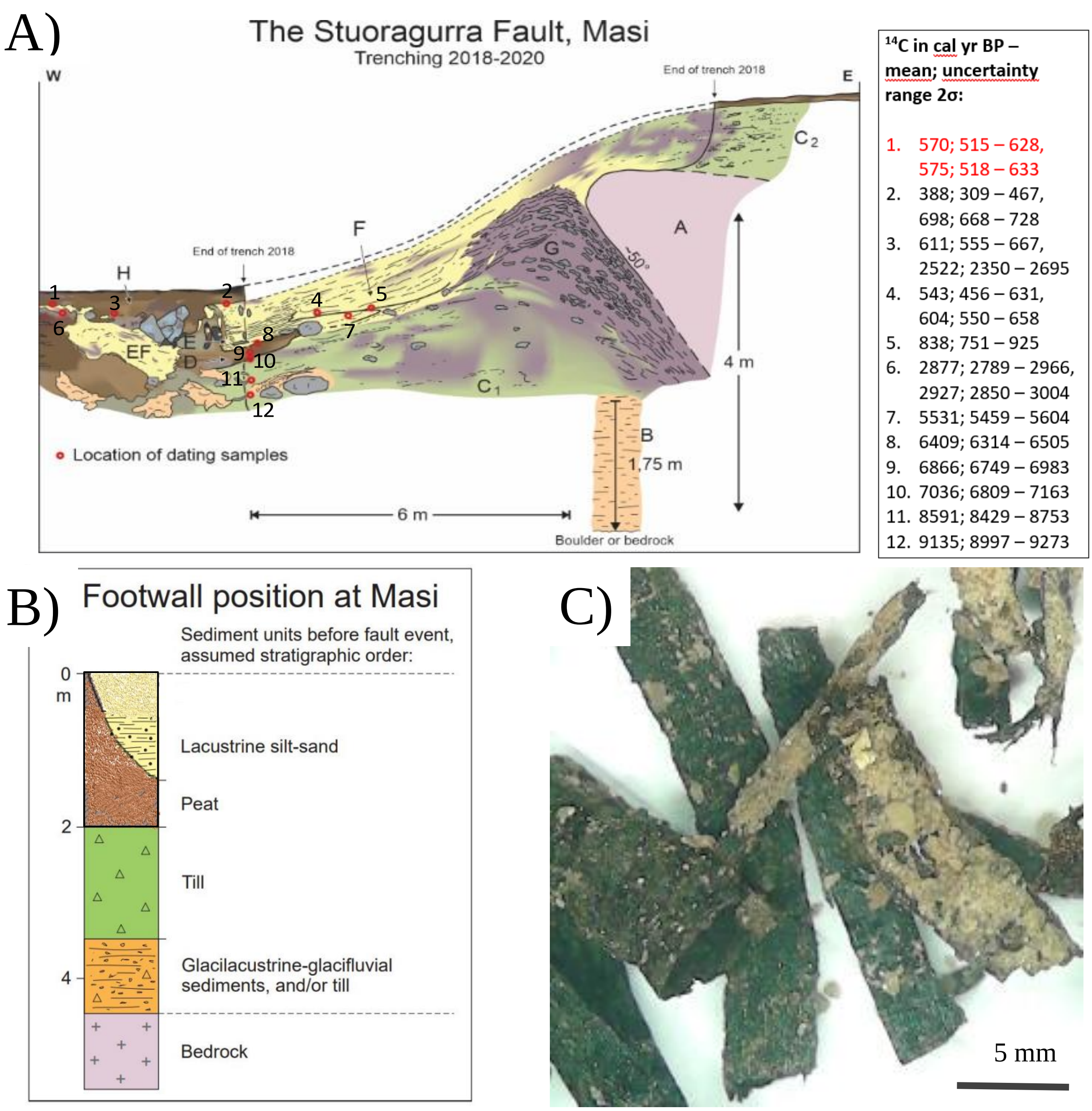

Figure 7. A) Outline of the trench (Trench 5 in Figs. 3 and 10) across the Máze Fault System (within the postglacial Stuoragurra Fault Complex) in the southern part of the Juŋkorajeaggi swamp located 1.5 km to the north of Masi (Figs. 2, 3, 9 and 10). The orientation of the section is normal to the fault. The nose of the up-thrown block of bedrock (A) is buried by deformed basal till (C_1 and C_2) with deformed lacustrine sand (with thin gyttja layers) (E and F) and modern mainly undeformed peat (H) on top. B represents glaciolacustrine or glaciofluvial sediments (silt and fine-grained sand). Unit D is buried and deformed peat, and unit G is wedges of fault breccia (diamicton with angular rock fragments) injected into the sediment overburden during the fault event. The base layer of the modern peat (H), as well as organic material, mainly plant remains, from the deformed and buried gyttja and peat (from units C_1, D, E and F) are sampled for ^{14}C dating. Positions and numbers of dating samples are shown in the profile, and the results are also given in Table 2 (included some dates where modern contamination is considered possible). Total Holocene peat thickness, less than 0.5 m west of the profile shown in A, is recorded to be c.2.0-2.5 m. Highlighted results (red) are discussed in the main text. B) Inferred stratigraphy of overburden on the footwall before the last major faulting event happened. C) Examples of dating materials (mainly from birch) from the deformed lacustrine sediment units E & F (Fig. A).

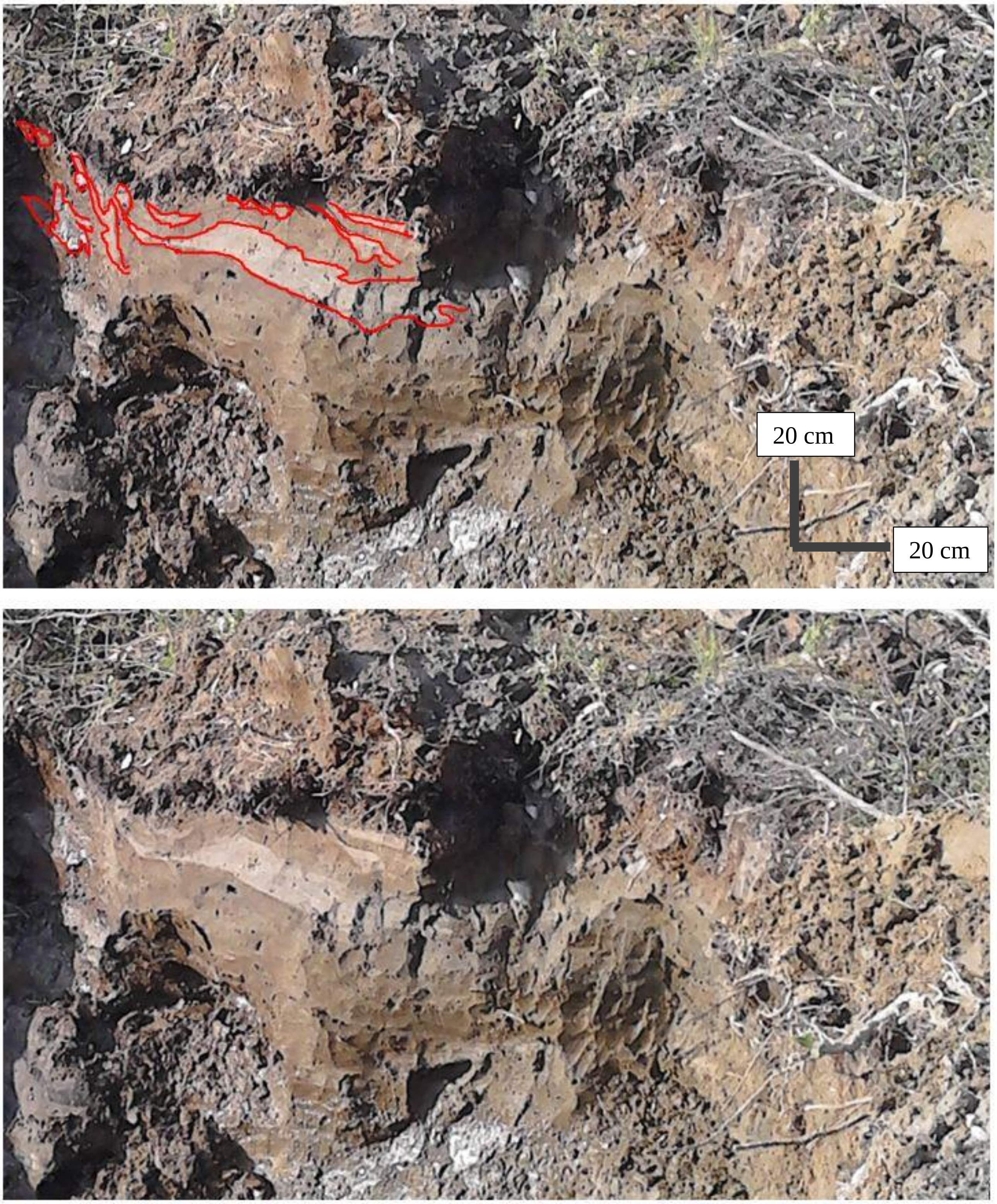

Figure 8. Injections of lacustrine silt-sand (outlined with red colour) into the surficial peat, up to c. 20 cm below surface. Lower part of these 20 cm of surficial peat must therefore have existed during injection made by push outward (left) and upward from the youngest faulting activity. Location of picture is in the left flank of the profile in Fig. 7A.

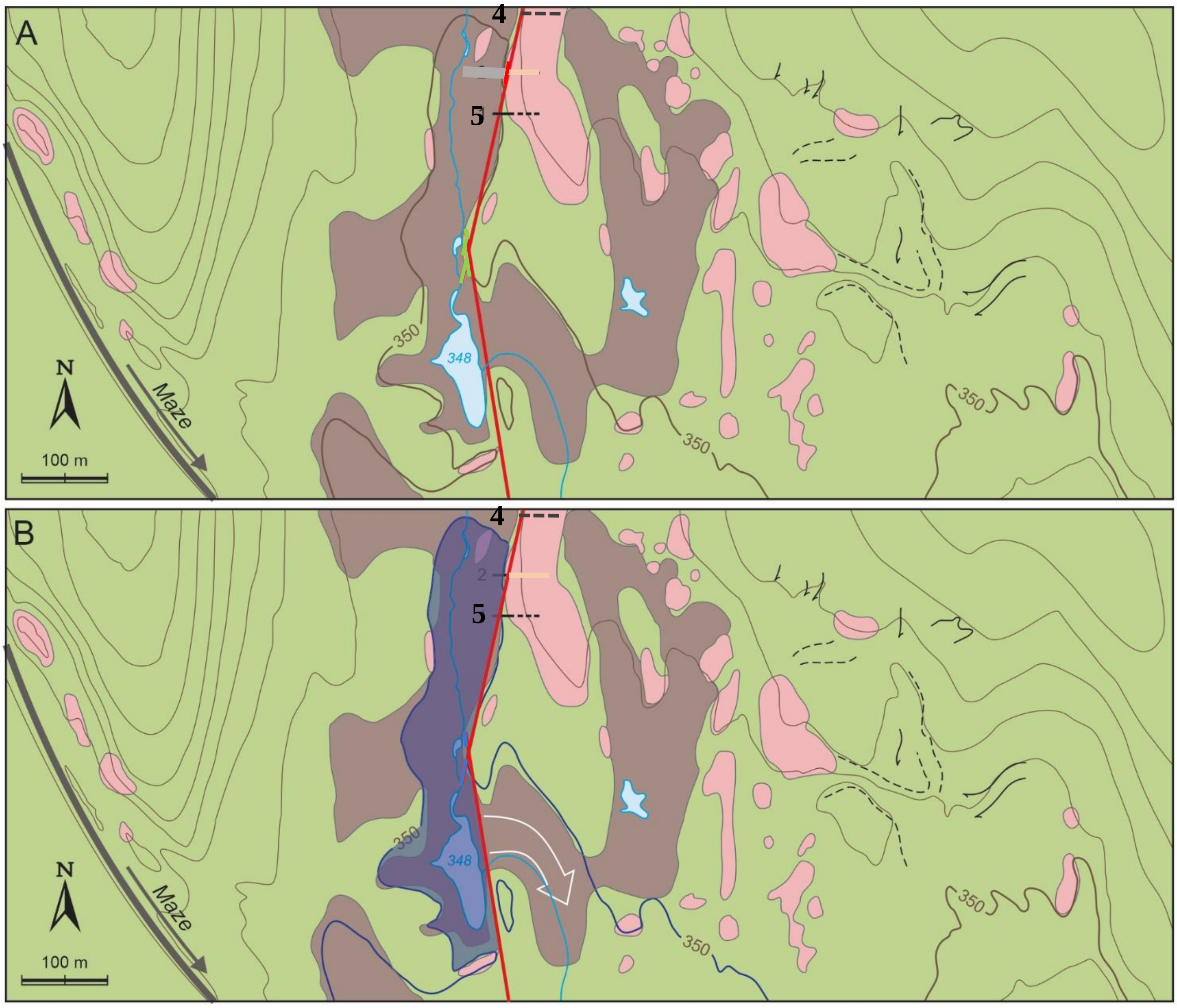

Figure 9. A) Location of Trenches 4 and 5 (in Figs. 3 & 10) and E-W trending georadar profiles (stippled lines) across the Stuoragurra Fault (SF) north of Masi, and 350 m a.s.l. contour around the basin adjacent to the NNE trending fault scarp. The outlet zone (white arrow) was dammed along the fault (red lines) up to this level to allow for deposition of lacustrine sediments (E and F) upon the buried peat indicated in Fig. 7. B) Same as in A with lineaments along the SF and location of trenching sites and georadar profiles. Maximum dammed area indicated with blue shading. Loose deposits occur in the damming area, i.e., no bedrock exposures where the fault lineament crosses the mire.

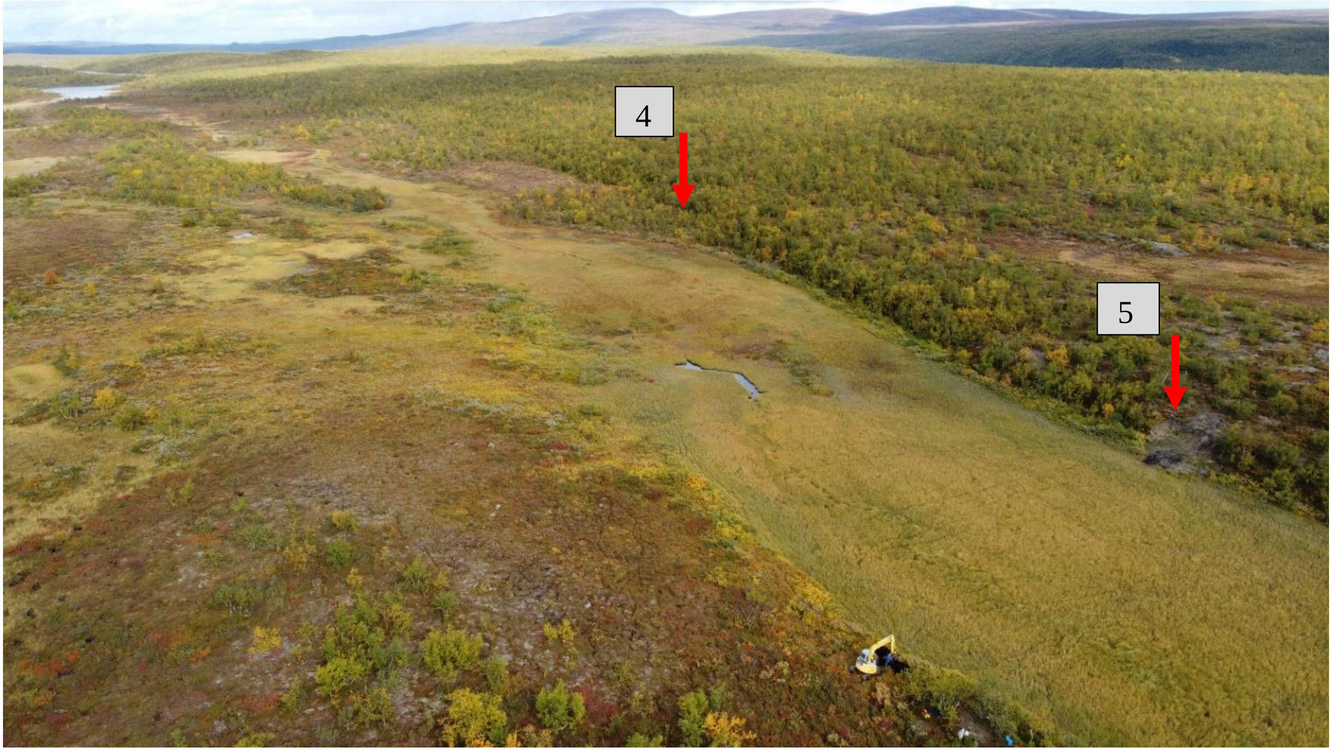

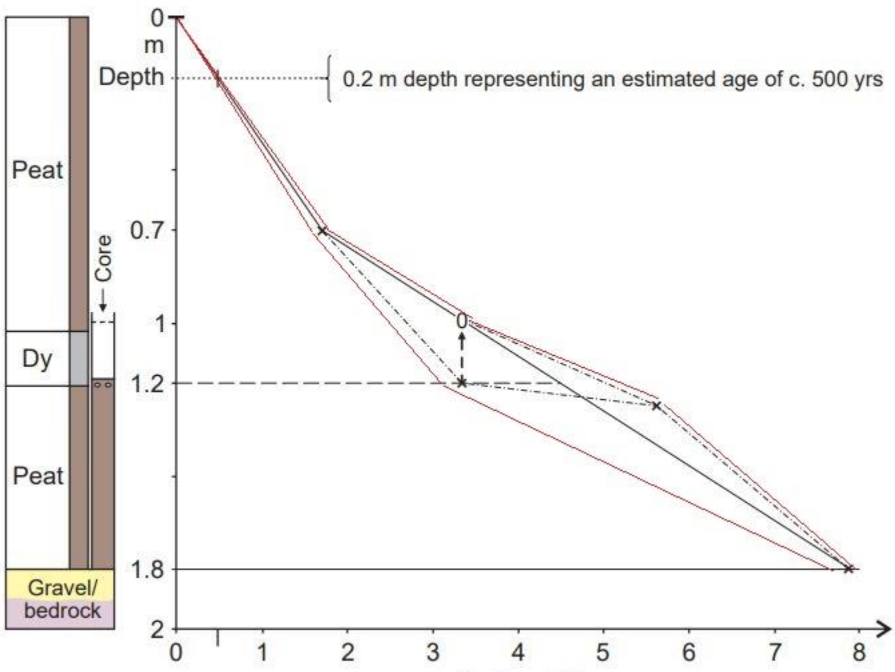

Figure 10. A) (above) Drone picture of a mire along the N-NNE trending SF escarpment NW of Masi with location of Trenches 4 and 5 (see also Fig. 3) shown with red arrows. Position of undeformed peat stratigraphy is represented by the machine excavator west of the mire, c. 50–60 metres from Trench 5. Latnetoaivi and Stuoragurra can be seen as a depression in the horizon above the "4" label. B) (below) Simplified log of the undeformed peat at the western flank of the mire, with location indicated by machine excavator in A. An approximal age-depth curve of the peat from the base to the top is drawn based on four ^{14}C-datings of macro plant remains, with mean ages in cal yr BP plotted with symbol x in the diagram, and uncertainty range 2σ indicated with red lines. Dating results are included in Table 3 (nos. 33-36).

Multiple discontinuous wedges of un-consolidated, normal fault breccia injected in the overburden were observed during trenching in 2020 (e.g., Fig. 5C; Trench 4 in Fig. 9A), and some of these may have their origin from a small older reverse faulting event. However, we have not been able to separate these structures clearly from the total deformation pattern.

The damming event is likely to have happened around 3000 years before present, which corresponds with the youngest age obtained from the top of the buried peat, and approximately the oldest age obtained from gyttja in the deformed overlying lacustrine sediments as well (Fig. 7A, sample location 6). The sample location 7 in the lacustrine represent a re-deposited lump of peat eroded from the buried peat, which is consequently considered to be much older than the lacustrine sediments.

No.	Field ref.	Lab. ref.	14C-yrs BP ± 1σ	Cal. yrs BP, mean	Cal. yrs BP, 2σ ranges	Comments
24	Guovz4-300819	Beta-540040	3650 ± 30	c. 3986	95.4%: 3888-4084	Macro plant remains, buried peat
25	Guovz3-300819	Beta-543862	5710 ± 30	c. 6513	95.4%: 6410-6617	Macro plant remains, buried peat
26	Guovz1-300819-2	Beta-543866	7880 ± 30	c. 8723	95.4%: 8591-8856	Macro plant remains, buried peat
27	Guovz2-300819	Beta-543861	8010 ± 30	c. 8890	95.4%: 8773-9007	Macro plant remains, buried peat
28	Guovz1-300819-1	Beta-543865	8150 ± 30	c. 9126	95.4%: 9009-9243	Macro plant remains, buried peat
29	Masi3-11/9-21	Beta-606448	1660 ± 30	c. 1553	95.4%: 1416-1690	Bark fragments
30	Fitna3-020919-2	Beta-543864	1120 ± 30	c. 1014	95.4%: 956-1172	Macro plant remains, buried peat
31	Fitna3-020919	Beta-543863	1260 ± 30	c. 1201	95.4%: 1086-1282	Macro plant remains, buried peat
32	Fitna 2020-1	Poz-129483	5820 ± 40	c. 6621	95.4%: 6529-6734	Macro plant remains, buried peat
33	Masi 1-30/8-21	Poz-145156	1765 ± 30	c. 1644	95.4%: 1571-1718	Undeformed peat, twigs
34	Masi 2-30/8-21	Poz-145237	4895 ± 35	c. 5644	95.4%: 5583-5716	Undeformed peat, twigs, leafs
35	Masi 3-30/8-21	Poz-145238	3030 ± 30	c. 3216	95.4%: 3083-3347	Core, peat, twigs, leaf
36	Masi 4-30/8-21	Poz-145239	6970 ± 40	c. 7809	95.4%: 7693-7925	Core, peat, twigs, leaf
37	Masi SE 10/9-21	Poz-145421	Modern	Modern		Gyttja, young slide, min. age
38	Masi N 1-11/9-21	Poz-145422	Modern	Modern		Surficial peat, base layer
39	Masi N 2-11/9-22	Poz-145423	1830 ± 30	c. 1727	95.4%: 1631-1823	Gyttja, young slide, min. age
40	Rass 2020-4	Poz-128858	Modern	Modern		Surficial peat, base layer
41	Rass 2020-3	Poz-128857	3020 ± 30	c. 3242	95.4%: 3143-3341	Landslide 2, max. age
42	Rass 2020-2	Poz-129527	7660 ± 35	c. 8462	95.4%: 8388-8537	Landslide 2, min. age
43	Rass 2020-1	Poz-129482	8580 ± 50	c. 9578	95.4%: 9481-9676	Landslide 1, min. age

Table 3. 12 radiocarbon dates of macro plant remnants from Guovziljohka (1; dating 24–28), Masi (3; dating 29) and Fitnajohka (7; dating 30–32) trenching sites (1, 3, 7 in Fig. 3), from undeformed peat (dating 33–36) west of the mire on the footwall side of Trench 5 north of Masi (Fig. 3), and from three landslide localities: west of the mountain Rassegalvarri (close to Trench 8; dating 40–43), west of Trench 3 (dating 38–39) and southeast of SFC at Masi (dating 37). Mean ages calculated as described in the caption to Table 2.

We have recorded the total peat thickness to be 1.8 m in the undisturbed peat some 60 m west of the SFC (Fig. 10A, B), just across the mire adjacent to this fault at Masi, Trench 5 (Figs. 3, 7A & 9). The base of the peat here at the western flank of the mire is dated to c. 8 cal. kyr BP. The peat is supposed to be deeper in the middle of the mire and started most likely to accumulate there shortly after deglaciation some 10,000 years ago. The oldest radiocarbon date from the deformed and buried sediments of c. 9,100 cal. years BP (Table 2) in the eastern flank of the mire, where the peat thickness reaches at least 2.5 m close to Trench 5 (Fig. 7A), supports this hypothesis. This means that the uppermost 20 cm of the peat represents c. 10% of the total recorded peat thickness, and it represents most likely much less than 1,000 years (c. 10%) of the total peat accumulation period (postglacial time), due to compaction of the peat with depth and less organic production, less peat accumulation, during the earlier parts.

Trenching with radiocarbon dates of buried or deformed older organic material from Fitnajohka (Fig. 11), Masi N (Fig. 12) and Guovžiljohka (Fig. 13) (Table 3) indicate that the fault events may have happened at different times at the different locations; younger than c. 600 years ago at the Máze Fault System, around or after c. 1,280 cal. years BP at the Fitnajohka Fault System and after c. 4,000 cal. years BP at Guovžiljohka in the northern part of the Iešjávri Fault System (Olsen et al., 2020) (Fig. 3) (Table 2: nos. 1-5; Table 3: nos. 24, 30-31). The interpretation that the fault event is younger than the dated age of the peat at 20 cm depth in Trench 5 at Masi (Fig. 3) is based on the observed wedges of sand which is injected to this level horizontally or slightly upward into the existing surficial peat during faulting event (Figs. 7A & 8). A similar interpretation is suggested for the Fitnajohka data (Fig. 11), but the sand wedge there is discontinuous, and the age of the faulting there may therefore, if the 'wedge' is somehow dropped as a sand spot on the peat surface, although no observations support a process like this, and not injected into the peat, possibly be slightly older than the base of the peat just above the sand wedge. The interpretation of the age of the faulting at Trench 3 north of Masi (Fig. 12) is also less straight-forward than the one at Trench 5 at Masi. This is because the dated bark fragments sampled from the top of a few mm thick silt-sand blanket draped upon the fault breccia on the footwall found in Trench 3 are inferred to be re-deposited organics together with the thin silt-sand blanket, just after impact of fault breccia upon the adjacent lake bottom. During impact the lacustrine silt and sand, together with organic remains, would be whirled up in the water and then slowly settled upon the fault breccia outlier when the movement calmed down. This would give a thin blanket of silt-sand with organic remains, including, e.g., fragments of bark on top, just as it is recorded here (Fig. 12). If not re-deposited, then the age of the bark fragments may indicate an age slightly younger than the fault event there, i.e., about 1500–1600 years BP (Table 3: no. 29). If re-deposited as we suggest, then the faulting is younger there. The age of the fault event at Guovžiljohka (Fig. 13) is more straight-forward to suggest since it must be younger than the top of the buried peat there.

Fault breccia observed at and in the trenches

Lithified fault breccia and injected wedges of unconsolidated, normal fault breccia characterise the contact zone with the up-thrown bedrock block and the adjacent deformed sediment overburden. This is observed both at Fitnajohka in the Fitnajohka Fault System and at Masi and Latnetoaivi in the Máze

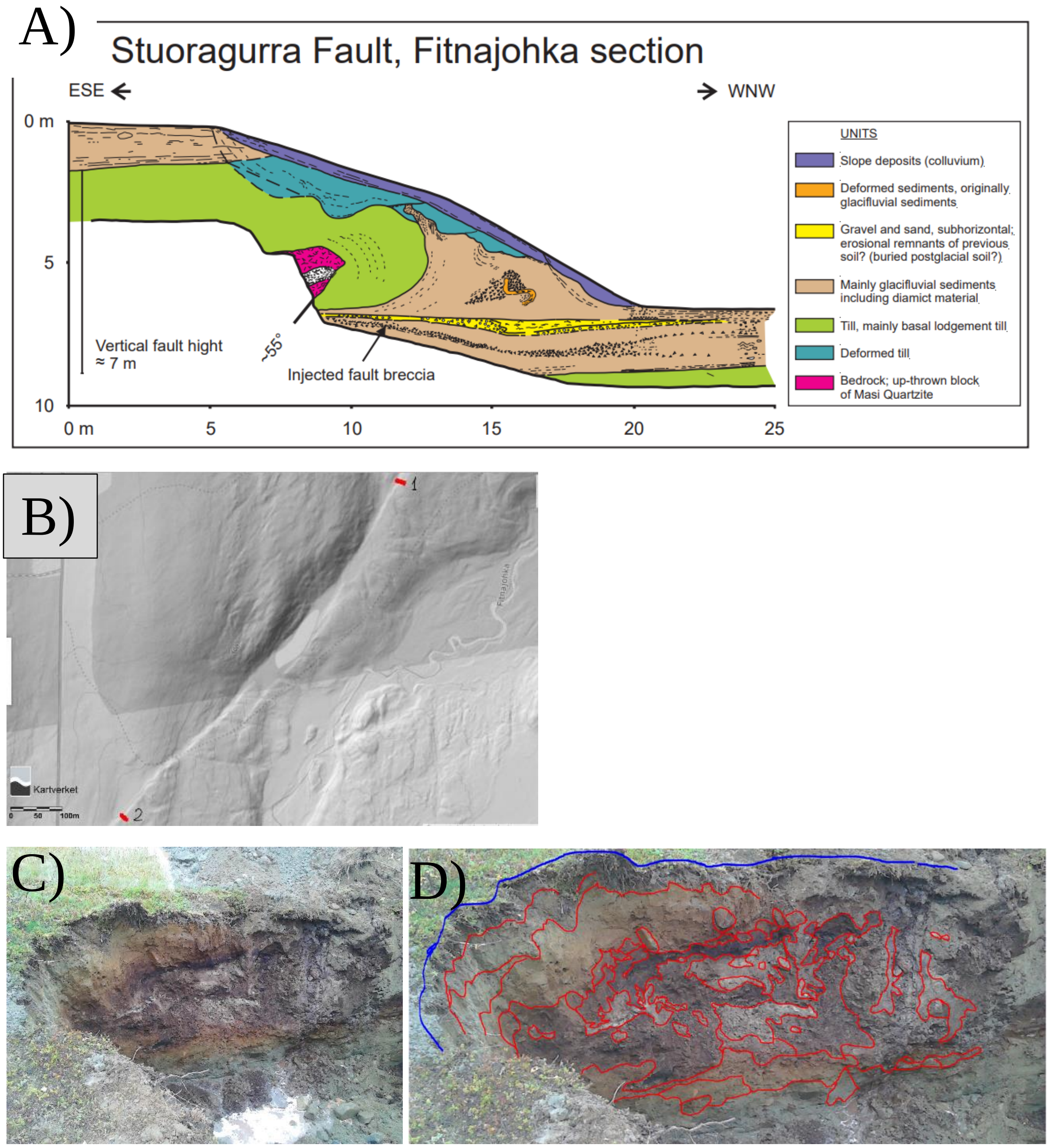

Figure 11. A) Section with stratigraphy revealed during trenching in 1998 transverse to NNE-trending scarp in the Fitnajohka Fault System. The orientation of the section is normal to the fault. The nose of the up-thrown block of bedrock (red) is buried by deformed till (green and blue) and glaciofluvial gravel and sand (beige, orange and yellow), with colluvial slope deposits (violet) on top. From Dehls et al. (2000). B) LiDAR image with fault lineaments and location of 2019-trenching site (2) across the scarp in the Fitnajohka Fault System, just 750 m southwest of the trenching site from 1998 (1) (Fig. A). C) (left) Base of scarp slope and stratigraphy with deformed organic bearing sediments in the lower end of the 2019-trench transverse to the NE-trending scarp in the Fitnajohka Fault System. The section is c. 2 m high. Location of trench is shown in Fig. B (2). D) Boundaries of the various deformed parts of the organic bearing sediments are shown with red lines, and surface or top of wall sections indicated with blue line. ^{14}C-datings of macro plant remains in organics overlying sandy lenses injected into the adjacent surficial peat 2-3 metres outside the scarp slope indicate that the fault event occurred either close to 1300 cal. years BP, or after that age (Table 3; nos. 30-31).

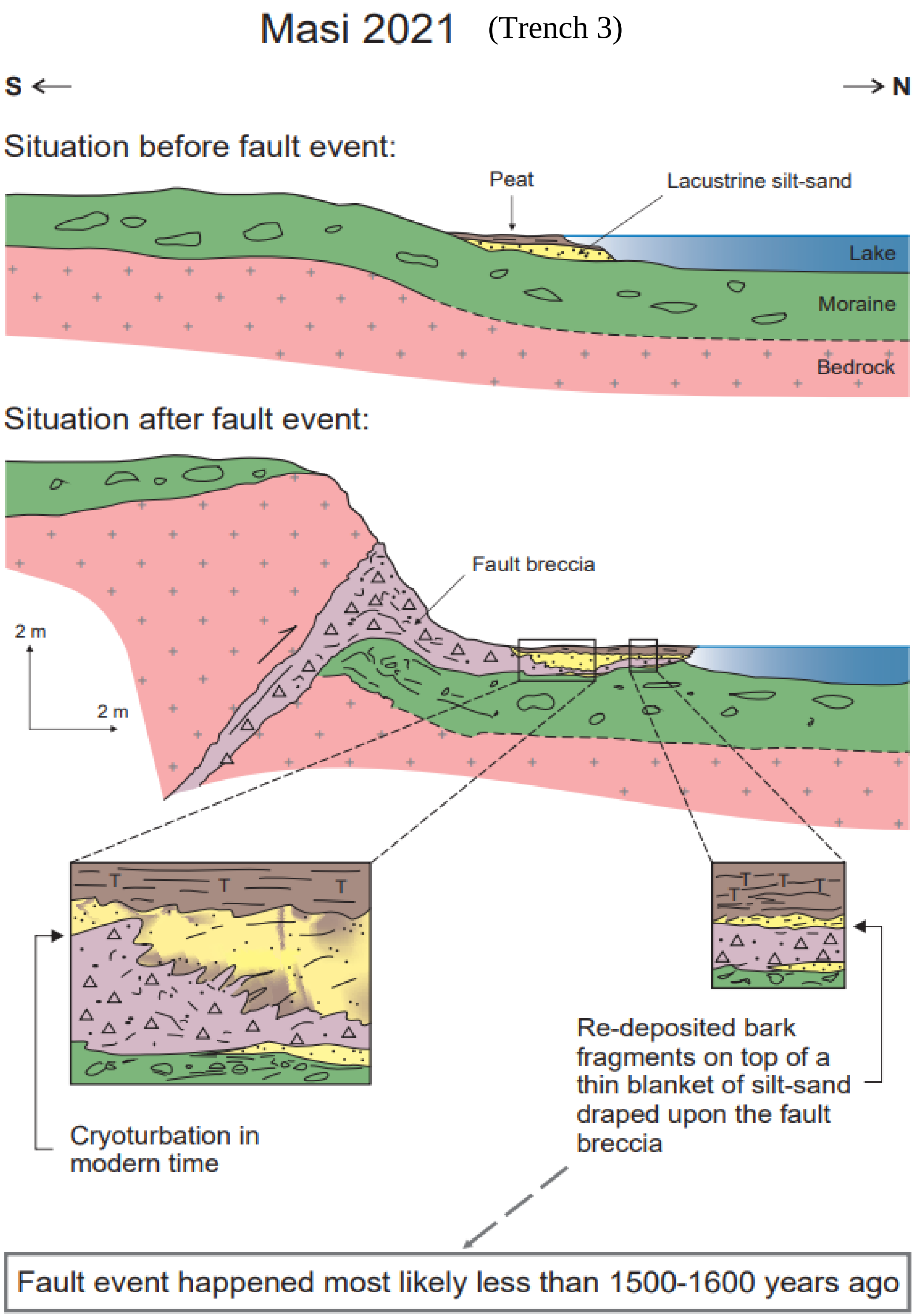

Figure 12. Sketches of stratigraphic profiles indicating assumed situation just before and actual situation after the last faulting along SF north of Masi. The latter is based on trenching perpendicular to the fault scarp in 2021 AD (Trench 3, Fig. 3). The till - bedrock boundary in the footwall area is however not directly observed, just inferred from surrounding areas. Result of ^{14}C dating of bark fragments included in Table 3 (dating no. 29).

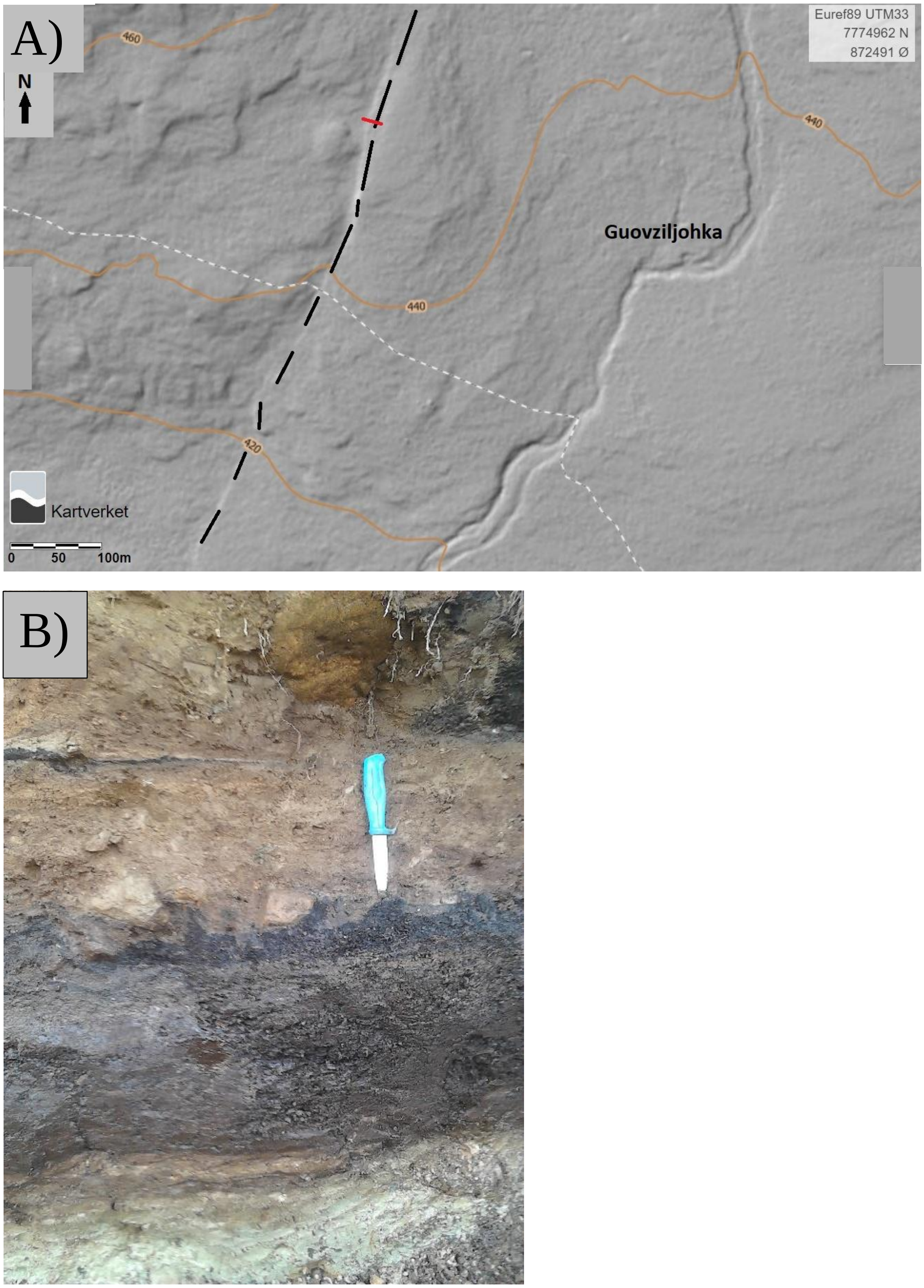

Figure 13. A) LiDAR image with location of trenching in 2019 (red line) transverse to the fault scarp (stippled) at Guovziljohka in the Iešávri Fault System. B) Lower part of scarp slope, with stratigraphy in the side wall of the trench transverse to the fault scarp at Guovziljohka in the Iešjávri Fault System in the north-eastern part of Finnmarksvidda (1 in Fig. 3). Deformed sediments are surrounding a buried peat layer. Deformation direction from left to right, normally to the SSW-NNE fault direction. ^{14}C dating from the top of the buried peat showed that the fault event has happened after 4,000 cal. years BP (Table 3: no. 24).

Fault System (Figs. 3, 5–7, 11–12 & 14–18). In addition, angular blocks of local bedrock type have been spread out from the nose of the up-thrown bedrock to at least 15–20 m distance from the fault scarp (Figs. 14B & 16A). Fracturing from the exposed hanging wall nose, followed by sliding downward the slope would not alone explain the long distance from the scarp for some of the blocks. Therefore, it is thought that the angular blocks located farthest from the scarp are somehow thrown out during the fault event. The wedges of fault breccia consist of mainly angular clasts of local bedrock type, and they are reaching several metres out from the fault scarp (Fig. 15A, B, C). Lithified fault breccia from the bedrock in the fault area clearly reveals a much older fault history and suggests that the postglacial Stuoragurra Fault Complex represents a reactivated part of a several hundreds of millions of years old tectonically active zone (Fig. 15D, and Olesen et al., 2022).

Georadar profiling (GPR)

A GPR radargram from the Masi area, along Trench 4 (Fig, 3), present a maximum penetration depth of about 10–12 meters with the intensity of reflectors varying laterally (Fig. 5A). Most of them presents sub-horizontal layering of intertwining sediments that locally reach larger depths in form of vertical columns. Such vertical features require attention because they may not indicate geological changes, but instead shifts in signal intensity due to violent jumps of the antenna sensors on the rough terrain. All data present a top layer of more irregularly shaped reflectors that is 2 meters thick by average. However, the most interesting feature in the GPR radargram is the almost complete lack of reflectors in the area where the fault scarp is found. Moving from higher to lower elevation, reflectors either gradually decrease in depth or become abruptly interrupted until background noise takes over and no reflectors are detected. This non-reflector area is usually about 20 meters wide and almost always gives place to downslope reflectors that appear similar both in terms of thickness and overall structure to their upslope counterparts. Even though GPR is generally unable to map the true inclination of the fault scarp since penetration is generally interrupted almost vertically as soon as the zone is met, the reflectors before and after this blank area can be thought of as a clear indication of the displacement that took place. Other structural elements detected by the GPR can only be extracted by directly comparing the results to trenching, and in the actual case shown in Fig. 5 it is possible to interpret the thickness of the overburden both on the footwall and hanging wall surfaces to be c. 2-3 m. This is confirmed by trenching. In addition, the scarp height of 7 m observed in the terrain and confirmed by LIDAR data (www.høydedata.no) is also reflected from bedrock displacement perpendicular to the fault scarp as seen in the GPR profile (Fig. 5A).

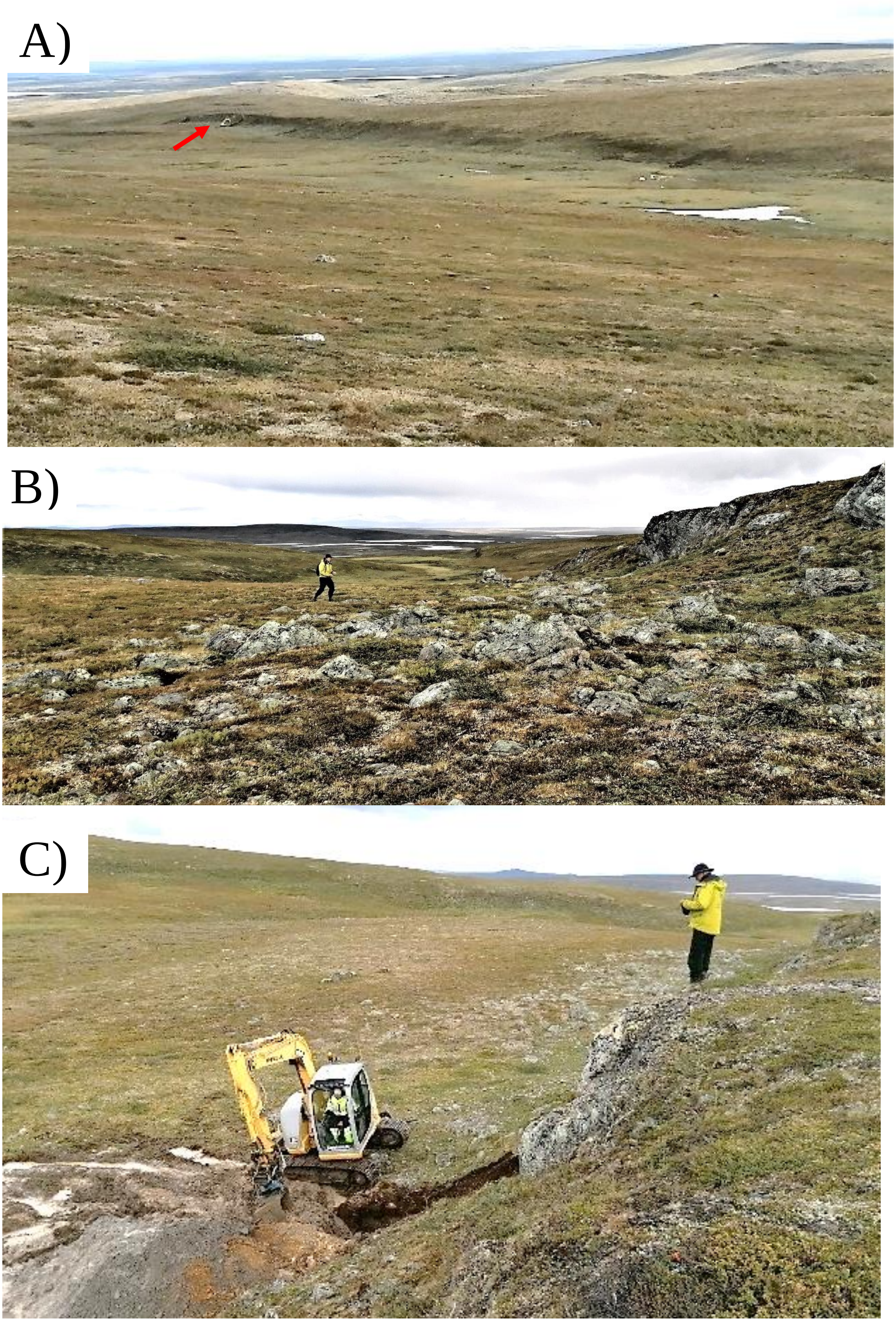

Figure 14. A) The Stuoragurra NNE-trending (left) fault scarp at Latnetoaivi, in the Máze Fault System. An 8-tons machine excavator is located at the trenching site at the foot of the the fault scarp, to the left (red arrow), and is used as scale here. B, C) Fault scarp along the Stuoragurra Fault at Latnetoaivi in the Máze Fault System. Scarp height is c. 7 m. A 15–20 m wide belt of angular blocks thrown out from the wall of the up-thrown bedrock during the fault event is located on the ground surface along the scarp (foreground in B and upper right part in C).

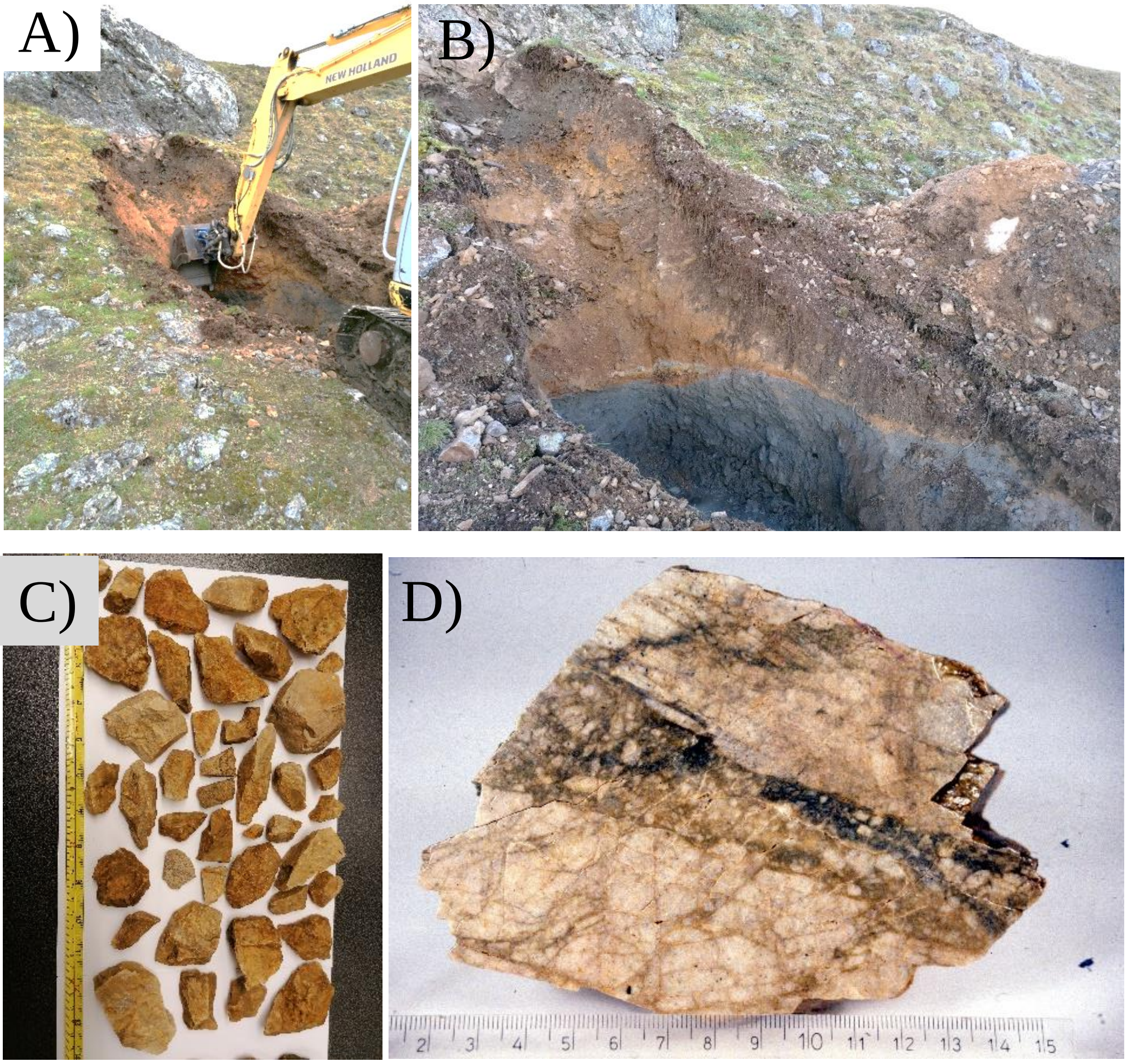

Figure 15. A) Trenching transverse to Stuoragurra Fault scarp at Latnetoiavi NE of Masi (2 in Fig. 3). The hanging wall block of quartzitic bedrock is exposed on top, penetrating through the sediment overburden, with fault breccia (brown) overlying till (dark grey). B) Fault breccia (brown) overlying till (dark bluish grey) in the trenching at Latnetoaivi, a cleaned section of the trenching also shown in A. The vertical section from the exposed bedrock on top and downwards to the bottom of the trench is c. 3 m. C) Angular clasts of quartzite from bedrock at Latnetoaivi trenching site, i.e., clasts from wedges of fault breccia, and D) lithified fault breccia from bedrock in the Stuoragurra Fault Complex zone (fragment indicated is from the Fitnajohka Fault System).

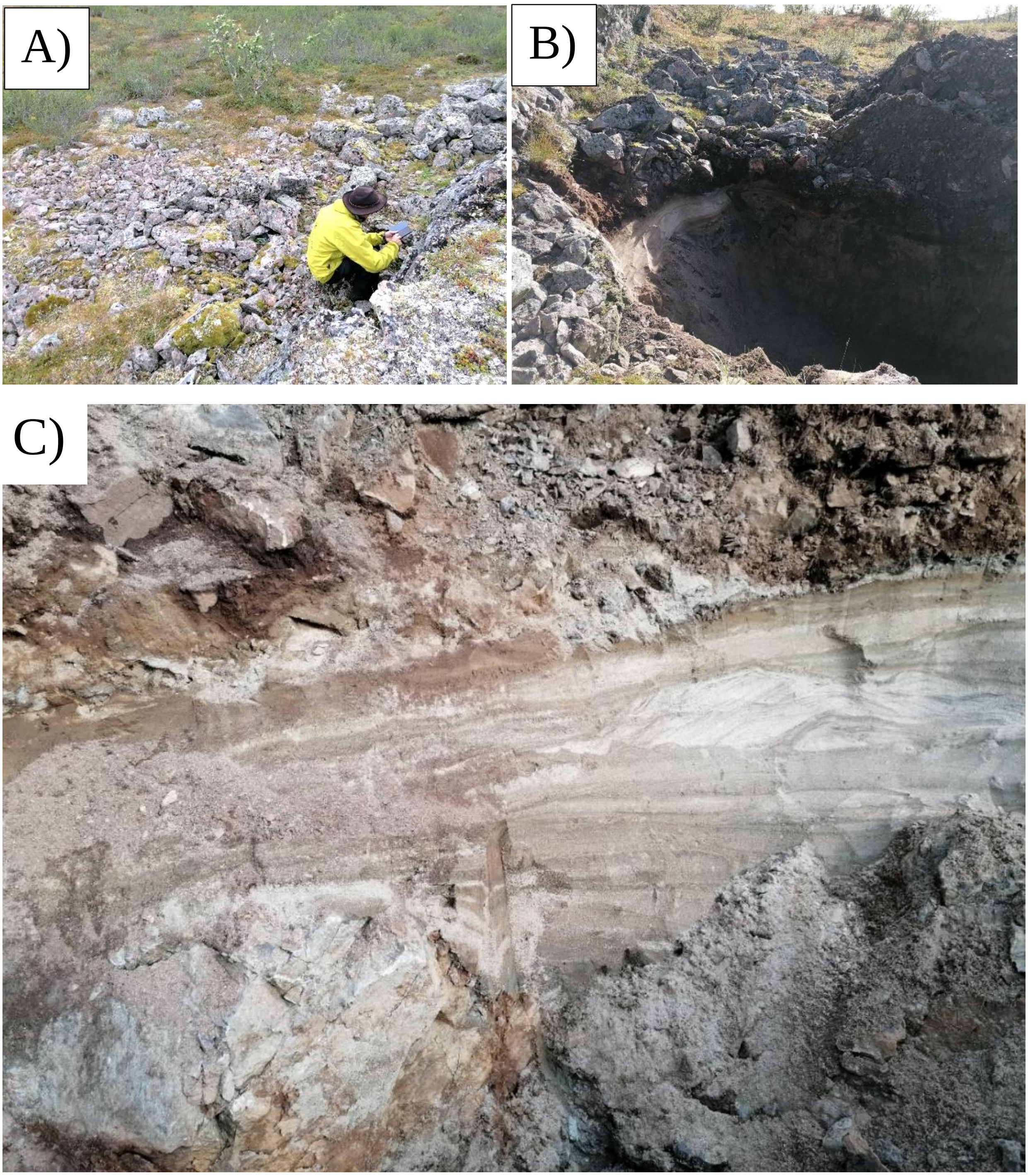

Figure 16. A) Belt of angular blocks representing the open-work part of the fault breccia in front of the fault scarp at Ellajávri in the southernmost part of the Fitnajohka Fault System (8 in Fig.3). The up-thrown part of the bedrock is exposed to the right. B) Trenching transverse to the fault scarp at Ellajávri. Exposed bedrock of up-thrown part to the upper left, with adjacent angular blocks as part of the fault breccia which continues downwards and outwards from the scarp. The fault breccia is interfingering with the underlying deformed sediments, with an originally layered glaciofluvial sand unit visible in the left, middle part of the picture. C) Close-up of a part of the deformed glaciofluvial sand unit shown also in B.

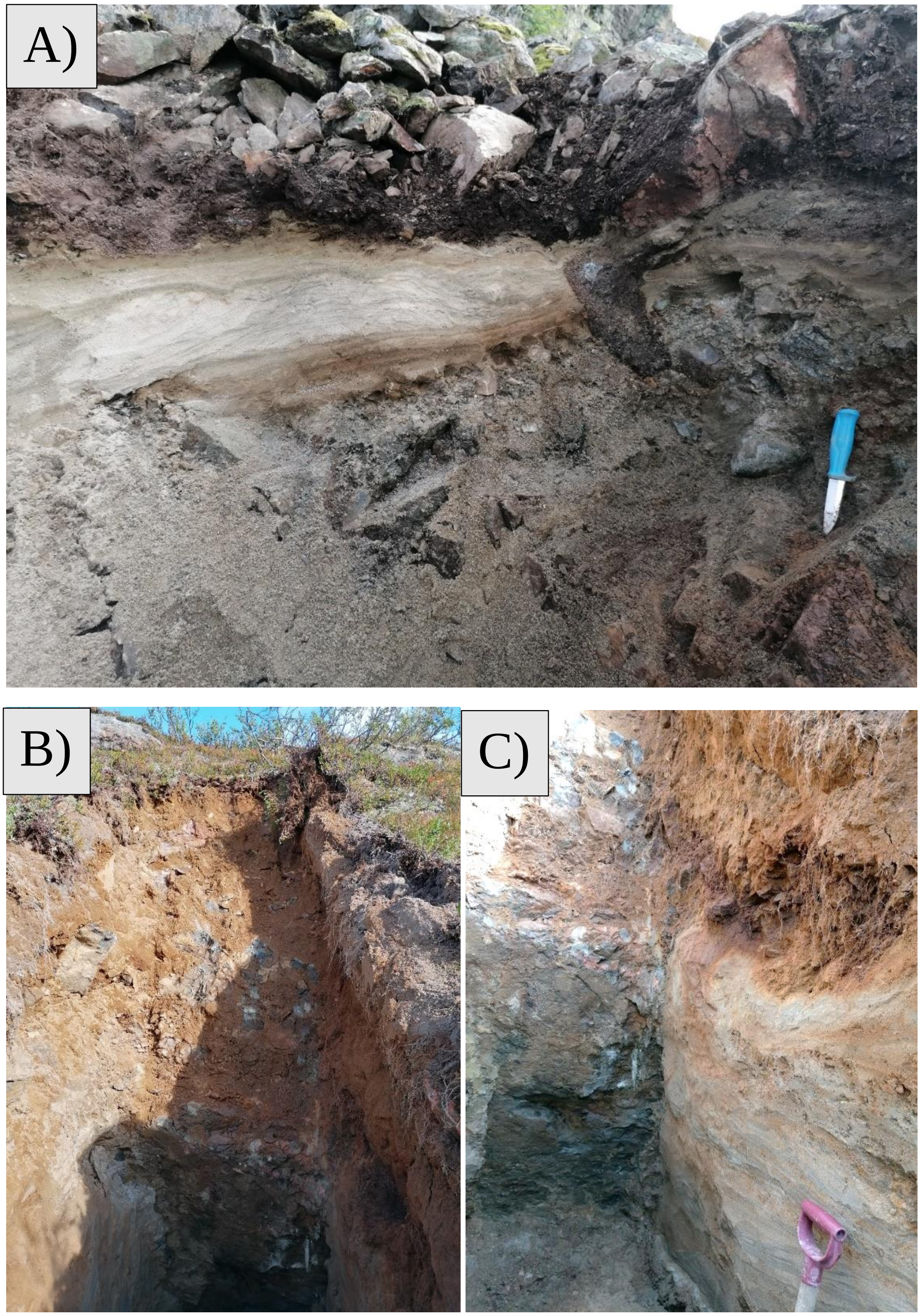

Figure 17. A) Another close-up of the deformed sediments shown in Figs.16B and 16C. B) A parallel trench, 5m from the one shown in Fig. 16B. Exposed up-thrown part of bedrock in the upper background, with thick fault breccia, overlying and interfingering with deformed glaciofluvial sediments in the central part and on both sides. C) Lower part of section shown in B. Exposed bedrock and fault plane, left in the photograph, and deformed originally layered sand underlying fault breccia to the right.

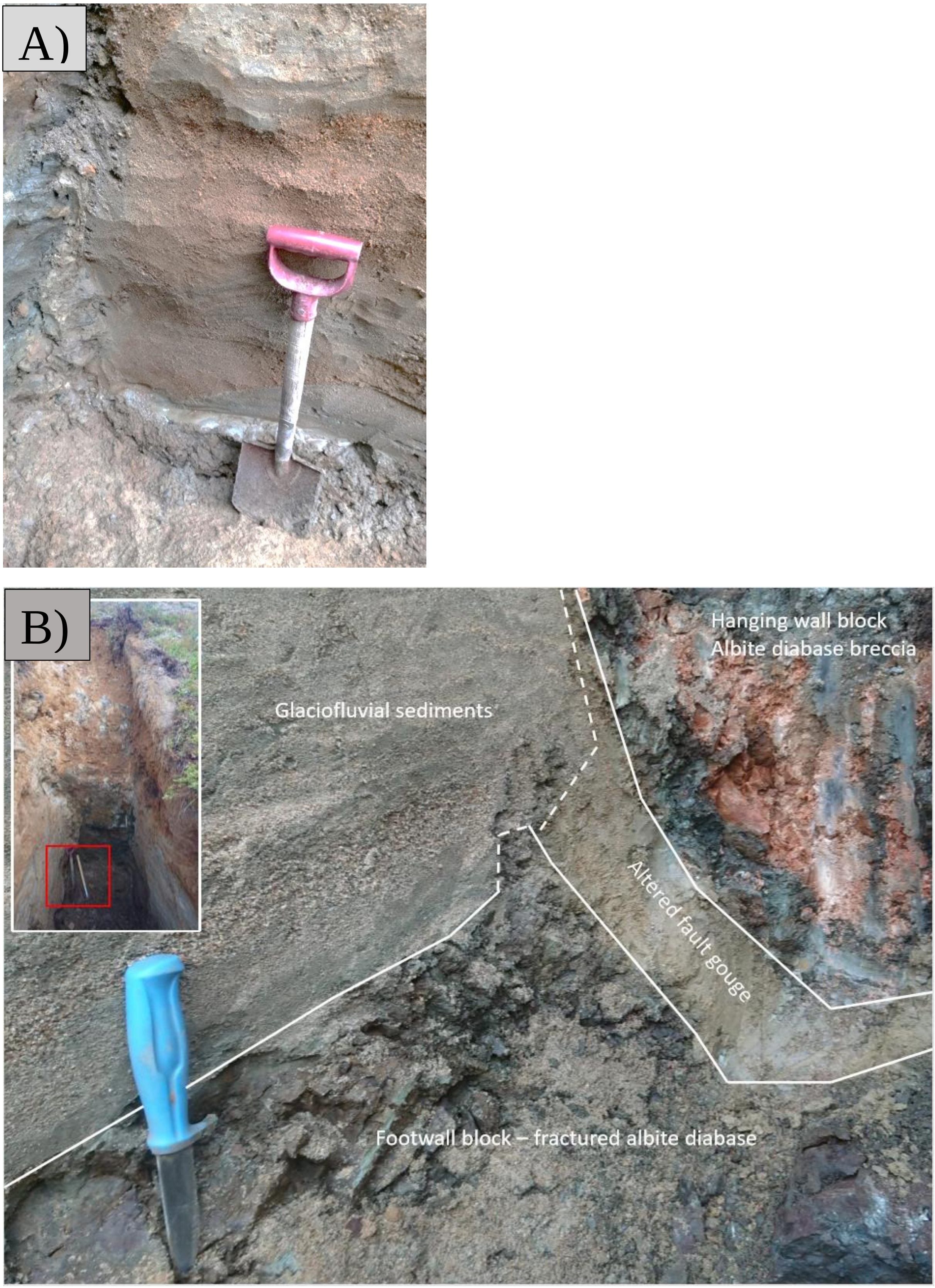

Figure 18. A) Close-up of deformed sandy sediments also shown in Fig. 17C. The deformed sand unit is surrounded with underlying and overlaying fault breccia, with thin layers of silty clay (fault gouge) in the contact zones. B) Overview and close-up of section also shown in Fig. 17B.

Spheroidal Carbonaceous Particles

During inspection of the sediment samples and search for macro-plant residues for dating, many small spheroids, approx. 0.5 mm up to 2 mm in diameter, were found in the deformed sediment units, both at Masi and at Guovziljohka (Fig. 19). Similar particles, referred to as spheroidal carbonaceous particles (SCP), are commonly formed by incomplete combustion of coal and oil (Ruppel et al., 2013), and has therefore been suggested to represent the Anthropocene (e.g., Ruppel et al., 2013; Swindles et al., 2015). The question is therefore whether the discovered particles could have been formed by natural and not just anthropogenic processes. The age of the particles is therefore crucial to clarify this, and a sample of SCPs from the deformed sand that lays above the buried peat at Masi was chosen for ^{14}C dating. The resulting age was approx. 5500 cal. years BP, which is only a few hundred years younger than the age of the dated plant macrofossils from the same stratigraphic position (Table 2, sample POZ-106547, sample 7 in Fig. 7A). This age represents the "Stone Age", i.e., long before the production of steel from bog iron ore or other industrial activities.

SCPs are recorded in all sediment samples, even in the lower peat samples at Masi (Fig. 20: "round black particles"), which indicates that they were included in the sediments before the deformation processes, i.e., a long time before the last major fault event. A natural cause for the formation of SCPs is therefore most likely, and such a process may be forest fires, which can reach temperatures of 800 to 1000˚C (Gabbert, 2011). Resin from the trees is assumed to produce similar SCPs as coal and oil, and it is suggested that the observed particles were produced by incomplete combustion of resin during forest fires. The occurrence of SCPs in all stratigraphic units indicate repeated forest fires during Holocene, and do not represent events just from the Anthropocene.

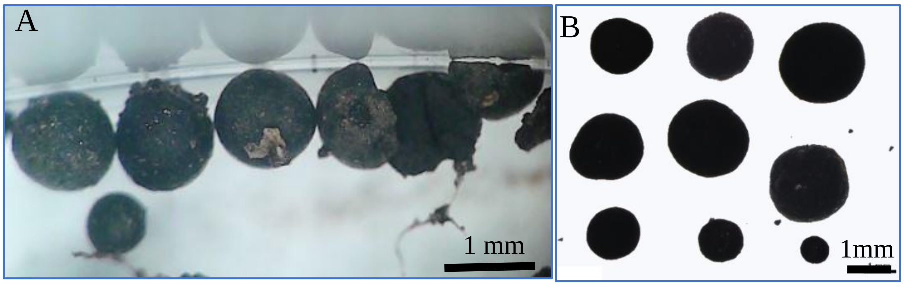

Figure 19. A) Spheroidal carbonaceous particles (SCP) from a thin organic horizon in deformed sediments overlying buried peat and deformed till in the 2019-trenching at Guovziljohka in the Iešjávri Fault System (1 in Fig.3). Size of these spheroids are c. 0.5–1.0 mm in diameter. B) Similar spheroids of larger sizes (1–2 mm diameter) from deformed sediments at Masi (Fig. 7). Such spheroids (both left and right) are from other areas known as a well-defined fraction of black carbon produced from incomplete combustion of fossil fuels, e.g., such as coal and oil (Ruppel et al. 2013). However, the spheroids in A and B are older and have most likely a natural cause (see main text for more details).

Sample number →	1-19	2-19	3-19	4-19	5-19	6-19	7-19	4B-18	3-18
Sediment depth, m →	**0.3**	**0.5**	**0.7**	**0.8**	**0.98**	**1.0**	**1.07**	**1.3**	**1.5**
Age, cal yrs BP →	**668-728**	**315-490**	**456-631**	**550-658**	**751-925**	**2350-2695**	**6275-6394**	**6314-6505**	**8429-8753**
Plant taxa identified↓									
Betula pubescens / leaf fragments	0	2	1	0	1	2	0	0	0
Betula pubescens / bark	3	4	0	0	1	3	0	2	0
Betula pubescens / wood (xylem fragments)	0	0	1	0	0	0	0	0	1
Betula total	3	6	2	0	2	5	0	2	1
Salix spp.	1	0	1	0	0	0	0	0	0
Trees and shrubs	**4**	**6**	**3**	**0**	**2**	**5**	**0**	**2**	**1**
Betula nana	0	0	0	0	1	0	2	0	0
Salix herbacea	0	1	0	0	1	0	0	0	0
Empetrum hermaphroditum	2	1	0	0	1	0	1	0	1
Cassiope tetragona	0	0	1	0	0	0	1	0	0
Vaccinium uva-ursi	0	1	1	0	0	0	0	0	0
Vaccinium myrtillus	0	0	0	1	0	0	0	0	0
Ericaceae indet.	0	0	1	0	0	0	0	0	0
Dwarf shrubs	**2**	**3**	**3**	**1**	**3**	**0**	**4**	**0**	**1**
Nardus stricta	1	0	0	0	1	0	0	0	0
Poa spp.	0	1	1	0	0	0	0	1	0
Poaceae indet.	10	4	3	0	1	0	4	0	0
Carex spp.	0	1	1	0	0	1	0	0	1
Eriophorum spp.	4	5	7	5	6	2	2	8	4
Juncus sp.	1	1	0	0	1	0	1	1	0
Luzula sp.	0	0	1	0	0	0	0	0	0
Poaceae total	11	5	4	0	2	0	4	1	0
Cyperaceae total	4	6	8	5	6	3	2	8	5
Juncaceae total	1	1	1	0	1	0	1	1	0
Graminoids	**16**	**12**	**13**	**5**	**9**	**3**	**7**	**10**	**5**
Apiaceae indet	1	0	0	0	0	1	0	0	0
Solidago spp.	0	0	1	0	0	0	0	0	0
Circaea alpina	0	0	0	0	0	0	0	1	1
Brassicaceae indet.	0	0	0	0	0	0	1	0	0
Silene acaulis	0	0	1	0	0	0	0	0	0
Caryophyllaceae indet.	0	2	0	0	0	0	0	0	0
Cerastium spp.	0	1	0	0	0	0	0	0	0
Bistorta vivipara	0	1	0	1	1	0	0	0	0
Oxyria digyna	0	1	0	0	0	1	1	0	0
Rumex spp.	1	0	1	0	1	0	0	1	0
Ranunculus cf. acris.	0	1	0	0	0	0	0	0	0
Thalictrum spp.	1	2	0	0	0	0	0	0	0
Dryas octopetala	0	0	0	0	0	0	0	0	1
Comarum palustris	0	0	0	0	0	0	0	1	0
Urtica dioica	1	0	0	0	0	0	0	0	0
Asteraceae total	1	0	1	0	0	1	0	1	1
Caryophyllaceae total	0	3	1	0	0	0	0	0	0
Polygonaceae total.	1	2	1	1	2	1	1	1	0
Ranunculaceae total	1	3	0	0	0	0	0	0	1

Rosaceae total	0	0	0	0	0	0	0	1	1
Forbs	**4**	**8**	**3**	**1**	**2**	**2**	**2**	**3**	**2**
Equisetum	120	142	150	120	145	130	150	80	60
Gymnocarpium dryopteris	0	1	0	0	0	0	0	0	0
Higher spore plants	**120**	**143**	**150**	**120**	**145**	**130**	**150**	**80**	**60**
Bryum ssp.	1	0	0	0	0	0	0	0	0
Rhizomnium pseudopunctatum	0	0	0	1	0	0	0	0	0
Dicranum scoparium	0	1	0	0	0	0	0	0	0
Distichium capillaceum	1	0	0	0	0	0	0	0	0
Calliergon richardsonii	0	1	0	0	1	0	0	0	0
Pleurozium spp.	0	0	1	0	1	1	0	0	0
Scorpidium cossonii	0	0	0	0	0	0	1	0	0
Polytrichum alpinum / P. commune	3	5	0	0	0	0	1	0	1
Sphagnum ssp.	0	0	1	0	4	8	12	5	8
Bryophyta in total	**5**	**7**	**2**	**1**	**6**	**9**	**14**	**5**	**9**
Bryophyta, poorly preserved leaves indet.	0	0	0	0	0	0	1	1	2
Round black particles	**6**	**8**	**5**	**4**	**2**	**5**	**2**	**10**	**7**
Sum of macroremains, numbers per sample	**157**	**187**	**179**	**132**	**169**	**154**	**180**	**111**	**87**
Sum of macroremains, numbers per ml.	**7,85**	**9,35**	**8,95**	**5,7391304**	**8,45**	**6,6956521**	**7,2**	**4,44**	**4,35**
Identified taxa, except Bryophyta	**12**	**18**	**15**	**4**	**12**	**7**	**9**	**8**	**7**
Identified taxa, Bryophyta	**3**	**3**	**2**	**1**	**3**	**2**	**3**	**1**	**2**
Volume of studied sediments, ml.	**20**	**20**	**20**	**23**	**20**	**23**	**25**	**25**	**20**

Table 4. Results, macrofossil analysis, samples from Trench 5, Masi (Fig. 3). Dating results are indicated as cal. years BP in 2σ uncertainty age intervals. Illustrations of recognised plant remains found in sample 2-19, 3-19, and 3-18 are included in Figs. 28 & 29 (Appendix). The dating samples are picked out from similar plant remains.

Plant macrofossils

Details of sample depths, ages and descriptions of sediments revealed during trenching across the SFC at Masi in 2018–2019 are given in Table 1. The results of the macro plant analysis of these samples are presented in Table 4 and Fig. 20. Remains that were of interest were picked out, sorted, identified, and counted. Results are presented as number of macro-remains in a volume of sediment (Table 4). To compare macrofossil data from different strata, the diagram of plant macro remains (Fig. 20) was created using the TILIA.GRAPH program (TGView 2.0.4, Grimm, 2004). The macrofossil diagram in Fig. 20 is shown as numbers in 100 cm^3 sediment.

Some of these samples may have reverse stratigraphic positions (see Tables 1, 2 & 4), because of possible turnovers from deformation during the fault events. Consequently, we have chosen not to make a traditional age-depth model of these data. Instead, we have carried out a new excavation

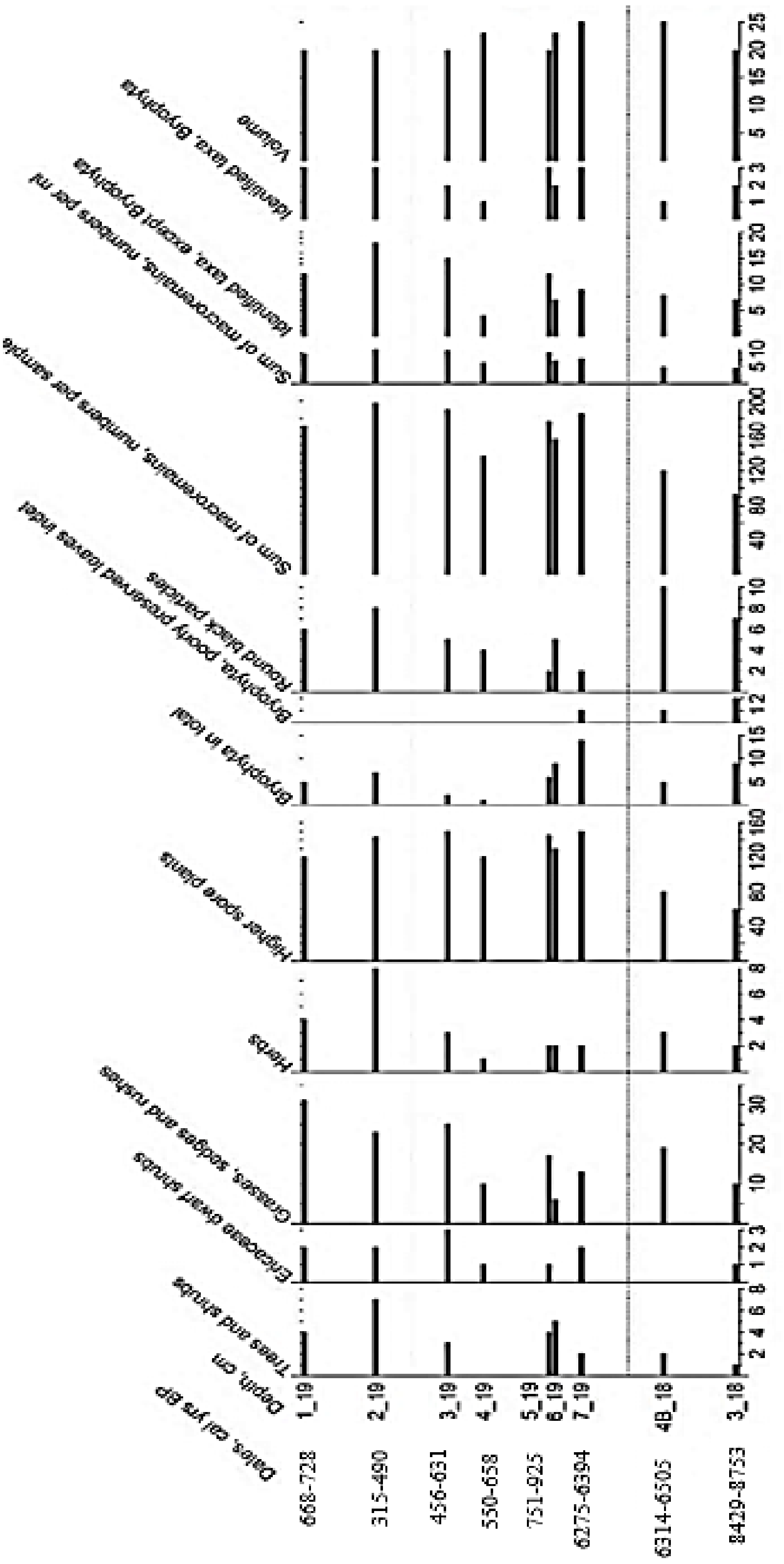

Figure 20. Groups of macro plant remains in samples from the SFC Masi trenching site 2018-2019 (Trench 5 in Fig. 3). For sample locations and descriptions, see Tables 1& 4. Sample no. 4-19, with dating result shown as 2σ uncertainty age interval (550–658 cal. years BP), is considered as the shallowest sample in the deformed sediments underlying the thin surficial peat, which is 'clearly' not affected with possible young C contamination, i.e., no traces of (vertical) modern plant root threads.

in 2021, with sampling of undisturbed sediments in a trench located just outside the reach of the fault deformation. In this way we hoped to get a continuous sequence of samples throughout most of the Holocene, thus enabling comparison of new data with the results we already have got from the disturbed sediments in the fault zone, based on both macro-plant remains and pollen (*preliminary study*).

However, it should be noted, that even the preliminary data we have from macro-plant remains in the disturbed sediments at Masi, indicate quite normal vegetational signatures for sub-arctic vegetation during the different postglacial ages, just as expected for this area.

Results from XRD and XRF analyses and K-Ar dating of fault gouge from Ellajávri

Mineral composition

The main minerals in sample #198469 are referred to as smectite and palygorskite. Additional minerals are quartz, plagioclase, chlorite, feroxyhyte, and small amounts (traces) of amphibole. The mineral composition of the samples is given in Table 5. The results of the K-Ar dating are given in Table 6.

Grain sizes	Smectite	Palygorskite	Chlorite	Quartz	Plagioclase	Feroxyhyte	Amphibole
2000 - 63 µm	36	28	6	12	10	7	1
<63 µm	40	35	5	7	5	8	<1
2-6 µm	38	46	3	3	3	7	<1
0.6-2 µm	39	45	4	2	2	8	<1
<0.6 µm	35	58	5	0	0	2	0

Table 5. Mineralogical composition of sample 2020-#198469 (Ellajávri, SSW of Masi) based on XRD. The samples also contain smectite/chlorite mixed-layered minerals, which are added to the smectite content [wt%].

Fraction	^{40}Ar* mol/g	σ ^{40}Ar* (%)	^{40}Ar* %	K wt %	σ K (% rel.)	Age (Ma)	σ (Ma)
<0.6 µm	1,725E-10	0,46	33,7	0,190	2,2	459,8	±9,1
0.6-2 µm	4,176E-10	0,35	60,4	0,411	2,2	507,4	±9,7
2-6 µm	4,317E-10	0,30	60,8	0,403	2,2	531,3	±10,0

Table 6. Results of the K-Ar dating of fine fractions of the clay-altered fault gouge from the Ellajávri trench at the south extreme of the Fitnajohka Fault System. Younger ages are obtained for the finest clay fractions. Uncertainties for ^{40}Ar and K concentrations are relative, whereas age uncertainties are absolute. ^{40}Ar* %: proportion of ^{40}Ar that is radiogenic.*

The term "fault gouge" indicates a cataclastic rock formed by crushing or grinding of the original rock in a fault zone. However, the composition of the present sample is mainly a result of hydrothermal and diagenetic processes, where new minerals have crystallised from a brine rich in Mg, Al, Si, and Fe. The presence of the two dominating minerals, smectite and palygorskite, is seen by the strong reflections (in dry conditions) at 14Å and 10.4Å, respectively. Furthermore, the identification of smectite is seen by the shift of the main reflection from 14Å to 17Å, when saturated with ethylene glycol (Fig. 21).

However, a large part of the 'smectite' is not a pure smectite, but an irregular smectite/chlorite mixed-layered mineral. This is seen from the glycolated sample scan by a broad poorly defined XRD reflection in the range 7Å to 7.7Å and after heating at 550 ^{O}C, one sees a broad, poorly defined XRD reflection from 13.5Å to 10Å (Fig. 21). The main Xray-reflections of the smectite/chlorite mixed-layered mineral are 'over-lapping' completely with the pure smectite. For this reason, the smectitic minerals are referred to as 'smectite' (Table 5). The sample also contains some chlorite, which gives a well-defined 14Å reflection after heating at 550 ^{O}C (Fig. 21).

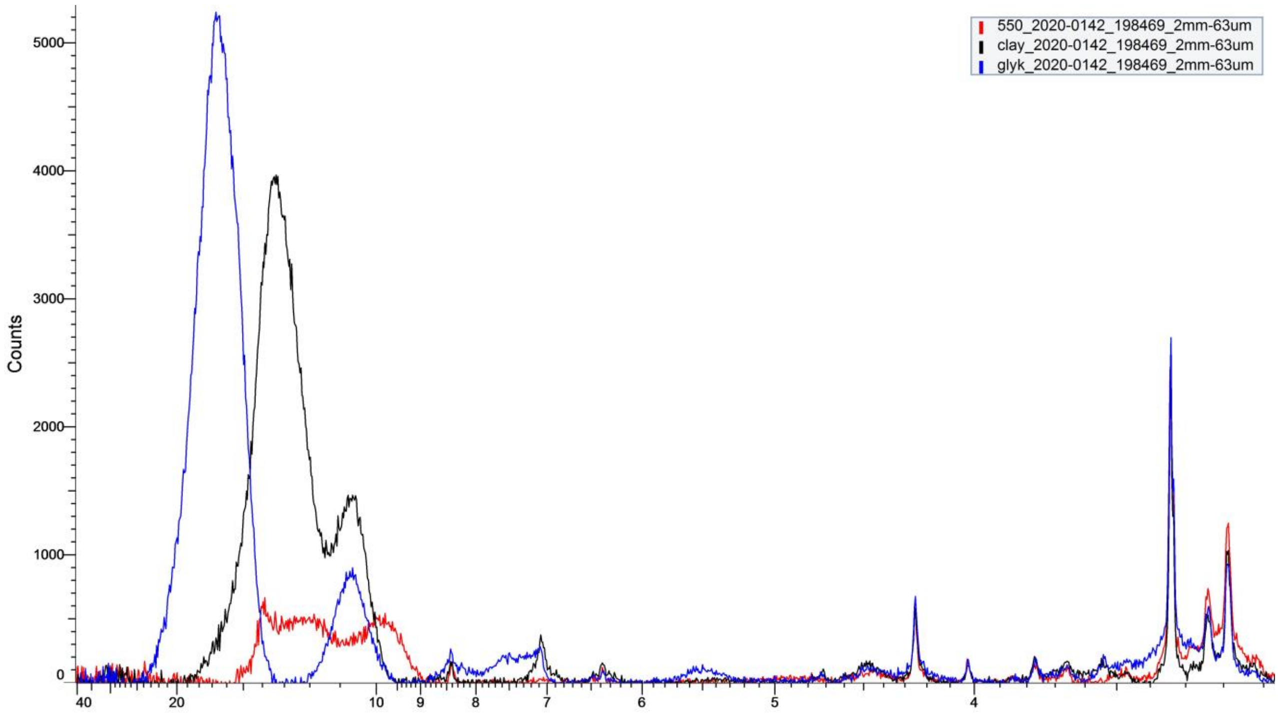

Figure 21. The X-ray diffractograms of sample <63 microns (silt + clay fractions) scanned in 1) dry condition (black), 2) glycol saturated (blue), and 3) heated at 550 degrees C (red). The red curve (after heating) shows reflections at 14Å due to the presence of chlorite, and at 12Å due to the presence of smectite/chlorite mixed-layered mineral. The blue curve is showing the expansion of smectite when saturated with ethylene glycol.

The palygorskite is also altered by the heating and the main reflection shifts from 10.4Å to ~9.5Å, seen by a broad peak from 11Å to 9Å (Fig. 21). The collapsed smectite is also included in this peak.

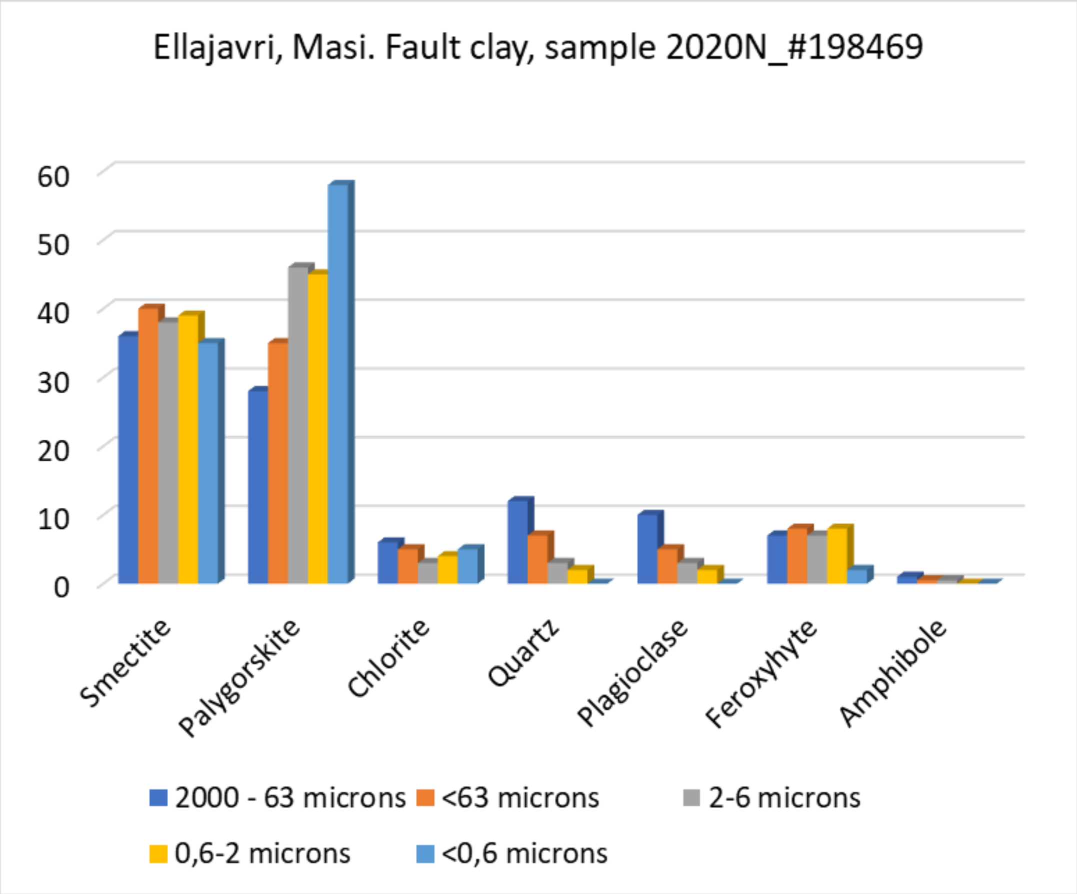

Figure 22. Illustration of mineral composition of the various particle size fractions. The two left columns illustrate the composition of the sand fraction and the silt + clay fractions, respectively. The three columns to the right illustrate the composition of the fine silt fraction (2-6 microns) and the two clay fractions (Table 5).

The mineral composition of the five sample specimens is illustrated in Fig. 22. The high contents of smectite and palygorskite in all fractions, including the sand size fraction, demonstrate that the dispersion process has not been able to disintegrate the smectite particles from the palygorskite. This is explained by the fibrous growth habit of palygorskite, making a web that locks up the smectite particles. Furthermore, it implies that the smectite particles must have crystallised *in-situ*, in the palygorskite network.

Formation of palygorskite and smectite

Palygorskite is commonly thought to be formed by diagenesis in alkaline brines rich in Mg, Al and Si, either as a replacement of smectite or by direct precipitation from the brine. Thus, smectite is commonly associated with palygorskite (Millot, 1970; Ryan et al., 2018; Chen et al., 2004). It is also reported that smectite may form from palygorskite at mild hydrothermal leaching (Mumpton & Roy, 1958; Komarneni, 1989).

In the present case, the brine was also rich in iron, which strongly indicate a reduced environment for iron to stay in solution. This excludes contact with oxygenated meteoric water, i.e., no weathering processes were associated with the formation of palygorskite.

The composition of the mineral assemblage indicates a prevailing high magnesium activity in the pore water, because the sample also contains chlorite, and much of the 'smectite' is actually a smectite/chlorite mixed-layered mineral.

The fibrous crystal growth of palygorskite often leads to a cardboard- or leather-like shape of the gouge filling in such fractures, hence the term ‘mountain leather’ for palygorskite. This mineral is found at several localities in Norway (e.g., Sæther, 1964). The occurrence of palygorskite is commonly associated with hydrothermal processes. In a study of veins filled with palygorskite and smectitic mixed-layered minerals in the nepheline syenite at Stjernøy, Northern Norway, Salter & Appleyard (1974) also suggest a hydrothermal formation of palygorskite.

Chemical analysis

The chemical composition of the fraction <63 microns (i.e., silt and clay) is given in Table 7, both main elements and some trace elements. The sample is characterised by high ignition loss due to the high contents of smectite, chlorite, and palygorskite. High iron content in the sample (12.3 weight-% Fe_2O_3) is primarily associated with the ferric mineral feroxyhyte (FeO(OH)) which indicates a late oxidation of the porewater at this location.

Main elements: Weight%	**SiO2**	**Al2O3**	**Fe2O3**	**TiO2**	**MgO**	**CaO**	**Na2O**	**K2O**	**MnO**	**P2O5**	**Ign. loss**
2020N_#198469 <63 µm fraction	51,6	12,3	12,3	0,71	9,38	2,22	0,32	0,625	0,09	0,14	9,81
Trace elements:	**Ba**	**Co**	**Cr**	**Cu**	**Ni**	**Pb**	**Sr**	**V**	**Zn**	**Zr**	**S**
(mg/kg)	164	47	504	207	111	<50	33	151	72	109	<200

Table 7. Chemical composition of the <63micron fraction of sample 2020N #198469. The chemical composition is based on XRF. The main elements are given in weight-%, while the trace elements are given in mg/kg.

Feroxyhyte is often found as coating on larger grains in poorly drained soils (Mindat.org., 2021). Otherwise, the high content of iron and magnesium in the sample is associated with the high contents of magnesium- and iron-rich minerals, such as chlorite and smectite/chlorite mixed-layered mineral.

Palygorskite may also contain iron, as demonstrated by Galan & Carretero (1999). They found that palygorskite often contained 5 to 6 weight-% Fe_2O_3. However, we do not know the iron content of the palygorskite in this case. The high contents of magnesium and iron in the sample point to a mafic source rock. Olesen et al. (1992a, b) report that the Stuoragurra Fault cuts through amphibolites and diabase within the Suoluvuobmi Formation, and that brecciation is observed at all locations where the bedrock is exposed in the fault escarpment. The presence of diabase and brecciation in the fault zone suggests abundant water-rock interactions with mafic rocks, which is crucial for the mobilization of the building materials for palygorskite, smectite and chlorite.

Neither mica nor illite is detected in the XRD scans of the samples, and this is supported by low contents of potassium. The content of K_2O (0.63 weight-% in Table 7) is probably associated with incipient illitisation of smectite and possibly some substitution of potassium for sodium in the plagioclase.

The trace elements given in Table 7 show some high values for P, Cr, Cu, V, and Ni. The samples have 5-10% iron-hydroxides and these trace elements may be adsorbed on the iron-hydroxides.

K-Ar geochronology results

K-Ar data were obtained from three grain size fractions (Table 6). The finest grain size fraction yields the youngest K-Ar date of 459.8 ± 9.1 Ma, and K-Ar dates increase with grain size. XRD data (Table 5) suggests that the only K-bearing phase in the <0.6 µm fraction is smectite, probably in the form of illite interlayers, whereas the coarser grain size fractions contain amphibole in addition to smectite.

Interpretation of K-Ar geochronology results

XRD and K-Ar data from the three dated grain size fractions (Tables 5 & 6) suggest that the finest fraction, hosting mainly smectite as a K bearing phase, is likely to record the age of incipient illite growth in the smectite, thus, giving the youngest age. The coarser fractions also contain some plagioclase, which may contain antiperthitic potassium. The old age of the plagioclase implies a high $^{40}Ar^*/K$ ratio which would affect the calculated K-Ar dates of the coarser fractions. The presence of small amounts of amphibole does not contribute significantly to potassium.

At 531 Ma (early Cambrian) the marine transgression had started from northwest towards southeast with a slope of approximately 20 m per km. The distance from the outcrop of the peneplain at Čárajávri to Ellajávri is around 30 km. The difference in elevation between Ellajávri and the Sub-Cambrian peneplain is therefore 600 meters plus the difference in altitude between the outcrop of the peneplain at Čárajávri and Ellajávri (150 m). The locality at Ellajávri was therefore located approximately 750 meters below the Sub-Cambrian peneplain during the early Cambrian. Maximum burial temperature for the autochthonous sediments is commonly set to around 200 degrees Celsius, i.e., within the constraint commonly set for diagenetic processes, while maximum burial temperature in the Lower Allochthon is set to around 250 °C. This indicate that initial metamorphism in this area took place before the movement of the Lower Allochthon. These high temperatures are not supported by the full expansion of the smectite in the clay samples from the fault. Heating of Fe-rich smectites (which we have here) to above 200 °C would cause complete dewatering and incipient dihydroxylation (Derkowski, 2017). Since the smectite shows full swelling ability, this indicates that the temperature has never been so high.

The Ordovician K-Ar age (459.8 ± 9.1 Ma) obtained from the <0.6 μm fraction of the sample might suggest an initial illitization of the smectite. However, such illitization has not been identified on the XRD scans. A regular illite/smectite mixed-layered mineral should have a reflection at 13.5 Å when saturated with ethylene glycol, but this is not seen (Fig. 21). However, minor incipient irregular growth of illite in the smectite interlayers may still be "hidden" in the broad XRD reflection of palygorskite (10Å–12Å).

The Cryogenian to Cambrian Dividal Group is downfaulted by c. 100 m to the south-east along the MSSZ (Townsend et al., 1989; Siedlecka et al., 2011). The overlying Caledonian sole thrust (Silurian Gaissa Thrust) is, however, not offset.

Landslides and rock avalanches in the fault area and in adjacent positions

From LiDAR data we have recorded c. 60 landslide scarps in or close to the area of the Stuoragurra Fault Complex (Fig. 2). We have dated landslides in one location in a relatively flat area, west of the mountain Rassegalvarri and close to the Fitnajohka Fault System (location close to Trench 8 in Fig. 3). Two landslides are recorded at this location; (Figs. 3 & 23), one older landslide that seem to have occurred before c. 9,500 cal. years BP and formed the main bowl of the slide depression, and one small younger landslide occurring after c. 3,300 cal. years BP (Table 3: nos. 41–43). Landslides in two other locations have been studied, one located 8 km SE of Masi (Fig. 24A) and the other just west of Trench 3 (Figs. 3 & 24B). In both locations, there have been major

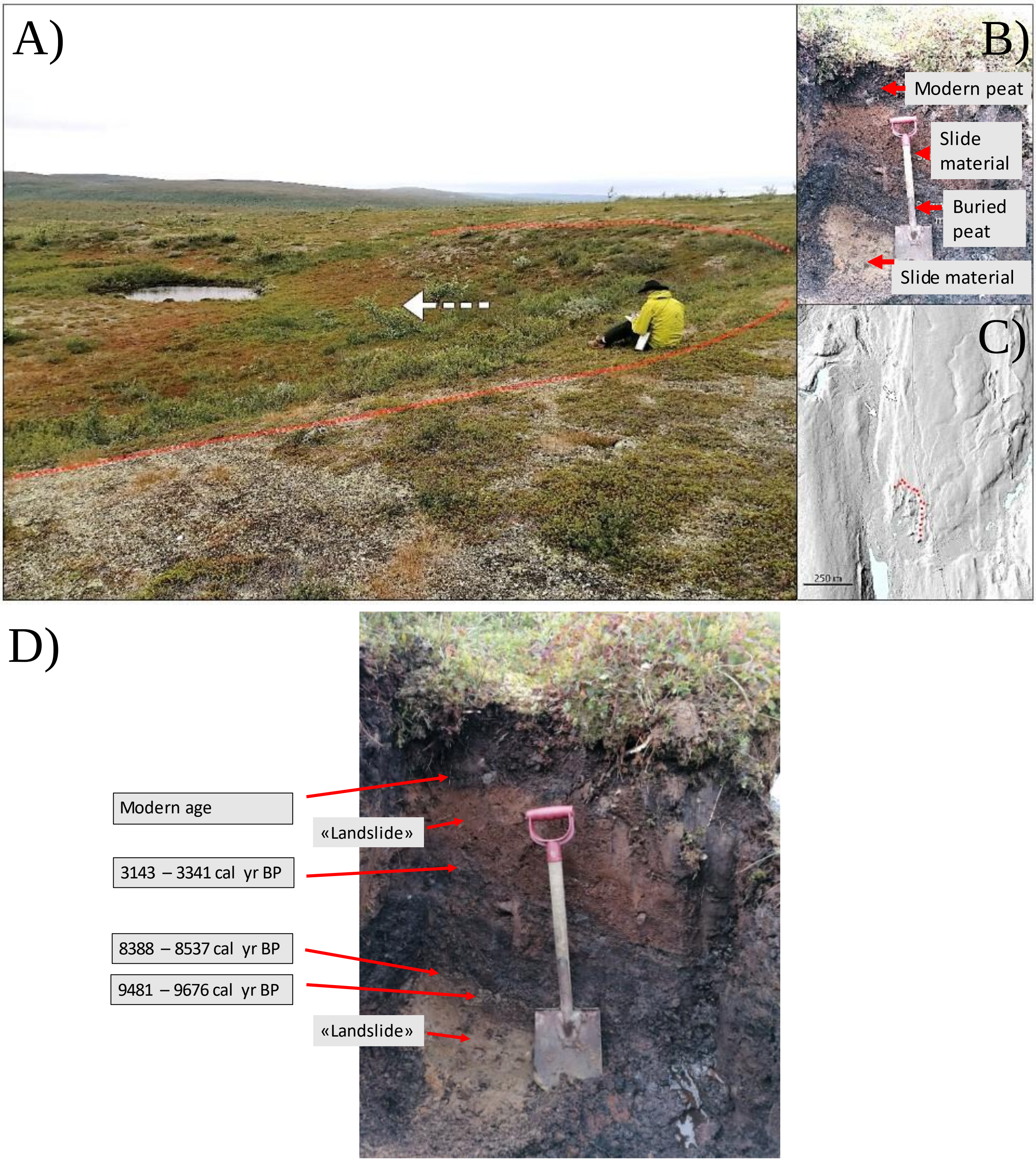

Figure 23. A) Landslide in the southernmost part of the Fitnajohka Fault System, with slide edge marked with red dot-lines. Geographical position: 69.220˚N; 23.396˚E; 472 m a.s.l.
B) Stratigraphy with peat, overlying slide materials and buried peat. C) LiDAR image of the area with landslide (red dots) and white arrows indicating two close-lying, almost parallel fault scarps. D) Close-up of stratigraphy in the landslide depression shown in A, with peat and two units of landslide diamicton separated by buried peat. The location is adjacent to the old road between Kautokeino and Alta, in the southernmost part of the Fitnajohka Fault System (close to 8 in Fig. 3). ^{14}C dates, shown in cal yr BP with 2-sigma uncertainty age range, indicate that the older landslide occurred prior to c. 9.5 cal kyr BP and the younger one after c. 3.3 cal kyr BP.

landslide episodes during or shortly after deglaciation, with slide morphology integrated fully into the deglaciation landscapes, including, e.g., kettle holes and meltwater channels. In the slide location SE of Masi a small landslide occurring within the bigger one is dated to modern timebased on ^{14}C-dating of gyttja in lacustrine silt-sand in a little pond in the slide depression (Table 3: no. 37; Fig. 24A).

In the slide location west of Trench 3 a small landslide occurred prior to 1735 cal. years BP (Table 3; no. 39), and there also located within the main bowl of the older bigger one. The latter is however more like a flush channel from the last deglaciation, a hypothesis which is supported by the presence of kettle holes on the top surface adjacent to the flush scar (Fig. 24B). ^{14}C-dating of gyttja in lacustrine sediments in a pond in the slide depression is also in this case basis for age estimation of the landslide.

A medium sized rock avalanche has been recorded to the northwest of Skoganvarre in the continuation of the fault to the NE, about 10 km from the fault (Figs. 2, 3 & 25). The rock avalanche is not dated but is assumed to be of a late Holocene age, due to the fresh appearance of the angular edges of the margins of the slip zone. Curvilinear structures in the lower parts may indicate that this portion of the rock fall material may have had enough time to transform to a rock-glacier type of formation. However, field observations this year indicate that the curvilinear structures may alternatively be a result of sliding of the avalanche on thick sandy glaciogenic deposits in the steep valley side. Two other minor rock avalanches occur along the eastern shore of lake Virdnejávri (Figs. 2 & 3). They are located c. 5 and 13 km northwest of the Máze fault system. A curvilinear c. 700 m long and c. 100 m wide unstable mountain slope is located c. 120 m above the northwestern shore of the hydropower reservoir behind the Alta Dam (Figs. 3 & 26). The distance to the Alta Dam and the SFC is 3 and 15 km, respectively. The vertical subsidence seems to be in the order of 20 m along the curvilinear fractures. Open fractures can be observed on arial photographs (www.norgeibilder.no). The water level of the water reservoir below the unstable rock slope is varying with 45 m during a year and is consequently contributing to further destabilization and to melting of the permafrost https://cryo.met.no/nb/permafrost. Present day permafrost is acting as a 'glue' to the fractured bedrock.

The unstable bedrock slope is covering an area of 120 000 m^2 along the Alta River south of the Alta Hydropower Station Dam, and north of the SFC. It reaches most likely c. 100 m downwards below the surface of the dammed Alta River. If the unstable area also reaches, e.g., 100 m into the bedrock, then it will include an unstable bedrock volume of c. 3 mill. m^3. The reservoir immediately below the unstable rock slope has a length of c. 700 m, a depth of c. 45 m and a width of c. 110 m. In total, this volume represents c. 1.75 million m^3 of water that most likely will be displaced if up to 3 million m^3 of rock falls into the reservoir. (We have assumed full magazine that will be the situation most of the year.) About half of the water will go northwards in the direction of the Alta Dam, i.e., c. 0.9 million m^3 of water (representing a body with 90 x 100 x 100 m of water). The crest of the dam is 150 m long, and it is 40 km downstream to the Alta Fjord. We recommend that a modelling of this scenario is carried out to predict the water flow in the Alta River. There is also a need to model the development of a potential tsunami across the narrow Virdnejávri and Latnetjávri lakes to the village Maze (Masi) located 30 km to the south.

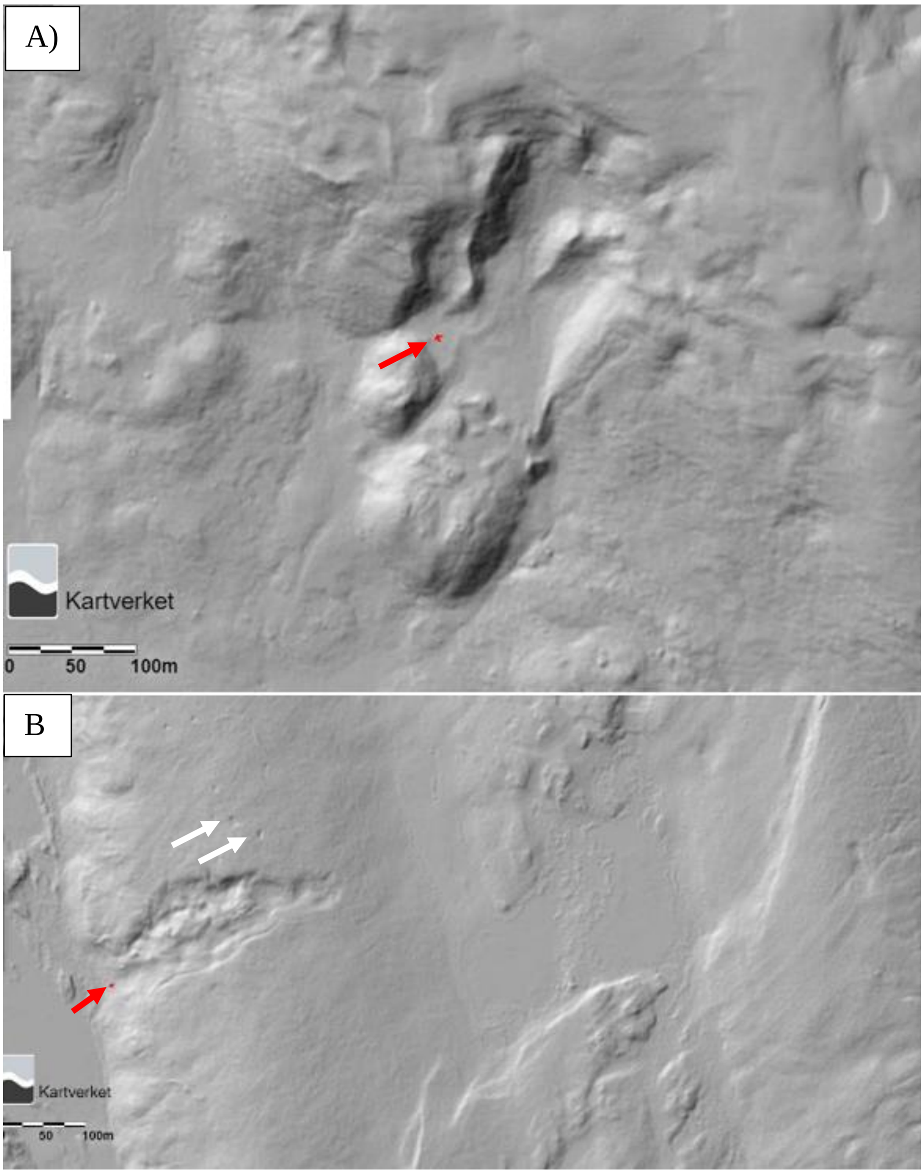

Figure 24. LIDAR images from www.høydedata.no. A) Landslide 8 km SE of Masi, and B) flush channel – landslide depression west of Trench 3 (Masi N). Geographical coordinates for the former are: 69.40597˚N, 23.80394˚E, Euref89, UTM 33, 7724473N, 44579E, and height: NN2000: 433.08 m a.s.l., DOM: 423.32 m a.s.l.. Geographical coordinates for the latter: 69.48833˚N, 23.67412˚E, Euref89, UTM 33, 7732851N, 838227E, and height: NN2000: 391.33 m a.s.l., DOM: 394.31 m a.s.l. Sampling sites for ^{14}C dating of gyttja in small ponds in the lower part of the slide depressions are indicated by arrow and a small red x in each case. Dating results are included in Table 3 (nos. 37–39). Kettle holes indicated with white arrows.

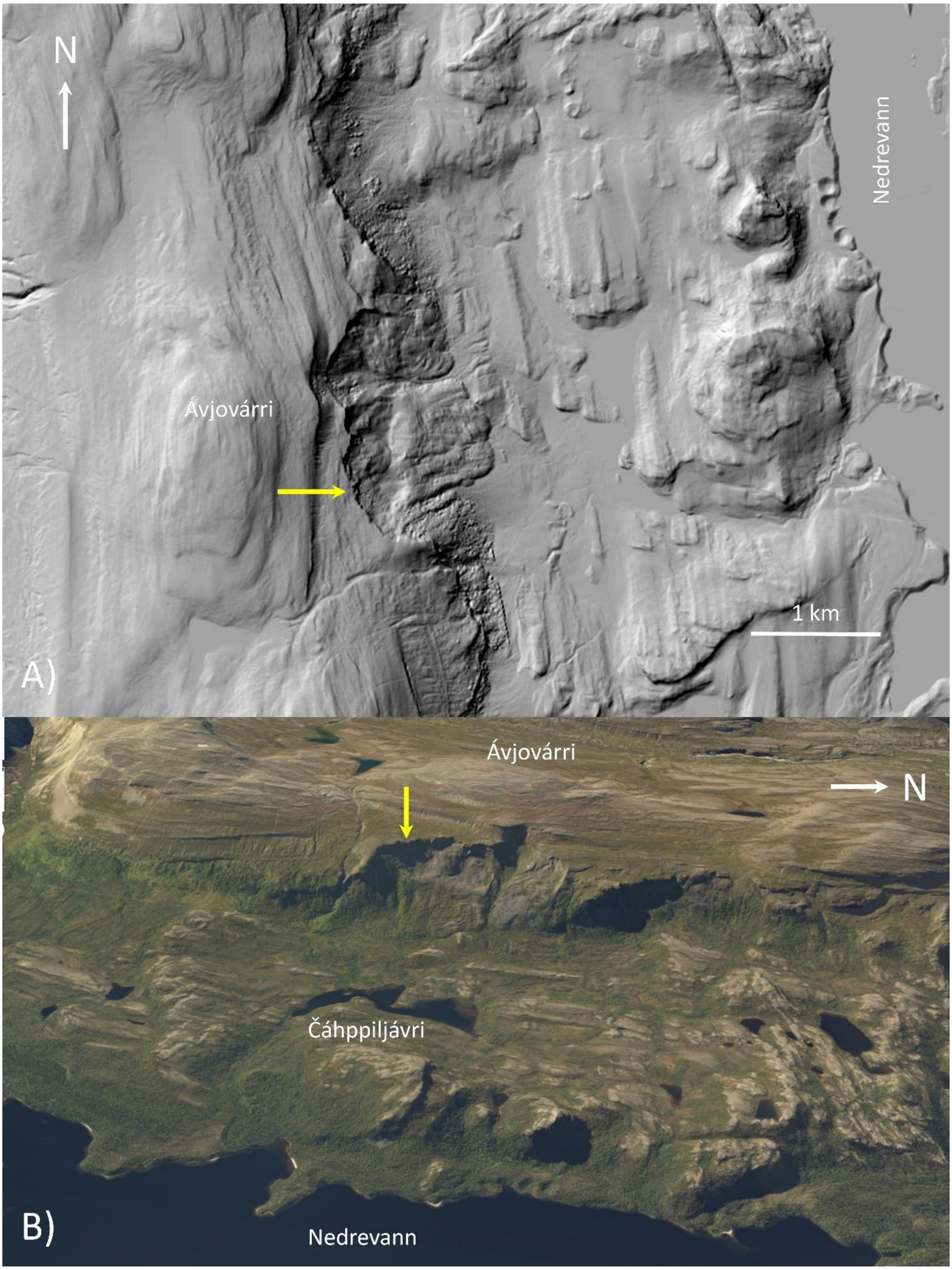

Figure 25. Rock avalanche west of Lakselv in Finnmark. Lower parts of the avalanche seem to have possibly transformed to a rock-glacier type of formation, with some lobate sliding structures present. For location, see upper right corner of Fig. 2. From www.høydedata.no and www.norgeibilder.no

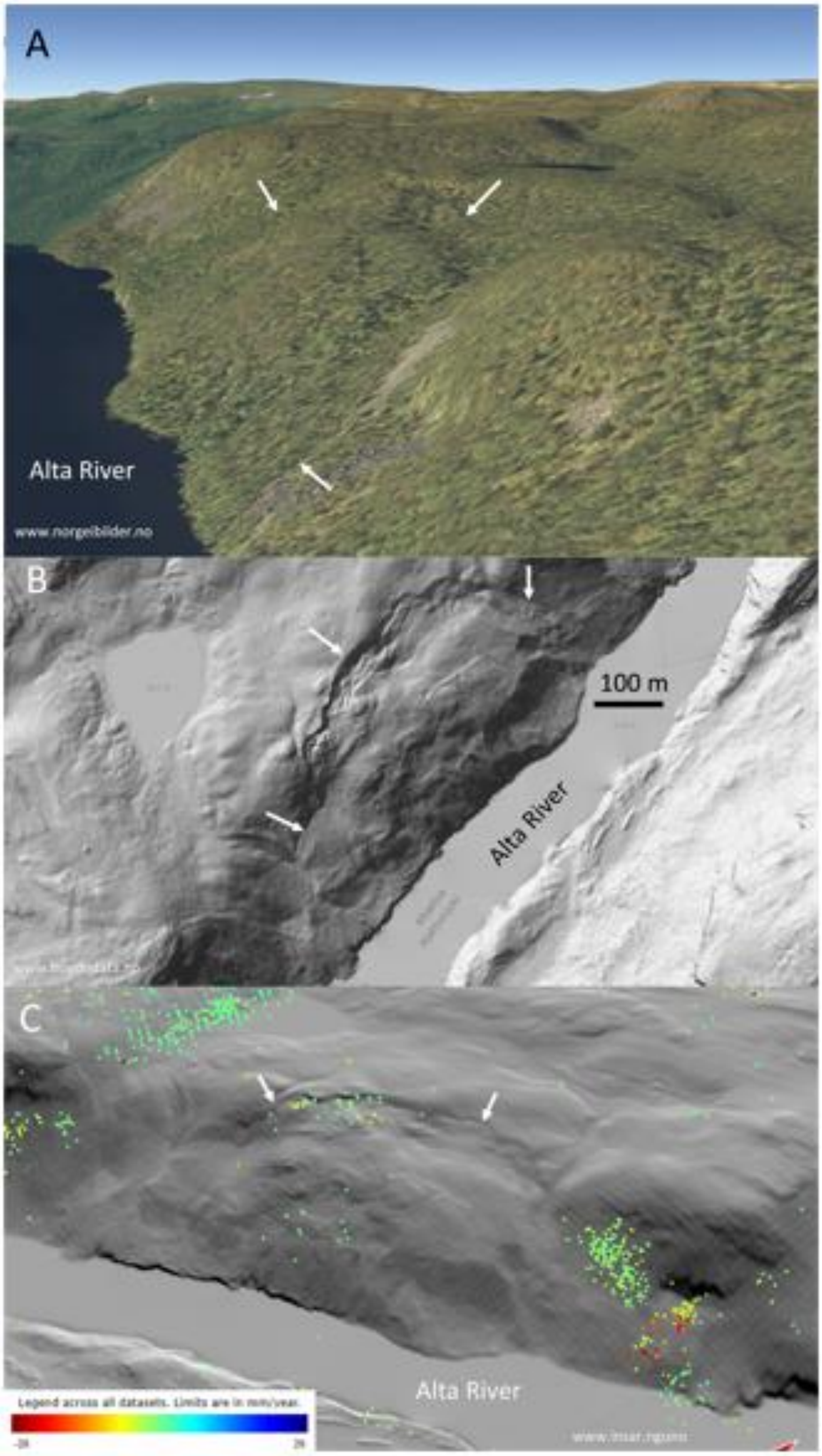

Figure 26. Unstable bedrock slope covering an area of 120 000 m^2 along the Alta River south of the Alta Hydropower Station Dam, and north of the SFC (Fig. 3). It reaches most likely c. 45 m downwards below the surface of the dammed Alta River. The height of the almost vertical wall at the back of the unstable rock slope is up to 15 m. If the unstable area reaches, e.g., 25 m into the bedrock, then it will include an unstable bedrock volume of c. 3 mill. m^3. InSAR data (C) show that the parts of the unstable rock slope is moving downwards with a speed of c. 10 mm/year (www.insar.ngu.no).

Discussion

The Stuoragurra Fault Complex (SFC) consists of three fault systems including at least 29 segments and each of the fault systems consists of 7-13 segments (Olesen et al., 2022) (Fig. 2). The three fault systems constitute the SFC and occur within the older Mierojávri-Sværholt Shear Zone (Olesen et al., 1992a). As to date it has not been clear if they formed during one large earthquake or several smaller events. Trenching across one of the southernmost segments in the Fitnajohka area in 1998 (Dehls et al., 2000) reveals one seismic event deforming the lodgement till into a large 5 m high fold above a blind thrust below the hanging wall block. When comparing the SFC with other postglacial faults in northern Fennoscandia (Lagerbäck & Sundh, 2008; Palmu et al., 2015), with emphasis on height and length of scarps and length between scarps, there is evidence for at least three separate seismic events, i.e., the Fitnajohka Fault System in the southwest, the Máze Fault System in the central area and the Iešjávri Fault System to the northeast. Fault parameters are given in Olesen et al. (2022). Some of the drainage systems in the area, especially northeast of Iešjávri, are controlled by the same weakness zones in the basement. Streams may have modified the fault escarpments following their formation (Olesen, 1988). The escarpments in the two southernmost faults have maximum scarp heights of 7 m and occur partly in an *en échelon* pattern. The distance between the Fitnajohka and Máze Fault Systems is 6 km while the distance between the Máze and the Iešjávri Fault Systems is 12 km. We assume that the Iešjávri Fault System is almost continuous at the floor of the Iešjávri lake since postglacial faults occur on either side of the lake (Fig. 2). Wesnousky (2008) suggests that earthquakes do not typically jump from one segment to another if the distance between the segments is more than 3–5 km. He based this conclusion on a total of 37 historical earthquakes with observed surface ruptures. A spacing of more than 5 km between surface ruptures therefore likely indicates that the earthquakes occurred in separate events. This would support the idea that the three fault systems along the SFC may have ruptured independently. Mattila et al. (2019) arrived at similar conclusions for the postglacial faults in northern Finland.

Radiocarbon dating of buried organics from locations along the Máze and Fitnajohka Fault Systems indicate fault events younger than c. 600 cal. years (N=5) and possibly younger than c. 1,280 cal. years BP (N=2) (Fig. 3; Trenches 5 & 7; Table 2: nos. 1-5; Table 3: nos. 30-31), respectively. Sand wedge injections in existing peat leaves no doubt about the faulting age that must be younger than the surficial peat at 20 cm depth at Masi, Trench 5, as illustrated in Fig. 7A and further described in the text. The faulting age at Fitnajohka is less well documented, as described before, and cannot be excluded as slightly older than c. 1,280 cal. years BP. Therefore, we cannot conclude with the present-day knowledge if these data represent one or two major faulting events. In addition, there is some data suggesting the occurrence of a smaller postglacial faulting event at Masi before the major one. This is exemplified by the multiple wedges of fault breccia injected in the overburden on the footwall at Trench 4 (Fig. 5C) and the damming event which led to accumulation of lacustrine sediments revealed in Trench 5 may just possibly be associated with a minor reverse fault event.

The apparently very young ages achieved from radiocarbon dating of the SFC at Masi require special attention to the reliability if these dates. It is well known that plant roots may give much too young ages of organic material in peat or minerogenic sediments at depth, this is considered and observed roots are not included in the dating samples. However, very small sticks that might be fragments of plant root systems may have been attached to other plant fragments and not detected during cleaning of samples for dating, and by that may have biased the dating results. We think that this may possibly have affected the dating results from the uppermost part of the deformed sediments, between positions 2 and 4 in Fig. 7A, where visible vertical traces of recent or former plant roots where observed. Consequently, it is needed to evaluate these ^{14}C-dates (Table 2: nos. 6–10) further before eventually included in the estimation of maximum age of the fault event. We observe that the age results of these dates overlap, or are just slightly younger than, and do not deviate significantly neither from those of close lying samples where no vertical traces of modern plant roots have been observed, nor from the dates at 20–30 cm depth in the surficial peat. In addition, most dating materials from the deformed lacustrine sediments are bark and twigs (mainly from birch; Fig. 7C) which we think are normally good ^{14}C-dating materials and not particularly susceptible for young C contamination. Considered that the lacustrine sediments were injected and pushed into the surficial peat during the faulting event, the youngest part of the lacustrine sediments should be older than the fault and younger than the overlying surficial peat at 20–30 cm depth, i.e., just above the lacustrine wedges (Figs. 7A & 8). However, based on the observations of vertical traces of recent or sub-recent plant roots we choose to exclude the dating nos. 6-10 from the data used to estimate maximum age of the youngest fault event.

We have as best we could, picked out leaves, twigs, and bark, which we consider most reliable for dating. However, even in these cases young plant remains could possibly be brought to some depth in wet peat due to, e.g., animal tramp or root turnovers, but structures of such events have not been observed, especially not in the upper 20 cm of the peat. This suggests that the sampled macro plant remains from the surficial peat are in *in situ* position and not re-deposited or contaminated from young carbon.

The peat depth and estimated accumulation rate of the undisturbed peat at the western flank of the mire adjacent to the fault scarp at Trench 5 (Fig. 10A, B), suggest an age of c. 500 years BP at 20 cm depth, which is the same peat depth as at the eastern flank of the mire where surficial peat there is found disturbed from below from sand wedges injected during the fault event. We consider this as a strong support to the idea of a very young age of the fault event at Masi, based on ^{14}C dates of recent peat at 20 cm depth at Trench 5 (Fig. 3; Table 2), and by that also is a strong support for the reliability of the young radiocarbon dates of the fault event from this site.

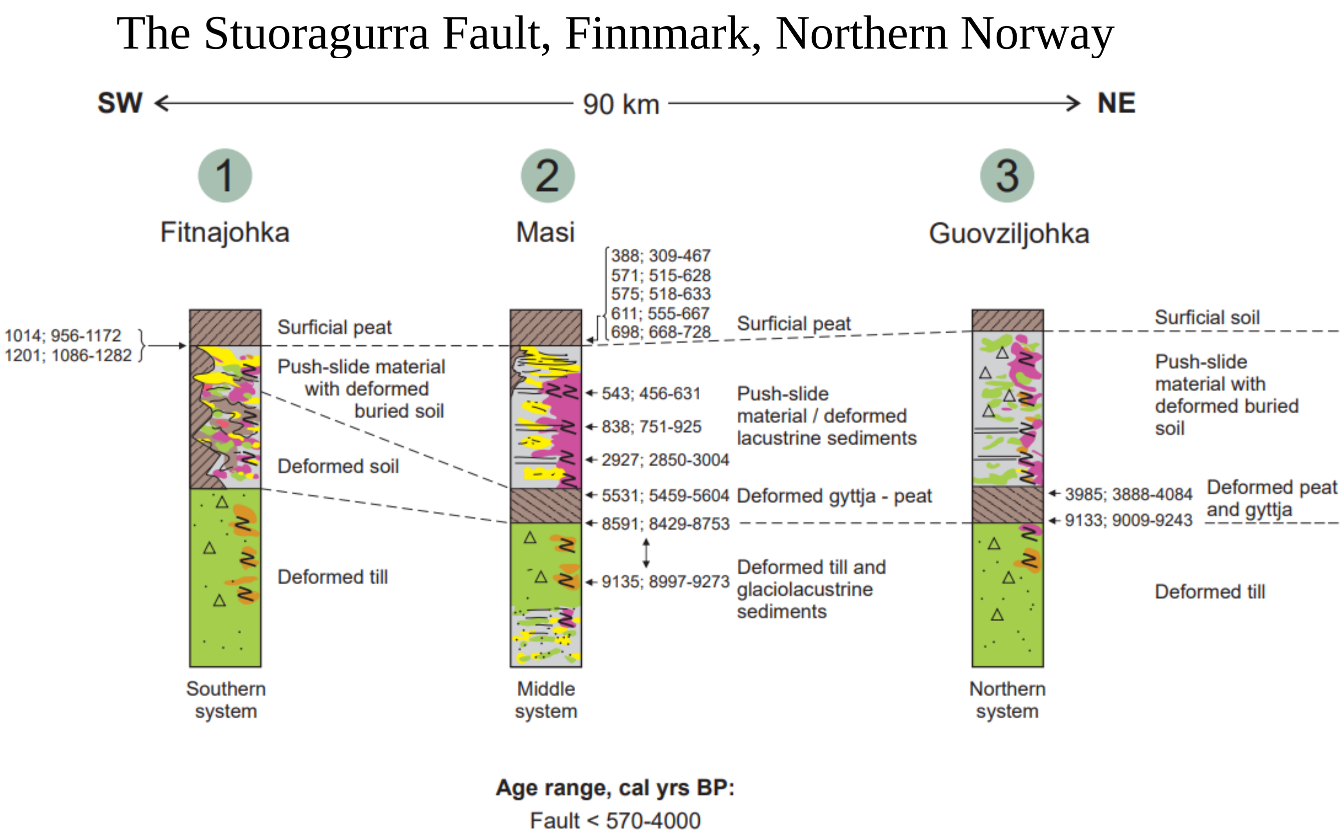

Figure 27. Combined simplified stratigraphies from footwall positions at three dating sites in the Stuoragurra Fault Complex, from Fitnajohka in the Fitnajohka Fault System, from Masi in the Máze Fault System, and from Guovziljohka in the Iešjávri Fault System. Results from ^{14}C dating calibrated to calendar years BP of the most relevant dates for age estimation of the faulting are indicated, with mean age and 2-sigma uncertainty range (for location see Fig. 3), and with more dates and details given in Tables 2 and 3. The deformed sediments at Fitmjohka and Masi are injected into existing peat (see main text), meaning that the indicated ages from positions directly upon the deformed sediments must be older than the faulting and deformation.

The nine segments of the Iešjávri Fault System occur with a spacing of 1–5 km and have a maximum scarp height of 2–3 metres. The length of the individual segments is maximum 2.5 km. Radiocarbon dating of buried organics at Guovziljohka in the Iešjávri Fault System indicate an age younger than 4,000 cal. years BP for the fault event there. At present, we are unable to decide upon how many fault events these radiocarbon dates represent, except at least one younger than 4,000 cal. years BP.

A synthesis based on a combination of simplified stratigraphies from the footwall positions at three dating sites in the Stuoragurra Fault Complex is presented in Fig. 27. Our working hypothesis is now, based on all available data, that the youngest fault event may have occurred at different ages in the three separated fault systems of the SFC. At Guovziljohka the sediments deformed during faulting seem to have just simply buried parts of the surficial postglacial peat which existed at that time. At the other sites, particularly at Masi, the situation was more complex, with both burying of parts of the postglacial peat, and injections into it. We do not know precisely how much of the surficial peat overlying the sandy injections closest to surface in the western end of Trench 5 (Masi) which have accumulated after the faulting event. However, it is clearly less than 20 cm (Figs. 7A & 8), and the surficial 20 cm of the peat represents less than 10% of the total c. 2.0-2.5 m thick Holocene peat, recorded just outside the western end of Trench 5. These uppermost 20 cm thus represents just a few hundred years of accumulation, and, therefore, supports the dating results from this depth level.

Large earthquakes in mid-continents such as Australia, Eastern United States, North China, and North-western Europe show complex spatiotemporal patterns that do not fit existing seismotectonic models (Clark et al., 2012; Calais et al., 2016; Liu and Stein, 2016). Individual faults tend to fall into long term (thousands of years or longer) dormancy after a cluster of ruptures, whereas large earthquakes seem to roam between widespread faults. This model can also be applied to the postglacial faults within the Lapland fault province. The end-glacial faults in the Bay of Bothnia area (e.g., the Lansjärv, Röjnoret and Burträsk faults, Lagerbäck & Sundh, 2008) could have transferred stress to neighbouring faults and disturbed conditions on distant faults in Finnmark and Finnish Lapland (Olesen et al., 2022). This model can explain the much younger age of the SFC and the northernmost postglacial faults in Finland (Ojala et al., 2019) compared with the Gulf of Bothnia faults in Sweden. It is also compatible with the GIA modelling by Steffen et al. (2014a, b) who predicted faulting along a 45° dipping weakness zone in a prestressed region beneath the centre of the former ice sheet. In such a system, widespread mid-continental faults can accommodate slow tectonic loading from the far field (including ridge push). Calais et al. (2016) and Craig et al. (2016) argue that the lithosphere can store elastic strain over long timescales, the release of which may be triggered by rapid, local, and transient stress changes caused by erosion, fluid migration or ice loading, resulting in the intermittent occurrence of intraplate seismicity. Liu & Stein (2016) and Calais et al. (2016) conclude that this paradigm shift would make some commonly used concepts such as recurrence intervals and characteristic earthquakes inadequate in many mid-continental areas. This has significant bearings on the seismic hazard estimates for Fennoscandia and implies that large earthquakes in the order of magnitude 7 can occur today (Olesen et al., 2022).

We speculate that some of the c. 80 earthquakes registered along the postglacial faults in the SFC between 1991 and 2019 (Olesen et al., 2022) may possibly represent aftershocks of a large-magnitude earthquake that occurred less than 500–600 years ago. Aftershock sequences can according to seismological observations and models (Stein & Liu, 2009) last for centuries in intraplate regions.

The deformed sediments associated with the fault system, contain a lot of small (0.5 to 2 mm diameter) spherical carbonaceous particles (SCPs), both at Masi and Guovziljohka. These particles are like black carbonaceous particles produced by incomplete combustion of fossil organic material, like coal and oil (Ruppel et al., 2013). For this reason, it has been suggested that such SCPs were derived from industrial activity and therefore have a young age, representing the beginning of the Anthropocene (e.g., Ruppel et al., 2013; Swindles et al., 2015). However, ^{14}C-dating of a SCP sample from Masi gave an age of 5,500 cal. years BP. Consequently, it is suggested that these particles have a natural source, like e.g., forest fires, and therefore, the occurrences of SCP in the deformed sediments cannot be used to suggest a maximum age of the SF fault at Masi.

The apparently different ages of the three main fault systems in Finnmark (Fig, 27) is supported by empirical data from historical surface ruptures reported from other faults where distances more than 3–5 km between fault segments often indicate different rupture ages of each fault system (e.g., Wesnousky, 2008). Different periods of postglacial faulting are also evident from age dating of landslides in northern Finland (e.g., Ojala et al., 2018). Radiocarbon age data revealed three episodes of increased landslide formation associated with postglacial faulting, from 9,000 to 11,000 cal. years BP, from 5,000 to 7,000 cal. years BP and from 1,000 to 3,000 cal. years BP.

Units of diamicton with breccia structure (normal fault breccia) adjacent to the fault scarp are produced and injected as wedges into the overburden during the faulting events. This was first observed during trenching at Fitnajohka in 1998 (Dehls et al., 2000) and is typically found in several of the trenching sites since Masi 2018 (Trench 5; Fig. 3). Breccia constitutes a major part of the present unconsolidated overburden. This is recorded in all trenches excavated down to the bedrock, i.e., hanging wall-footwall boundary in the fault scarp area.

Fault clay from the Mierojávri–Sværholt shear zone in the Ellajávri area, SSW for Masi, consists mainly of palygorskite and smectite. It is suggested that these minerals were formed by prolonged hydrothermal and diagenetic processes during Cambrian and Ordovician. This is confirmed by K-Ar dating of the fine fractions (<6 microns) of the material, which gives ages from 531.3 ± 10.0 Ma to 459.8 ± 9.1 Ma (youngest age of the finest clay fraction). The mineral forming processes in this shear zone are suggested to be the result of precipitations from hydrothermal brines rich in Mg, Al, Si and Fe. The good swelling properties of smectite show that the formation and subsequent storage has taken place at temperatures well below 200 °C. The high content of poor crystalline iron oxyhydroxide (feroxyhyte) in the sample indicates an incomplete oxidation of iron, because feroxyhyte tend to recrystallise to goethite when exposed to atmospheric conditions. It is therefore suggested that these iron compounds were formed in a reduced environment, simultaneously with the formation of palygorskite and smectite. This precludes weathering processes with oxidized meteoric water. Consequently, these data do not give reason to suggest an age of the old fault activity in the fault zone. The best data to suggest an age of the older fault activity here is the occurrence of weathered fault gouge, with e.g., kaolinite and vermiculite, at Fitnajohka (Åm, 1994) and lithified fault breccia at all trenched sites where bedrock was reached (7 of 8 sites; the trenching at Guovziljohka, Trench 1 in Fig, 3, did not reach bedrock). These data imply that the young SFC faulting is just reactivation of an old fault zone.

Several landslides in the proximity of faults in northern Finland have been found to have occurred over most of the Holocene, with the youngest landslides occurring 3,000–1,000 cal. years BP (Ojala et al., 2018). We have so far tried to estimate the age of three of the c. 60 recorded landslides less than 20 km from the SFC (Fig. 3), and in all three cases a large landslide forming the main part of the slide depression occurred during the last deglaciation or shortly after that. In all three cases there are also younger, smaller slides represented. It is needed more data to see if clusters of landslide events occur in any age-intervals during the Holocene. Therefore, it is at present premature to discuss further whether any of these slides may have been induced by earthquakes and seismicity along or close to the SFC.

'Black swans' are often applied as a metaphor for extreme and rare events which might still happen. In the risk discipline, this term is used to emphasise how serious and inconceivable instances are still possible. We think that large earthquakes represent threats or "black swans" to Norwegian society and especially to the Norwegian hydropower and oil and gas industry.

Our studies also provide important information for ongoing exploration programs offshore northern Norway by estimating the impact of recent uplift and neotectonics that is applicable for understanding subsurface conditions, such as temperature, stress, gas expansion and sealing of reservoirs.

Further studies are needed to investigate the areas outside the faulting disturbed area (seismic, paleo-seismic, geodesy), to assess potential hazards of large earthquakes in the future and reduce their possible effects. We need to understand the potential for large earthquakes in Finnmark, to mitigate the effects of such events.

Conclusions

- The Stuorgaurra Fault Complex (SFC) comprises 29 segments which can be grouped into three major systems with c. 6–7 and 12 km wide gaps without any apparent faulting. They were most likely formed during three or more separate earthquakes.
- The dip of the reverse postglacial faults as observed in trenches is 50–55° implying a maximum reverse displacement of approximately 9 m, which together with the 14–21 km length of the fault systems indicates associated earthquakes with a moment magnitude of 6.4–8.0 if just one fault rupture event happened in each fault system. If more than one fault rupture event occurred in each fault system, which we have discussed the possibility of for the Máze Fault System at Trenches 4 and 5, then the associated earthquakes would be less than magnitude 7.
- Trenching across different sections of the faults, including radiocarbon dating of organic material buried in the deformed sediments, reveals a late Holocene age (younger than c. 600, c. 1,280 and c. 4,000 cal. years before present at three separate fault systems, respectively). This indicates that faulting occurred as much as c. 10,000 years after deglaciation, and is not a direct result of rapid, initial, rebound following deglaciation.
- Units of diamicton with breccia structure (normal fault breccia) adjacent to the fault scarp is produced and injected as wedges into the overburden during the faulting events and the breccia constitutes a major part of the present unconsolidated overburden. This is recorded in all trenches excavated down to the bedrock, i.e., hanging wall-footwall boundary in the fault scarp area.
- Fault clay from the Mierojávri-Særholt Shear Zone in the Ellajávri area, SSW for Masi, consists mainly of palygorskite and smectite. It is suggested that these minerals were formed by prolonged hydrothermal and diagenetic processes during Cambrian and Ordovician.
- Lithified fault breccia is observed in all trenches reaching bedrock, i.e., in 7 of 8 trenches. This indicates that the young SFC faulting represents reactivation of an old fault zone.
- Palynological data from macro-plant remains from the buried organic matter at Masi (Máze) reveal a pre-fault vegetation history typical for the early to late Holocene in this area.

- The deformed sediments at both Masi and Guoziljohka, contain abundant small spherical carbonaceous particles (SCP) (commonly 0.5–2.0 mm in diameter). Dating of these particles with ^{14}C gives an age of 5,500 cal. years BP. It is therefore suggested that the observed SCPs are the result of natural processes, such as forest fires. Similar particles are described in the literature as well-defined fractions of black carbonaceous material produced by incomplete combustion of fossil fuels (coal and oil), distributed by emissions from combustion engines and industrial activity. However, our data show a pre-industrial origin of these particles, and the occurrence of such particles cannot be used to estimate maximum age of the SFC faulting events.
- Based on aerial photographs and LIDAR data a total of 60 landslides have been identified in relatively flat terrain. They occur mostly in the southern part and within 20 km from the fault scarps. Landslides in three locations have been dated, with a major episode during or shortly after deglaciation represented at all three sites and small landslides occurring c. 3,300 - 1735 cal. years BP in two sites, and even a smaller landslide in modern time at one of the sites. In addition, one medium size and two minor size rock avalanches of supposed late postglacial age are recorded c. 5–13 km from the fault complex.
- A curvilinear c. 700 m long and c. 100 m wide unstable mountain slope occurs along the northwestern shore of the Alta River and c. 3 km from the Alta hydropower dam and c. 15 km from the SFC.
- A georadar profile across the fault scarp in the Masi area, where also trenching was carried out, show reflectors on both sides, just below the fault scarp, before and after a blank area with no reflectors. This is interpreted as a clear indication of the displacement that took place, and which is confirmed from the trenching in the same location (e.g., Trench 4; Fig. 3), but the overall data have too little resolution to indicate details other than thickness of overburden and bedrock surface displacement.
- The SFC represents a reactivation of the regional Mierojávri-Særholt Shear Zone that was active in the Palaeoproterozoic as well as the Palaeozoic.

Acknowledgements

Klemet Johansen Hætta, Nils Erik Eriksen, Nils Peder Eira, Joar Førster, Svein Are Eira, Joar Henning Hætta, Isak Mathis Hætta and Per William Hermansen, as well as the companies Kauto Maskin, Eira Anlegg and Nord Transport (Lakselv) were responsible for the trenching in the field seasons of 2018–2021. The Geological Survey of Norway (GSN) funded the study via the projects 378100 ("Glacially Triggered Faulting"; Steffen et al., 2022) and 362200 ("Crustal onshore – offshore Project – Phase 3 (Coop 3)"). Radiocarbon datings were performed by the Poznan

Radiocarbon Dating Laboratory, Poland, and by Beta Analytic, USA. Irene Lundquist drafted the figures. Marco Brønner and Lilja Run Bjarnadottir gave useful comments to the final report draft. We express our gratitude to these persons, companies, dating laboratories and to GSN.

References

Åm, M. 1994: *Mineralogisk og petrologisk karakterisering av vitrings/sleppemateriale fra Stuoragurraforkastningen, Finnmark.* MSc thesis, Norwegian University of Science and Technology, 102 pp.

Andresen A., Agyei-Dwarko, N. Y., Kristoffersen, M. & Hanken, N.M. 2014: A Timanian foreland basin setting for the late Neoproterozoic-early Paleozoic cover sequence (Dividal Group) of northeastern Baltica. *In* Corfu, F., Gasser, D., and Chew, D. M., (eds.): *New perspectives on the Caledonides of Scandinavia and related areas.* Geological Society Special Publications 390, 157–175.

Bakken, A.J.H. 1983: *Nordmannvikdalen kvartærgeologi og geomorfologi.* MSc thesis, University of Oslo, 126 pp.

Bingen, B., Solli, A., Viola, G., Torgersen, E., Sandstad, J.S., Whitehouse, M.J., Rohr, T.S., Ganerød, M. & Nasuti, A. 2015: Geochronology of the Palaeoproterozoic Kautokeino Greenstone Belt, Finnmark, Norway: Tectonic implications in a Fennoscandia context. *Norwegian Journal of Geology*, 95, 365–396, http://dx.doi.org/10.17850/njg95-3-09.

Bjørlykke, A., Rueslåtten, H., van der Lelij, R., & Schönenberger, J. in prep.: Ediacaran to early Cambrian weathering of the Kautokeino Greenstone Belt in Finnmark, Northern Norway

Bronk Ramsey, C. 2009: Bayesian analysis of radiocarbon dates. *Radiocarbon* 51(1): 337–360.

Bungum, H. & Lindholm, C. 1997: Seismo- and neotectonics in Finnmark, Kola Peninsula and the southern Barents Sea. Part 2: Seismological analysis and seismotectonics. *Tectonophysics*, 270, 15–28.

Bungum, H. & Olesen, O. 2005: The 31st of August 1819 Lurøy earthquake revisited. *Norwegian Journal of Geology*, 85, 245-252.

Calais, E., Camelbeeck, T., Stein, S., Liu, M. & Craig, T.J. 2016: A new paradigm for large earthquakes in stable continental plate interiors. *Geophysical Research Letters*, 43, 10,621–10,637, http://doi:10.1002/2016GL070815.

Charbit, S., Guillou, H. & Turpin, L. 1998: Cross calibration of K–Ar standard minerals

using an unspiked Ar measurement technique. *Chemical Geology*, Volume 150, Issues 1–2, 147–159. ISSN 0009-2541, https://doi.org/10.1016/S0009-2541(98)00049-7.

Chen, T., Xu, H., Lu, A. et al. 2004: Direct evidence of transformation from smectite to

palygorskite: TEM investigation. *Sci. China Ser. D-Earth Sci.* 47, 985–994 (2004), https://doi.org/10.1360/03yd0509.

Clark, D., McPherson, A. & Van Dissen, R. 2012: Long-term behaviour of Australian stable continental region (SCR) faults. *Tectonophysics*, 566, 1–30.

Clauer, N. & Chaudhuri, S. 1995: *Clays in Crustal Environments, Isotope Dating and Tracing.* Springer Verlag, Heidelberg, 359 pp.

Craig, T.J., Calais, E., Fleitout, L., Bollinger, L. & Scotti, O. 2016: Evidence for the release of long-term tectonic strain stored in continental interiors through intraplate earthquakes, *Geophysical Research Letters*, 43, 6826–6836, http://doi:10.1002/2016GL069359.

Dehls, J., Olesen, O., Olsen, L. & Blikra, L.H. 2000: Neotectonic faulting in northern Norway; the Stuoragurra and Nordmannvikdalen postglacial faults. *Quaternary Science Reviews*, 19, 1445–1460.

Derkowski, A. 2017: Tightly bound water in smectites. *American Mineralogist*, 102 (5), 1073-1090. https://doi.org/10.2138/am-2017-5918

Fuhrmann, U., Lippolt, H. & Hess, J.C. 1987: HD-B1 Biotite reference material for K-Ar chronometry. *Chemical Geology*, 66, 41–51.

Gabbert, B. 2011: At what temperature does a forest fire burn?

https://wildfiretoday.com/2011/02/26/at-what-temperature-does-a-forest-fire-burn/

Galan, E. & Carretero, I. 1999: A new approach to compositional limits for sepiolite and palygorskite. *Clays and Clay Minerals*, 47, 4, 399–409.

Grimm, E.C. 2004: Tilia and TG View Version 2.0.2. Illinois State Museum, Research and Collector Center.

Hałas, S. & Wójtowicz, A. 2014: "Propagation of error formulas for K/Ar dating method".

Geochronometria, 41,3, 202–206, https://doi.org/10.2478/s13386-013-0162-1.

Henderson, I.H.C., Viola, G. & Nasuti, A. 2015: A new tectonic model for the Kautokeino Greenstone Belt, northern Norway, based on highresolution airborne magnetic data and field structural analysis and implications for mineral potential. *Norwegian Journal of Geology*, 95, 339–363, http://dx.doi.org/10.17850/njg95-3-05.

Jol, H.M. 2009: *Ground Penetrating Radar Theory and Applications*. Elsevier Science, 544 pp.

Komarneni, S. 1989: Mechanisms of Palygorskite and Sepiolite Alteration as Deduced from Solid-State ^{27}Al and ^{29}Si Nuclear Magnetic Resonance Spectroscopy. *Clays and Clay Miner.* 37, 469–473 (1989), https://doi.org/10.1346/CCMN.1989.0370512.

Lagerbäck, R. & Sundh, M. 2008: Early Holocene faulting and paleoseismicity in northern Sweden. *Sver. Geol. Unders.*, C836, 80 pp.

Lee, J.-Y., Marti, K., Severinghaus, J.P., Kawamura, K., Yoo, H.-S., Lee, J.B. & Kim, J.S. 2006: A redetermination of the isotopic abundances of atmospheric Ar. *Geochimica et Cosmochimica Acta*, 70, 4507–4512.

Liu, M. & Stein, S. 2016: Mid-continental earthquakes: Spatiotemporal occurrences, causes, and hazards. *Earth-Science Reviews*, 162, 364–386, http://dx.doi.org/10.1016/j.earscirev.2016.09.016.

Lund, B., Schmidt, P. & Hieronymus, C. 2009: Stress evolution and fault instability during the Weichselian glacial cycle. *Swedish Nuclear Fuel and Waste Management Co., Stockholm. Technical Report*, TR-09-15, 106 pp.

Lundqvist, J. & Lagerbäck, R. 1976: The Pärve fault: A lateglacial fault in the Precambrian of Swedish Lapland. *Geologiska Föreningens i Stockholm Förhandingar*, 98, 45-51.

Mattila, J., Ojala, A.E.K., Ruskeeniemi, T., Palmu, J.-P., Aaltonen, I., Käpyaho, A., Lindberg, A. & Sutinen, R. 2019: Evidence of multiple slip events on postglacial faults in northern Fennoscandia. *Quaternary Science Reviews*, 215, 242–252, https://doi.org/10.1016/j.quascirev.2019.05.022.

Mauquoy, D., Hughes, P. & Geel, B. 2010: A protocol for plant macrofossil analysis of peat deposits. *European Journal of Dental Education* - EUR J DENT EDUC. 7, 1–5.

seNorge.no 2016: Klima. http://www.senorge.no/?p=klima (accessed 24 January 2020).

McDougall, I. &Wellman, P. 2011: Calibration of GA1550 biotite standard for K/Ar and 40Ar/39Ar dating. *Chemical Geology*, 280 (1–2), 19–25.

Mikko, H., Smith, C., Lund, B., Ask, M.V. & Munier, R. 2015: LiDAR-derived inventory of post-glacial fault scarps in Sweden. *Geol. Fören. Stockh. Förh.*, 137, 334–338.

Millot, G. 1970: *Geology of Clays.* Textbook, Springer Verlag.

Mindat.org. 2021: Feroxyhyte: Mineral information, data and localities. The Hudson Institute of Mineralogy dba Mindat.org.

Mitchell, J.G. 1972: Potassium-argon ages from the Cheviot Hills, Northern England. *Geol. Mag.*, I09, 421-426.

Moss, E.S. & Ross, Z.E. 2011: Probabilistic fault displacement hazard analysis for reverse faults. *Bull. Seismol. Soc. Am.*, 101, 1542–1553.

Muir Wood, R. 1989: Extraordinary deglaciation reverse faulting in northern Fennoscandia. *In* Gregersen, S. & Basham, P.W. (eds.): *Earthquakes at NorthAtlantic passive margins: neotectonics and postglacial rebound*. Kluwer Academic Publishers, Dordrecht, The Netherlands, 141–173.

Mumpton, F. A. & Roy, R. 1956: New data on sepiolite and attapulgite in Clays & ClayMinerals, Proc. 5th Natl. Conf., Urbana, Illinois, 1955, Ada Swineford, ed., Natl. Acad. Sci. Natl. Res. Counc. Publ. 566, 136–143.

O'Hanlon, J.F. 2005: *A user's guide to vacuum technology.* John Wiley & Sons 516 pp.

Ojala, A.E.K., Markovaara-Koivisto, M., Middleton, M., Ruskeeniemi, T., Mattila, J. & Sutinen, R. 2018: Dating of paleolandslides in western Finnish Lapland. Earth Surf. Process. Landforms. DOI: 10.1002/esp.4408.

Ojala, A.E.K., Mattila, J., Ruskeeniemi, T., Palmu, J.-P., Lindberg, A., Hänninen, P. & Sutinen, R. 2017: Postglacial seismic activity along the Isovaarae-Riikonkumpu fault complex. *Glob. Planet. Chang.*, 157, 59–72.

Ojala, A.E.K., Mattila, J., Hämäläinen, J. & Sutinen, R. 2019: Lake sediment evidence of paleoseismicity: Timing and spatial occurrence of late- and postglacial earthquakes in Finland. *Tectonophysics*, 771, https://doi.org/10.1016/j.tecto.2019.228227.

Olesen, O. 1988: The Stuoragurra Fault, evidence of neotectonics in the Precambrian of Finnmark, northern Norway. *Norsk Geologisk Tidsskrift*, 68, 107–118.

Olesen, O. & Sandstad, J. 1993: Interpretation of the Proterozoic Kautokeino Greenstone Belt, Finnmark, Norway from combined geophysical and geological data. *Geological Survey of Norway Bulletin*, 425, 43–64.

Olesen, O., Henkel, H., Lile, O.B., Mauring, E. & Rønning, J.S. 1992a: Geophysical investigations of the Stuoragurra postglacial fault, Finnmark, northern Norway. *Journal of Applied Geophysics*, 29, 95–118.

Olesen, O., Henkel, H., Lile, O.B., Mauring, E., Ronning, J.S. & Torsvik, T.H. 1992b: Neotectonics in the Precambrian of Finnmark, northern Norway. *Norsk Geologisk Tidsskrift,* 72, 301–306.

Olesen, O., Blikra, L.H., Braathen, A., Dehls, J.F., Olsen, L., Rise, L., Roberts, D., Riis, F., Faleide, J.I. & Anda, E. 2004: Neotectonic deformation in Norway and its implications: a review. *Norwegian Journal of Geology,* 84, 3–34. ISSN 029-196X.

Olesen, O., Brönner, M., Ebbing, J., Gellein, J., Gernigon, L., Koziel, J., Lauritsen, T., Myklebust, R., Pascal, C., Sand, M., Solheim, D. & Usov, S. 2010: New aeromagnetic and gravity compilations from Norway and adjacent areas – methods and applications. *In* B.A. Vining, S.C. Pickering (eds.): *Petroleum Geology: From mature basins to new frontiers.* Proceedings of the 7th Petroleum Geology Conference. Petroleum Geology Conference series 7, Geological Society of London, 559–586.

Olesen, O., Bungum, H., Lindholm, C., Olsen, L., Pascal, C. & Roberts, D. 2013: Neotectonics, seismicity and contemporary stress field in Norway – mechanisms and implications. *In* L. Olsen, O. Fredin, O. Olesen (eds.): *Quaternary Geology of Norway*. Geological Survey of Norway Special Publication, 13, 145–174.

Olesen, O., Olsen, L., Gibbons, S., Ruud, B.O., Høgaas, F., Johansen, T.A. & Kværna, T. 2022: Postglacial faulting in Norway - Large magnitude earthquakes of late Holocene age. *In* H. Steffen, O. Olesen, and R. Sutinen, (eds.): *Glacially Triggered Faulting*. Cambridge University Press, 198-217.

Olsen, L., Reite, A., Riiber, K. & Sørensen, E. 1996: Finnmark fylke, kvartærgeologisk kart i målestokk 1:500 000, med beskrivelse. Summary in English. Norges geologiske undersøkelse.

Olsen, L., Olesen, O., Dehls, J. & Tassis, G. 2018: Late–/postglacial age and tectonic origin of the Nordmannvikdalen Fault, northern Norway. *Norwegian Journal of Geology,* 98, 483–500, https://dx.doi.org/10.17850/njg98-3-09.

Olsen, L., Olesen, O. & Høgaas, F. 2020: Dating of the Stuoragurra Fault at Finnmarksvidda, northern Norway. 34th Nordic Geological Winter Meeting January 8th-10th 2020, Oslo, Norway.

In H.A. Nakrem, A.M. Husås (eds.): *Abstracts and Proceedings of the Geological Society of Norway*, 1, 2020, 157–158.

Olsen, L., Olesen, O., Høgaas, F. & Tassis, G. 2021: A part of the Stuoragurra postglacial fault complex, at Máze in N-Norway, is less than 600 yrs old. Vinterkonferansen 2021, Digital, January 6th–8th, 2020. *In* H.A. Nakrem and A.M. Husås (eds.): *Abstracts and Proceedings of the Geological Society of Norway*, 1, 2021, p 55.

Palmu, J.-P., Ojala, A.E.K., Ruskeeniemi, T., Sutinen, R. & Mattila, J. 2015: LiDAR DEM detection and classification of postglacial faults and seismically-induced landforms in Finland: a paleoseismic database. *Geol. Fören. Stockh. Förh.*, 137, 344–352.

Reimer, P., Austin, W. E. N , Bard, E., Bayliss, A., Blackwell, P. G., Bronk Ramsay, C., Butzin, M., Cheng, H., Edwards, R. L., Friedrich, M., Grootes, P. M., Guilderson, T. P., Haijdas. I., Heaton, T. J., Bogg, A. G., Hughen, K. A., Kromer, B., Manning, S. W., Muscheler, R., Palmer, J. G., Pearson, C., van der Plicht, J., Reimer, R. W., Richards, D. A., Scott, E. M., Southon, J. R., Turney, C. S. M., Wacker, L., Adolphi, F., Būntgen, U., Capano, M., Fahrni, S., Fogtmann-Schulz, A., Friedrich, R., Kòhler, P., Kudak, S., Miyake, F., Olsen,. J., Reinig, F., Sakamoto, M., Sookdeo, A. & Talamo, S. 2020: The IntCal20 Northern Hemisphere radiocarbon age calibration curve (0–55 cal kBP). *Radiocarbon,* 62 (4), pp. 725–757. Published online by Cambridge University Press, doi: 10.1017/RDC.2020.41.

Roberts, D., Olesen, O. & Karpuz, M. R. 1997: Seismo- and neotectonics in Finnmark, Kola Peninsula and the southern Barents Sea; Part 1, Geological and neotectonic framework. *Tectonophysics*, 270, 1–13.

Ruppel, M., Lund, M.T., Grythe, H., Rose, N.L., Weckström, J. & Korhola, A. 2013: Comparison of Spheroidal Carbonaceous Particle Data with Modelled Atmospheric Black Carbon Concentration and Deposition and Air Mass Sources in Northern Europe, 1850–2010. Hindawi Publishing Corporation. *Advances in Meteorology*, 2013, ID 393926, 15 pp.; http://dx.doi.org/10.1155/2013/393926.

Ryan, B.H., Kaczmarek, S.E., Rivers, J.M., 2018: Dolomite dissolution: An alternative diagenetic pathway for the formation of palygorskite clay. *Sedimentology*, https://doi.org/10.1111/sed.12559.

Salter, D. L. & Appleyard, E. C. 1974: An occurrence of vein palygorskite from the nepheline syenite at Lillebugt, Stjernøy, northern Norway. *Norsk Geologisk Tidsskrift 54,* 329-336.

Sandmeier Geophysical Research 2019: REFLEXW Version 9.5, Windows™ XP/7/8/10-program for the processing of seismic, acoustic or electromagnetic, reflection, refraction and transmission data, 709 pp.; https://www.sandmeier-geo.de/Download/reflexw_manual_a4.pdf.

Schumacher, E. 1975: Herstellung von >99,9997% 38Argon für die 40K-40Ar *Geochronologie Chimia*, 29, 441–442.

Sensors and Software 2018: EKKO_Project: Processing Module Users Guide,

Sensors & Software Inc., Mississauga, Ontario - Canada.

Siedlecka, A. & Roberts, D. 1996: Finnmark Fylke. Berggrunnsgeologi M 1:500 000. Norges geologiske undersøkelse, Trondheim.

Siedlecka, A., Davidsen, B., Rice, A.H.N. & Townsend, C. 2011: Berggrunnskart; Skoganvarri 2034 IV, M 1:50 000, revidert foreløpig utgave. Norges geologiske undersøkelse, Trondheim.

Sletten, K., Olsen, L. & Blikra, L.H. 2000: Slides in low-gradient areas of Finnmarksvidda. *In* Dehls, J. & Olesen, O. (eds.): *Neotectonics in Norway, Annual Technical Report 1999.* NGU Report 2000.001, 41–42.

Smith, C., Sundh, M. & Mikko, H. 2014: Surficial geologic evidence for early Holocene faulting and seismicity. *Int. J. Earth Sci.,* 103, 1711–1724.

Smith, C.A., Grigull, S. & Mikko, H. 2018: Geomorphic evidence for multiple surface ruptures of the Merasjärvi "postglacial fault", northern Sweden. *Geol. Fören. Stockh. Förh.,* 140, https://doi.org/10.1080/11035897.2018.1492963.

Steffen, R., Steffen, H., Wu, P. & Eaton, D.W. 2014a: Stress and fault parameters affecting fault slip magnitude and activation time during a glacial cycle. *Tectonics,* 33, http://doi:10.1002/2013TC003450.

Steffen, R., Wu, P., Steffen, H. & Eaton, D.W. 2014b: On the implementation of faults in finite-element glacial isostatic adjustment models. *Computers & Geosciences*, 62, 150–159, http://doi:10.1016/j.cageo.2013.06.012.

Steffen, H., Olesen, O. & Sutinen, R. (eds.) 2022: Glacially Triggered Faulting. Cambridge University Press, 438 pp. DOI: 10.1017/9781108779906.

Stein, S. & Liu, M. 2009: Long aftershock sequences within continents and implications for earthquake hazard assessment. *Nature,* 462, 87–89.

Steiger, R. H. & Jäger, E., 1977. Subcommission on geochronology: convention on the

use of decay constants in geo- and cosmochronology. *Earth and Planetary Science*

Letters, 36, 359–362.

Sutinen, R., Hyvönen, E., Middleton, M. & Ruskeeniemi, T. 2014: Airborne LiDAR detection of postglacial faults and Pulju moraine in Palojärvi, Finnish Lapland. *Glob. Planet. Chang.,* 115, 24–32.

Sæther, E. 1964: Clay veins in rocks in Norway. *Norsk Geologisk Tidsskrift,* 44, 385-429.

Swindles, G.T., Watson, E., Turner, T.E., Galloway, J.M., Hadlari, T., Wheeler, J. & Bacon, K.L. 2015: Spheroidal carbonaceeous particles are a defining stratigraphic marker for the Anthropocene. *Scientific Reports,* 5, 10264, http://doi:10.1038/srep10264.

Tolgensbakk, J. & Sollid, J.L. 1988: *Kåfjord, kvartærgeologi og geomorfologi 1:50.000, 1634 II.* Geografisk Institutt, Univ. of Oslo.

Townsend, C., Rice, A.H.N. & Mackay, A. 1989: The structure and stratigraphy of the southwestern portion of the Gaissa Thrust Belt and the adjacent Kalak Nappe Complex, N Norway. *In* R.A. Gayer (Ed.): *The Caledonide Geology of Scandinavia.* Graham and Trotman, London, 111–126.

Virtanen, R., Oksanen, L. & Oksanen, T. 2016: Where do the treeless tundra areas of northern highlands fit in the global biome system: Toward an ecologically natural subdivision of the tundra biome. *Ecology and Evolution,* 6 (1), 143–158.

Weaver, C.A. 1980: Use of K-Ar dating and oxygen isotopes for determining the thermal history of shales. *National Technical Information Service Technical Report,* ONWI-107, 57 pp.

Wells, D.L. & Coppersmith, K.J. 1994: Empirical relationships among magnitude, rupture length, rupture area, and surface displacement. *Bulletin of the Seismological Society of America*, 84, 974–1002.

Wesnousky, S.G. 2008: Displacement and geometrical characteristics of earthquake surface ruptures: issues and implications for seismic-hazard analysis and the process of earthquake rupture. *Bull. Seismol. Soc. Am.,* 98, 1609–1632.

Wu, P., Johnston, P. & Lambeck, K. 1999: Postglacial rebound and fault instability in Fennoscandia. *Geophys. J. Int.,* 139, 657–670.

Appendix

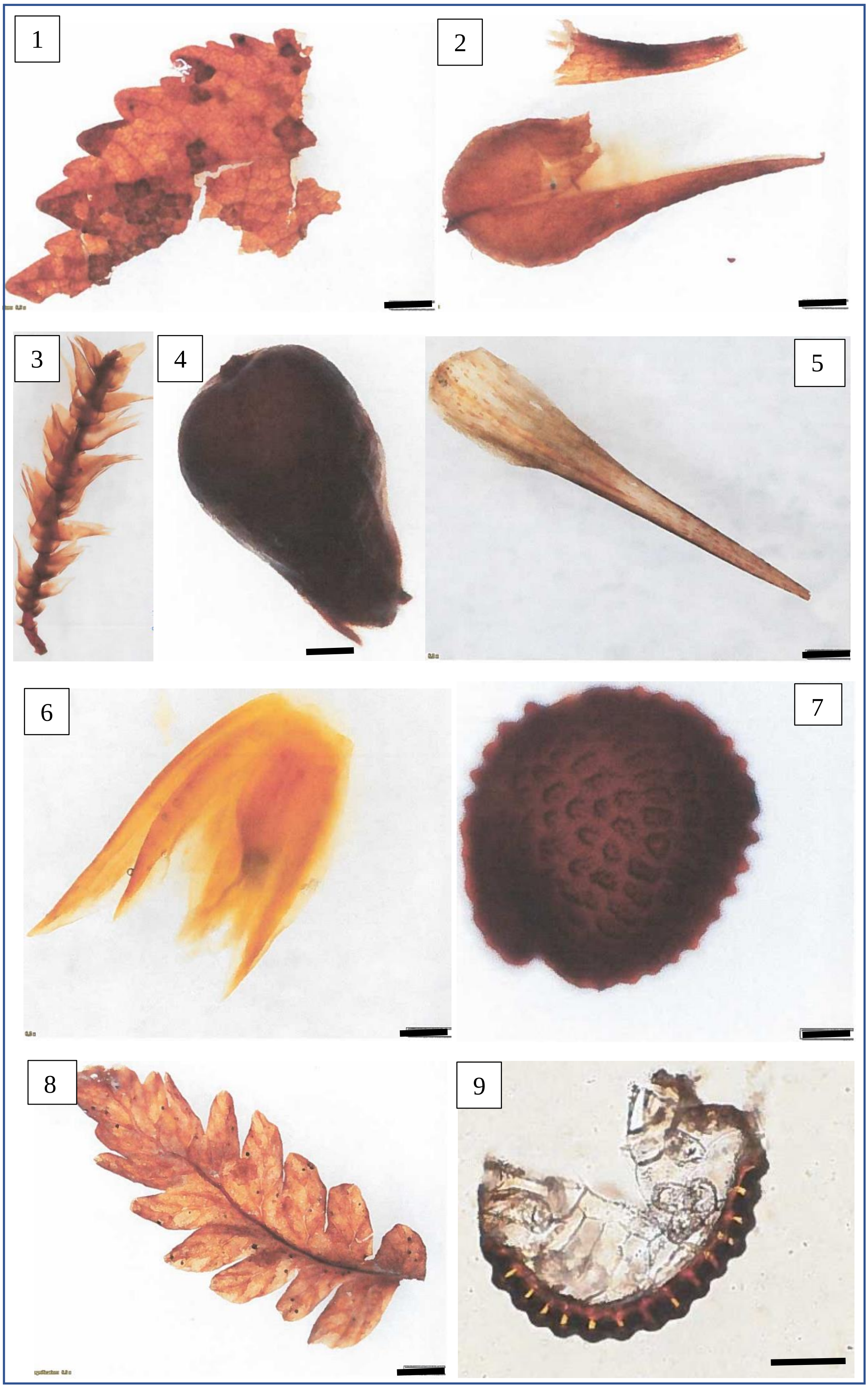

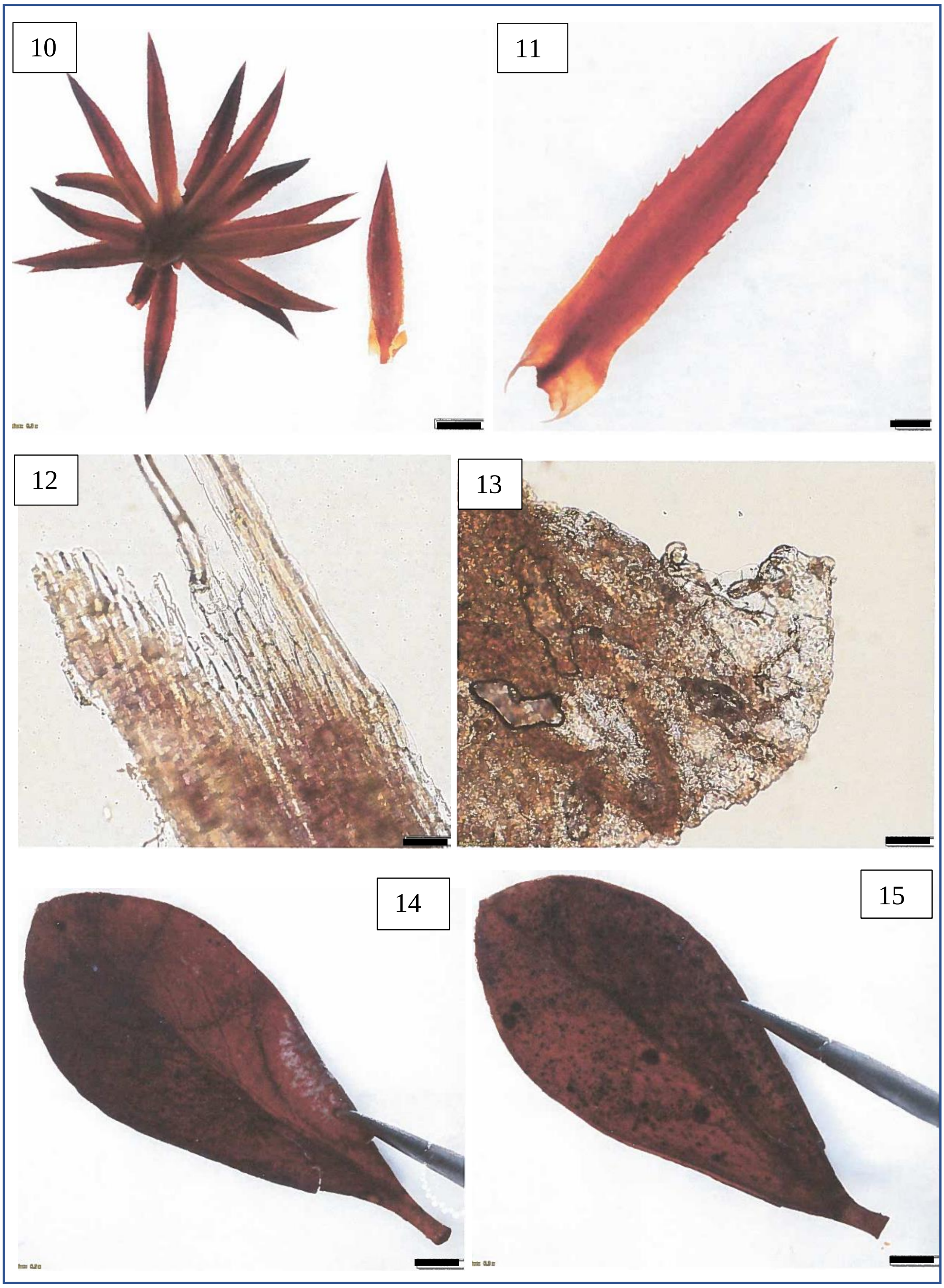

Figure 28. Plant remains from sample no. 2-19, Masi. Black rod for scale is 1 mm long. Picture 1 – Leaf of betula. 2 – Salix, 3 – Calliergon ricchardsonii, 4 – Bistorta vivipara, 5 – Carex spp., 6 – Caryophyllaceae indet., 7 – Cerastium spp., 8 – Gymnocarpum, 9 – Gymnocarpum, 10 – Politrichum, 11 – Politrichum, 12 –Ranunculus cf acris, 13 – Thalictrum spp, 14 – Vaccinium uva-ursi, 15 – Vaccinium uva-ursi.

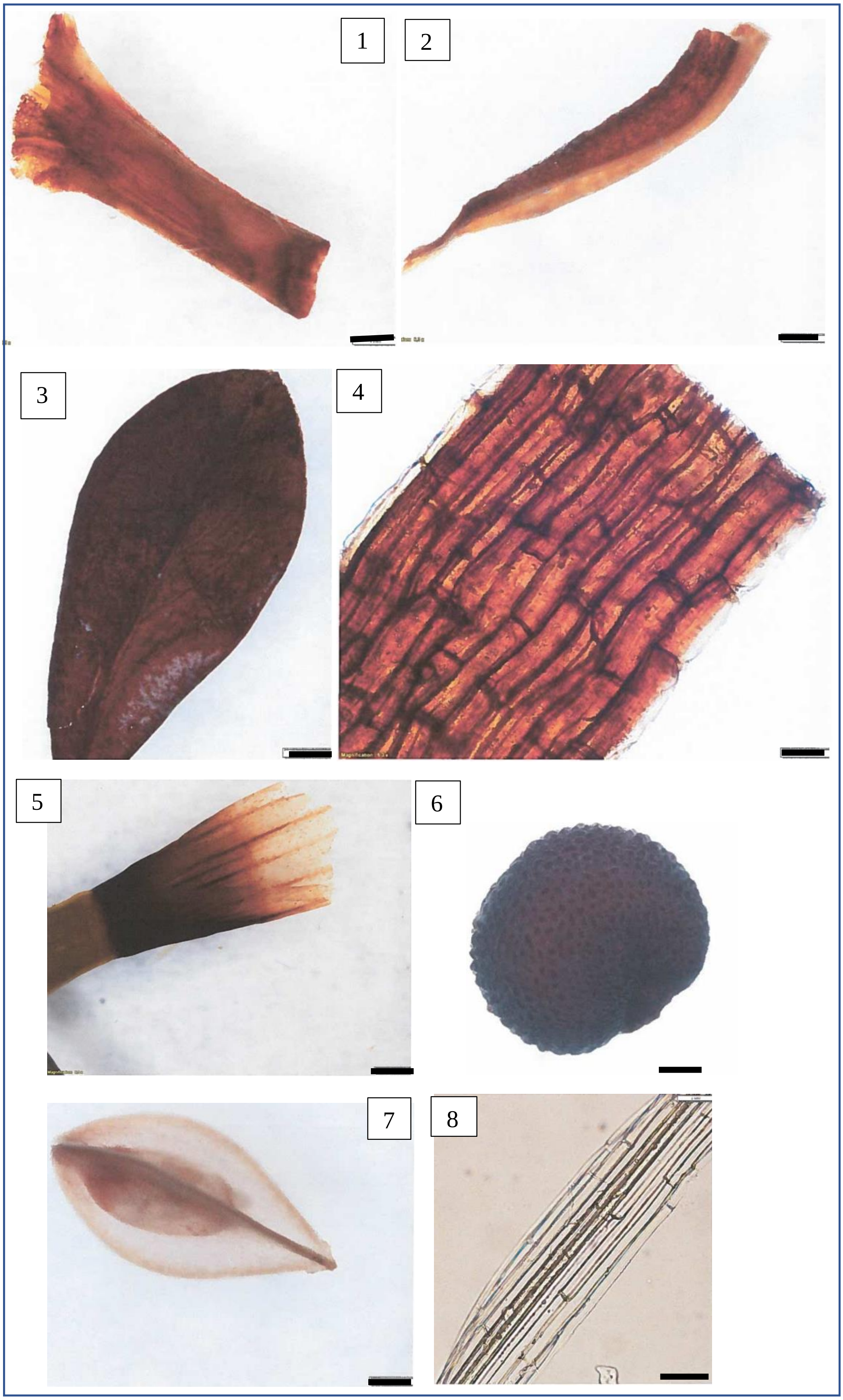
1
2
3
4
5
6
7
8

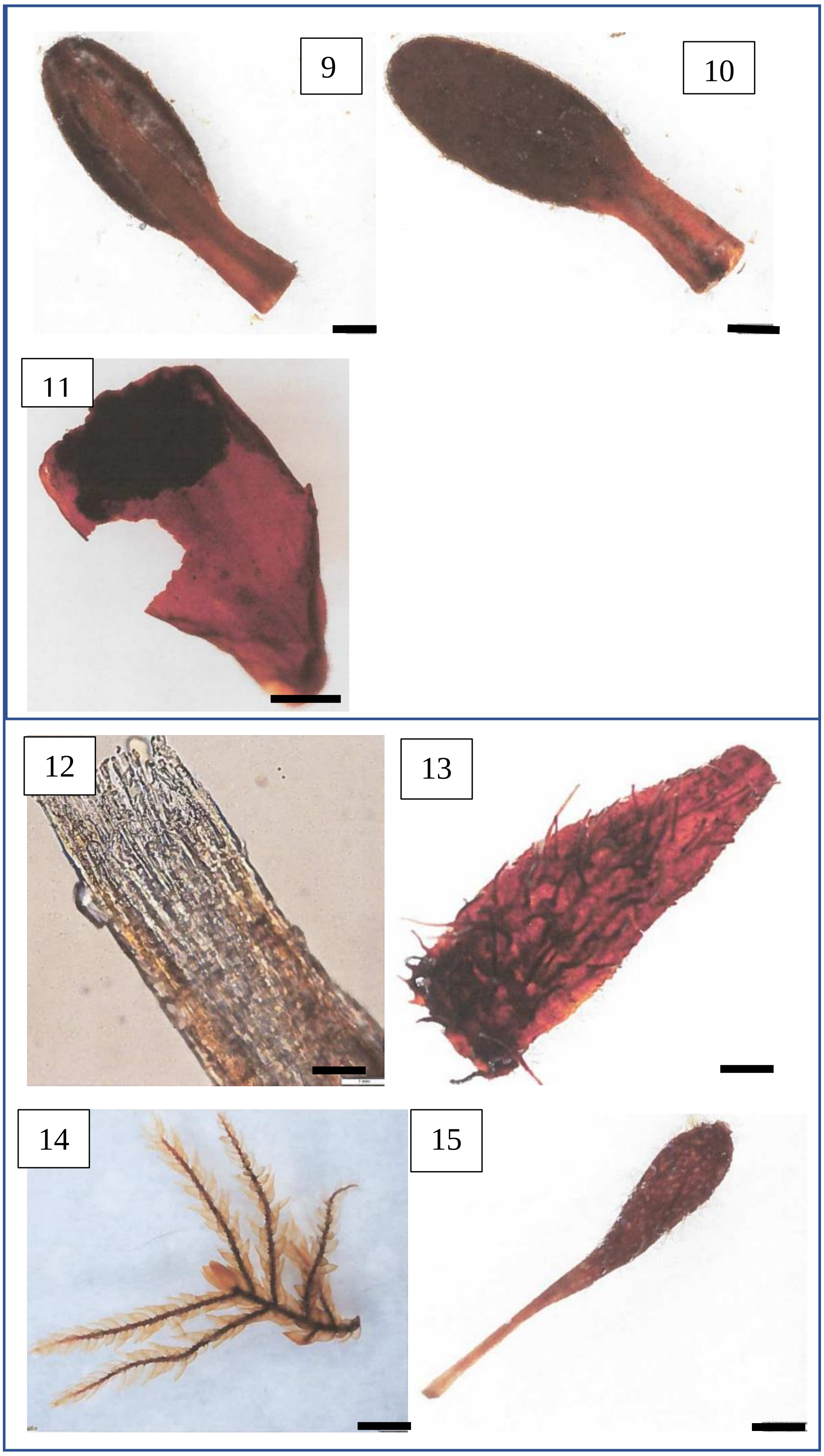

Figure 29. Plant remains from sample no. 3-19, Masi (pictures 1 – 11) and no. 3-18., Masi (pictures 12 – 15). Black rod for scale is 1 mm long. Picture 1 – Salix, 2 – Salix herbacea, 3 – Vaccinium uva-ursi, 4 – Equisetum, 5 – Carex spp, 6 – Siline acaulis cf, 7 – Rumex alpestris, 8 – Eriophorum, 9 – Ericaceae indet, 10 – Ericaceae indet, 11 – Cassiope tetragona. Picture 12 – Carex spp, 13 – Dryas octopetala, 14 – cf Pleurozium spp, 15 – Circea alpina.

GEOLOGICAL SURVEY OF NORWAY
- NGU -

Geological Survey of Norway
PO Box 6315, Sluppen
N-7491 Trondheim, Norway

Visitor address
Leiv Eirikssons vei 39
7040 Trondheim

Tel (+ 47) 73 90 40 00
E-mail ngu@ngu.no
Web www.ngu.no/en-gb/